

SIMULTANEOUS MULTICHANNEL PHOTOMETRY WITH BUSCA

Dissertation

zur
Erlangung des Doktorgrades (Dr. rer. nat.)
der
Mathematisch-Naturwissenschaftlichen Fakultät
der
Rheinischen Friedrich-Wilhelms-Universität Bonn

vorgelegt von
OLIVER-MARK CORDES
aus
Wilhelmshaven

Bonn, 13. September 2004

Angefertigt mit Genehmigung
der Mathematisch-Naturwissenschaftlichen Fakultät
der Rheinischen Friedrich-Wilhelms-Universität Bonn

1. Referent: Prof. Dr. K. S. de Boer
2. Referent: Prof. Dr. W. Seggewiß

Tag der Promotion: 13. September 2004

Diese Dissertation ist auf dem Hochschulschriftenserver der ULB Bonn
http://hss.ulb.uni-bonn.de/diss_online elektronisch publiziert.

“Perhaps when a man has special knowledge and special powers like my own, it rather encourages him to seek a complex explanation when a simpler one is at hand.” - Sherlock Holmes

Contents

1	Introduction	1
1.1	The multicolour simultaneous camera: BUSCA	1
1.2	The first science applications with BUSCA	1
2	Introduction to BUSCA	5
2.1	The BUSCA cube	5
2.2	The BUSCA electronics	7
2.3	The Bonn Shutter	8
2.4	4k×4k CCDs	9
3	BUSCA control software	13
3.1	The main program (MP)	13
3.2	The graphical user interface (GUI)	15
3.3	Remote control	16
3.4	Special exposure types	17
3.4.1	Focus exposures	17
3.4.2	Sequence exposures	18
4	Data and data reduction	21
4.1	Basic data reduction	21
4.1.1	Bias correction	21
4.1.2	Flat-field correction	23
4.1.3	Bad pixel correction	24
4.2	Globular cluster photometry	26
4.2.1	PSF photometry	26
4.2.2	Star pairing	26
4.2.3	Photometric calibration	27
5	BUSCA performance verification	29
5.1	Introduction	29
5.2	Exposure uniformity	29
5.3	Optical quality	29
5.3.1	The PSF	30
5.3.2	Reflections from bright stars	30
5.3.3	Star ghosts	31
5.4	CCD characteristics	31
5.4.1	Noise, fullwell and conversion factor of the CCDs	31
5.4.2	CTE effects	34
5.5	Colour stability	35
5.6	Summary and conclusions	37

6	Are clouds really grey? – Thick clouds observed with BUSCA	39
6.1	Data analysis	40
6.2	Summary and conclusions	41
7	BUSCA Application I: The rapid variable sdB star PG1605+072	43
7.1	sdB stars	43
7.2	The V361 Hya class of stars	43
7.3	PG1605+072	44
7.4	Data and data analysis	45
7.5	Summary and conclusions	47
8	BUSCA Application II: Strömgren photometry of Globular Clusters	51
8.1	Introduction	51
8.2	CN variations in Galactic globular clusters	52
8.3	Results for the individual clusters	54
8.3.1	M12 (NGC 6218)	54
8.3.1.1	Photometry	54
8.3.1.2	Metallicity	56
8.3.1.3	Summary for M 12	56
8.3.2	M71 (NGC 6838)	58
8.3.2.1	Photometry	58
8.3.2.2	Membership analysis	59
8.3.2.3	CN variations	60
8.3.2.4	Summary for M 71	63
9	Further scientific applications and the future of BUSCA	67
9.1	Photometric redshift determination of galaxy clusters	67
9.2	RR-Lyr stars	69
10	Summary and outlook	71
11	Zusammenfassung und Ausblick (Summary in German)	73
A	BUSCA software	77
A.1	Commands from the MP	77
A.1.1	Common commands	77
A.1.2	Filter commands	78
A.1.3	Status commands	79
A.2	Commands from the GUI	79
A.2.1	Common commands	79
A.2.2	Exposure commands	80
A.2.3	Filter commands	81
A.2.4	Shutter and temperature commands	81
A.2.5	Requests	81
B	Artificial Bias	83
C	First order linear transformation	85

Bibliography

87

List of Figures

1.1	<i>The Dumbbell Nebular M27</i> ; first light image of BUSCA in Sep. 1998 (K.Bagschik, O.Cordes)	2
2.1	BUSCA mounted at the 2.2 m telescope at the Calar Alto Observatory	5
2.2	The way of the light beam coming from the telescope through the BUSCA beamsplitter	6
2.3	The transmission characteristics of the BUSCA channels and the position of the Ström-gren and Johnson-Cousins filters are shown. It is obvious that overlapping filter systems (such as the Johnson-Cousin system) cannot be used with BUSCA.	7
2.4	View of the Bonn Shutter before installing into BUSCA. The two black carbon blades are moved into the open state for testing.	8
2.5	The left image shows a correction image for a science image made with an iris type shutter. The exposure time is 0.5 s. The right diagram shows the radial intensity distribution from the centre of the iris to one corner of this correction image. The flux loss of 10% corresponds to the opening and closing time of 20-30 ms of this type of shutters. (Data taken from the ESO public archive.)	9
2.6	This figure shows one of the 3 “thick” CCDs in comparison to a one dollar bill just before mounting the device into one of the dewars.	10
2.7	Quantum efficiency of the thick (solid line) and thinned CCDs (dashed line) used in BUSCA taken from the manufacturers CCD manual.	11
2.8	The temperature of the liquid nitrogen (LN ₂) cooled CCD (bottom panel) and the measured temperature difference (see text) which is correlated to the evaporation rate (top panel, virtual units) are plotted against the time. One can clearly see the 22 minutes time difference between the decrease of the evaporation rate and increase of the CCD temperature.	11
3.1	Data flow diagram of the BUSCA control software. The arrows labelled with DATA show the data flow from the controller to the hard disk. Commands (CMD) to the controller and to the telescope can be sent from the main program (MP) and it receives information (INFO) from these devices. The MP can be controlled by the graphical user interface (GUI) or via a remote TCP/IP network connection. Status information from the MP is displayed in the GUI or sent to the user over TCP/IP.	14
3.2	Screenshot of the BUSCA GUI with the five main panels: the exposure parameter panel, the realtime display panel, the filter control, the exposure status, and the BUSCA status panel.	15
3.3	This dialog shows all temperatures, heating powers and evaporation rates (in arbitrary units). The observer can change the operating temperature of the CCDs individually. Green values signifying the OK status. If a colour turns yellow or red this informs the observer that there is a problem with one of the dewars.	16

3.4	Screenshot of a terminal window which is connected to the BUSCA main program. The output of the “status” command which displays all important status values, e.g. CCD status, temperatures, can be seen as well as the logging output of the background temperature update which indicates a stable evaporation rate of the dewars.	17
3.5	Dialogbox for the parameters for a focus exposure.	18
3.6	A sample image of a focus exposure. Each vertical line of objects is an image of a single star with different telescope focus positions. The steps in intensity at the top of the image signify the brightness steps and the movement of the image between each single exposures.	18
3.7	Dialog to enter the parameters for the sequence mode. The user can select the number of different exposure configurations and the global exposure time (top). Filters and individual exposure times filter can be defined for each exposure configuration.	19
4.1	The line bias structure in x-direction with an amplitude of nearly 10 counts found in the masterbias of channel b. The scatter of ~ 1 count in the profile is due to the readout noise in the image.	22
4.2	Example artificial bias frame for the BUSCA yellow-red channel. The wave like pattern in x-direction with an amplitude of 3 counts is clearly visible in the middle of the image.	23
4.3	This picture shows the flat image taken in the UV channel with the UV_B filter. The brighter areas indicate CCD parts which are more sensitive than the darker areas. Many doughnut rings are visible indicating a lot of dust particles on the filter and on the CCD window. Note that the brightness levels presented lie between 18000 and 22000 counts while a CCD can reach a maximum of 65000 counts.	24
4.4	An example of a bad pixel image of the early $2k \times 2k$ CCD in the BUSCA UV channel. This CCD has a large number of bad pixels and columns in particular in the centre of the CCD which makes the central region unusable. The circle marks one small area which contains a few bad pixels.	25
4.5	Curve of growth of the brightness aperture of a sample star in the M71 field. The enlargement of the aperture radius leads to smaller magnitudes until the optimal radius of ~ 10 pixel is reached. From this point on the star is completely encircled by the aperture.	28
5.1	The relative intensity ΔI plotted versus the row number (parallel to the moving direction of the two shutter blades) for different exposure times of 100 ms (top) down to 1 ms (bottom). The exposure inhomogeneity is at 1 ms about 10% and at 10 ms $< 1\%$. Smaller variations in the bottom diagram are due to noise at 1 ms as well as bad pixels which cannot be reduced completely.	30
5.2	Sample PSF in the near-infrared channel of BUSCA. The contour plot indicates an elongation ($\epsilon=0.058$) due to small telescope movements in east-west direction. The dashed cross signifies the north-west orientation of the image. In general, the dewars are not perfectly aligned with RA & DEC. In this case there is an angular offset of $\sim 7^\circ$	31
5.3	Image of the globular cluster NGC 6366 in the yellow-green channel. The streaks at the lower left are reflections inside BUSCA coming from bright stars outside the CCD field.	32

5.4	This image shows “ghosts” pictures of the two overexposed bright stars. The “ghosts” are coming from secondary reflections in the beam splitter. The flux ratios of the ghosts to the stars are $\simeq 0.25\%$	32
5.5	The behaviour of the RMS in relation to the intensity in logarithmic scale for the yellow-red BUSCA channel is shown. The intensity drops abruptly at the full well point of 155000 electrons. The dashed line is the fit of the linear slope in logarithmic scale. The determined CF is $2.96736 e^-/ADU$	34
5.6	CTE effect of a standard star in the near-infrared channel of BUSCA. The PSF is somewhat rotated and elongated (as in Fig. 5.2) and then wider to the right caused by the CTE effect in x-direction.	35
5.7	Flux distribution along serial readout direction of a single pixel cosmic event with CTE effect near the right border of the blue channel CCD. The determined CTE value of this cosmic of 0.99996 is compatible to the value of the radioactive Fe^{57} source.	35
5.8	The lightcurve of a non variable star during a 70 min cloud passage over the telescope. In the lower left panel two Strömrgren colour indices are plotted which show no significant variability. The right panel indicates the advantage of the simultaneous colour determination against the “classical” sequential method which shows a large deviation.	37
5.9	The upper part shows the y lightcurve of one of the comparison stars of PG1605+072. The colour index $v - y$ is below ± 0.06 mag while the y -magnitude varies by more than 2 mag.	38
6.1	The summed light curve of the reference stars and the colour index curves $UV_B - B_B$ and $B_B - R_B$. Both curves are scaled with a factor of 5 and show clearly an anti-correlation in the behaviour during higher cloud extinction.	39
6.2	This diagram defines the time periods belonging to the “clouds” A,B and C. The period labelled with “phot.” is used as a reference period and shows no signs of clouds.	40
6.3	This graph shows the deviation of the intensity in the BUSCA bands for the three example clouds A,B,C. The intensities are normalised to the assumed grey colour of each cloud. Higher magnitudes indicate larger extinction.	41
7.1	The field of the target star PG1605+072 is shown, and the two comparison stars “Ref. A” and “Ref. B” used for the relative photometry are indicated.	44
7.2	Light curve of PG1605+072 in the BUSCA band R_B for each night. The zero magnitude refers to the median magnitude of the star. The gaps signify the periods of bad weather in which no data were taken.	45
7.3	Lomb-Scargle periodograms of the light curves of PG1605+072 in the BUSCA bands UV_B , B_B (top), R_B and NIR_B (bottom). The horizontal line in each panel represents the confidence level of 99% (3σ -level).	46
7.4	Semi-amplitudes of four selected pulsation frequencies of PG1605+072 as a function of effective wavelength.	47
7.5	Relative semi-amplitudes of the four selected frequencies from Fig. 7.4 of PG1605+072. These are calculated by $\Delta y = (y - \bar{y}/\bar{y})$. y is the semi amplitude of the wavebands.	48
8.1	The two BUSCA pointings on M12 are shown overlain on a map from the DSS. The smaller inner rectangles indicate the small fields available in the UV channel.	54
8.2	CMD of M 12 of all matched stars having v , b , and y magnitudes. Additionally three isochrones were shown which match the data. The best isochrone fit gives an age of 16 Gyr and a metallicity of $[Fe/H] = 1.59$ dex.	55

8.3	m_1 vs. $b - y$ diagram of the red giant branch stars of M 12. The dashed lines indicate isometallicity lines ranging from -2.0 up to 0.0 dex. The metallicity determined by the calibration of Hilker (2000) is $[\text{Fe}/\text{H}] = -1.58 \pm 0.05$ dex.	56
8.4	The two BUSCA pointings on M71 are shown overlain on a map from the DSS. The smaller inner rectangles indicate the small fields available in the UV channel.	58
8.5	CMD of M 71 of all matched stars having v , b , and y magnitudes. Overlaid are three isochrones, two with an age of 12 Gyr and a metallicity of $[\text{Fe}/\text{H}] = -0.80$ and -0.98 dex which fit well the MS and the TOP region, and an isochrone with a larger age of 14 Gyr.	59
8.6	m_1 vs. $b - y$ diagram of the red giant branch stars of M 71. the dashed lines isometallicity lines ranging from -2.0 up to 0.0 dex. The relatively large scatter in this plot is caused by contaminating field stars, so a metallicity determination is not possible.	60
8.7	CMD of the identified cluster members of M 71 together with an isochrone of 12 Gyr and a metallicity of $[\text{Fe}/\text{H}] = -0.98$ dex from Bergbusch & Vandenberg (1992).	61
8.8	m_1 vs. $b - y$ diagram of the identified cluster members of M 71. The dashed lines indicate isometallicity lines ranging from -2.0 up to 0.0 dex. Using the calibration of Hilker (2000) a metallicity of $[\text{Fe}/\text{H}] = -0.76 \pm 0.06$ dex can be determined.	62
8.9	The normalised spectroscopic CN abundance index $S(3839)$ (left panel) and $S(4142)$ (right panel) vs. the difference of the measured and calculated Strömgen metallicity index Δm_1 for the CN calibration stars. The adopted metallicity of the calculated m_1 index is -0.76 ± 0.06 dex. The error bars represent the intrinsic uncertainty of the derived mean metallicity.	63
8.10	The left and right panels show plots of the photometric $S(3839)$ and $S(4142)$ indices vs. the Strömgen y magnitude. Filled and open circles are used to depict CN-strong and CN-weak stars respectively.	64
8.11	This diagram shows histograms of the CN residual indices $\delta S(3839)$ and $\delta S(4142)$	65
9.1	Galaxy cluster observed with the STIS camera on board the HST. The field size of the STIS camera is $\sim 50'' \times 50''$	68
9.2	The same galaxy cluster field (see Fig. 9.1) observed in all four BUSCA bands UV_B , B_B , R_B and NIR_B . The images are scaled against each other. The galaxies of the cluster are getting fainter from the near-infrared to the ultra-violet band. From a rough investigation the redshift estimate for the cluster is $z \simeq 0.4$	68
9.3	Lightcurve of the RR-Lyr star SS Leo from the Strömgen photometry (left panel) and the corresponding atmospheric parameters Θ and $\log g$, and the radius R (right panel). The bump in y at $\phi = 0.75$ with a related change in $b - y$ and c_1 shows no change in Θ	69
B.1	This diagram shows the bias structure in x-directions in an artificial bias frame (for the yellow-green channel of BUSCA). The electronical artefacts from the controller with a typical amplitude of three counts show two effects, a sinoidal function and an overlaying profile.	83
B.2	This figure shows the construction of an artificial bias frame. In the upper left panel there is a stacked master bias of 56 single bias frame for the yellow-green channel. The upper right panel shows the calculated artificial bias frame and in the lower left frame the “reduced” noise pattern can be seen.	84

List of Tables

4.1	Calibration parameters for the 04./05./06. Sep. 2000 with zero-points z , extinction coefficients k , colour terms c and the PSF-aperture shift.	28
5.1	CCD characteristics of all BUSCA CCD's	33
6.1	Definition of the "cloud" periods A,B, and C as well as the extinctions determined for the BUSCA bands. The "phot." period is used as a reference period without cloud influence. The right column shows the mean extinction of all clouds.	40
7.1	Frequencies and corresponding periods as well as semi-amplitudes derived for PG1605+072 in all BUSCA bands. The errors of the periods and amplitudes are formal fit errors from the sine fit procedure. In comparison to the values derived in Kilkenny et al. (1999) the two with stars marked frequencies cannot be resolved in the BUSCA data.	49
8.1	Coordinates and positional properties of the two globular clusters M 12 and M 71 taken from Harris (1996).	51
8.2	Observational properties of the data set.	52
8.3	Member stars of M71 used for photometric calibration of the CN line indices S(3839) and S(4142). The spectroscopic data were taken from Penny et al. (1992).	61

1 Introduction

This thesis is dealing with the multicolour simultaneous camera BUSCA (**B**onn **U**niversity **S**imultaneous **C**amera), which was built at the Sternwarte of the University of Bonn, is divided into a technical and a scientific part. The technical part of this work includes the Ch. 2-6. In Ch. 7 and 8 the first science projects which were done with BUSCA are presented. The following section gives a brief introduction into both parts. At the end of the thesis two future projects are introduced in Ch. 9. A summary about the results of this work and short outlook is given in Ch. 10.

1.1 The multicolour simultaneous camera: BUSCA

At the beginning of this thesis in Sep. 1998, BUSCA was nearly finished and mounted at the 1m telescope of the Hoher List observatory where it had its first light. Fig. 1.1 shows the first light image of the “Dumbbell Nebular” M 27.

The advantage of this new instrument is the capability of observing simultaneously in four different colour bands ranging from the ultraviolet to the near-infrared. This technique saves on one hand the amount of time needed for a full colour coverage of astronomical objects. In comparison, single filter systems waste all the light except that light passing the band filter. On the other hand, the simultaneous observation in four colours should provide a stability of the colour indices during non-photometric conditions caused by variable extinction, e.g., thin clouds (droplets, ice crystals) or dust. This includes the assumption that thin clouds have a grey colour, which means an equal flux loss in all colour bands. Additionally, a new shutter, the “Bonn Shutter”, was developed. It provides homogeneous illumination over the whole field of view at small exposure times (<0.1 s).

After the first light of BUSCA a new control software was developed and new hardware (most important, the $4k \times 4k$ CCDs) was installed. When the camera was completed several tests to check the overall performance were done. In many observing runs at the Hoher List and Calar Alto observatory BUSCA was amply tested, including the optical performance, the shutter, the CCDs, and the electronical system. Also the predicted colour stability was analysed.

The technical part of the thesis is organised as follows: Ch. 2 gives an overview of BUSCA with a detailed technical description, the control software is presented in Ch. 3, and in Ch. 5 the results of the overall performance tests are shown. Sect. 5.5 deals with the colour stability and is followed by a study about the grey colour of clouds in Ch. 6.

1.2 The first science applications with BUSCA

In Ch. 7 the first simultaneous observations of the rapidly variable sdB star PG1605+072 are presented. sdB (sub-luminous B) stars dominate the population of faint blue stars of our Galaxy and are found in the disk (field sdBs), in globular clusters and in the halo of our Galaxy. Belonging to the extended Horizontal Branch (EHB), sdB stars burn He in their cores of about half a solar mass and have a thin hydrogen envelope surrounding the core. Some of these sdB stars were recently found to exhibit

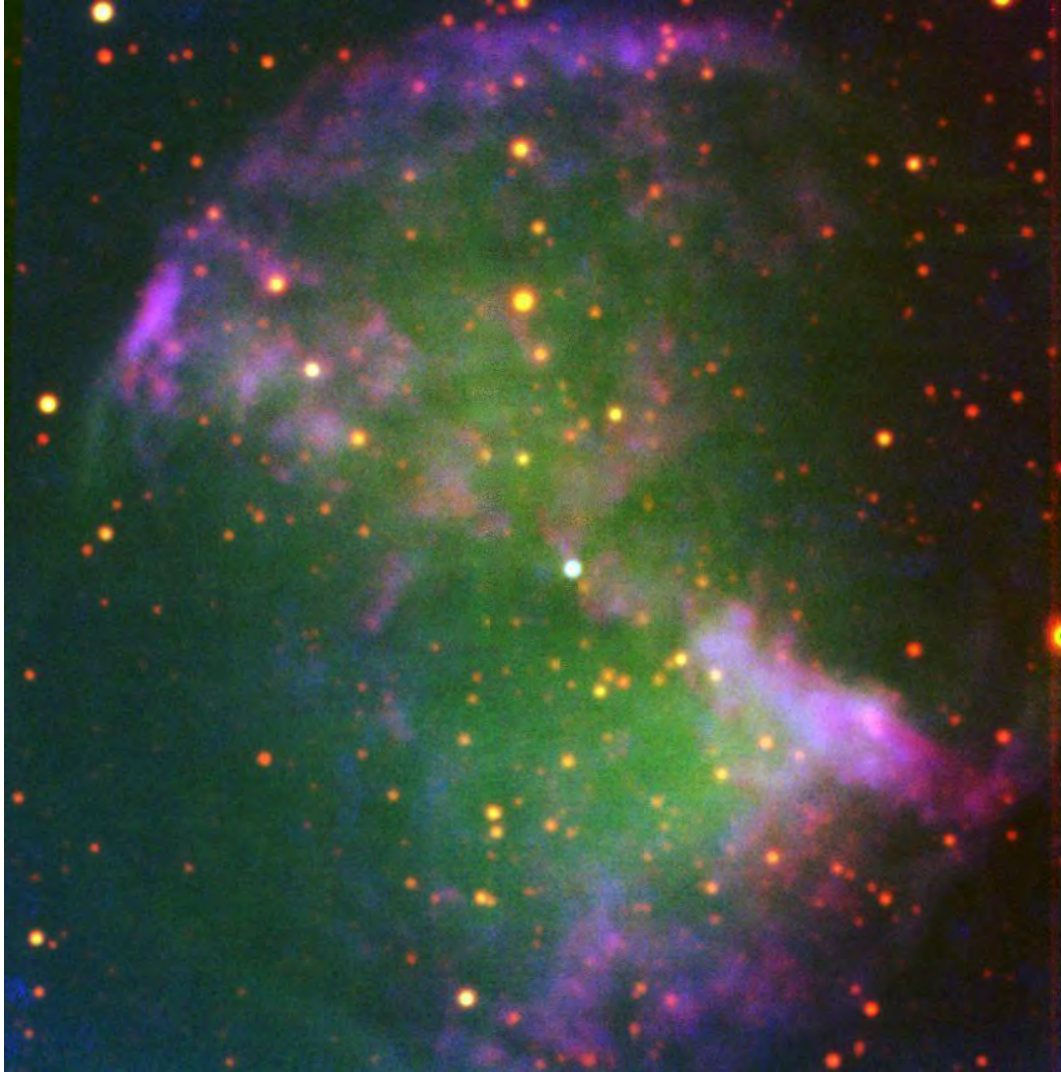


Figure 1.1: *The Dumbbell Nebular M27*; first light image of BUSCA in Sep. 1998 (K.Bagschik, O.Cordes)

rapid multi-periodic light variations ($P \approx 80 - 600$ s) of low amplitudes (a few mmag). They form a new class of pulsating stars named V361 Hya stars for which more than 30 sdB pulsators are known. The stellar pulsations allow insight into the structure of the stellar atmosphere and therefore indirectly into the evolutionary history of the sdB stars. With this asteroseismological analysis tool it is then possible to determine the stellar mass as well as the envelope mass. PG1605+072 is an ideal target for a photometric and spectroscopic analysis, because it has the longest pulsation periods (≈ 500 s) known for this class of variable stars, and with 50 known pulsation frequencies it possesses by far the richest frequency spectrum.

Observations with BUSCA exploit the possibility to obtain colour information during each single measurement. The simultaneously observed data avoid the problem of deriving colour indices through interpolation in data obtained during variable photometric conditions.

The second science project deals with the Strömgren photometry of Galactic globular clusters. One

advantage of the Strömgren photometry is that it can be used as a reliable metallicity indicator. The Strömgren v filter includes several iron absorption lines and is as well as the $m_1 = (v - b) - (b - y)$ index sensitive to the iron abundance. Giant and supergiant stars with a constant iron abundance in the colour range of $0.5 < (b - y) < 1.1$ mag form an approximately straight line in a $(b - y), m_1$ diagram. This behaviour is used in this work to determine the iron metallicity of two Galactic globular clusters, M 12 and M 71, observed with BUSCA. Both clusters are well studied, but up to now no Strömgren metallicity studies were available. Moreover, M 71 shows additional CN variations among the red giant branch (RGB) and main sequence (MS) stars. The origin of these CN variation is not yet understood. One possible explanation is an evolutionary scenario in which the CN abundance at the star surface is enriched with processed material (out of the CNO-cycle) from inside the star. The next explanation is based on a self-pollution scenario in which stars in the globular cluster (e.g., AGB stars and novae) eject stellar winds. These winds can contain CNO enriched material which can be accreted by other stars. The last discussed scenario deals with primordial variation of CN in the molecular cloud in which the globular cluster was born. Also a merging of two primordial clouds with different chemical composition is a possible scenario.

In the past the CN variations were detected spectroscopically for only a few RGB and MS stars. With this photometric approach with BUSCA more RGB stars were investigated. The results of these globular cluster studies are given in Chap. 8.

2 Introduction to BUSCA

The Bonn University Simultaneous Camera (BUSCA) was nearly finished when in 1998 this thesis research started. The basic BUSCA characteristics were described in the theses by Schmoll (1997) and Bagschik (2001), giving details about the optics, and by Kohley (1998) and Harbeck (2000) describing the CCDs. The essentials have been given by Reif et al. (1999).

This chapter gives a compact overview of BUSCA and describes those technical details, which are of relevance for this thesis.

2.1 The BUSCA cube

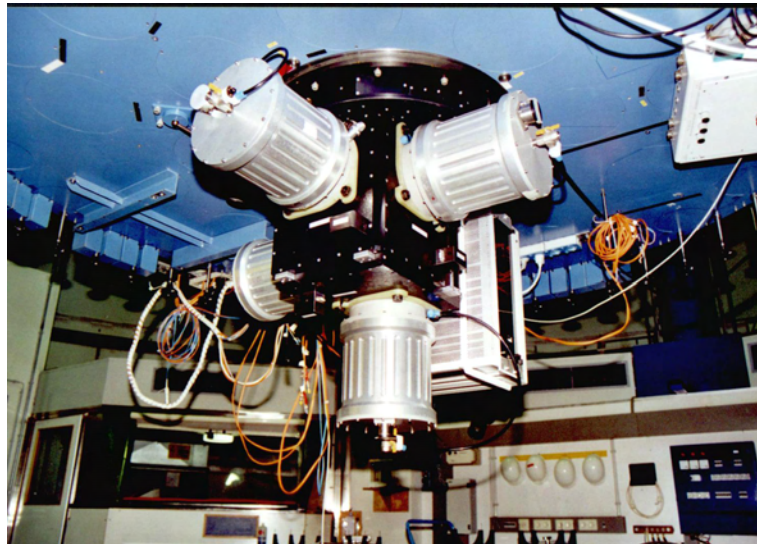


Figure 2.1: BUSCA mounted at the 2.2 m telescope at the Calar Alto Observatory

The BUSCA cube (see Fig. 2.1), the black box in the centre of the image to which the 4 dewars and the electronic boxes are mounted, contains the BUSCA optics. The main part of this optical system is the beam splitter which divides the incoming light beam in four separate colours, ultraviolet, blue-green, yellow-red and visual infrared. For this purpose three dichroic plates are installed. In all dichroic plates the incoming light is split into a blue totally reflected and a red transmitted beam. In Fig. 2.2 the schematic view of the light path in BUSCA is shown. The first dichroic plate tilted by 45° splits the incoming light into a red and blue beam. Then both beams are being splitted again into the final BUSCA bands.

The disadvantage of the dichroic plates is the astigmatism of each transmitted converging beam due to refraction inside the plate tilted against the optical axis. However, this effect can be corrected by a second plate of the same type which is also tilted by 45° and rotated by 90° around the optical axis

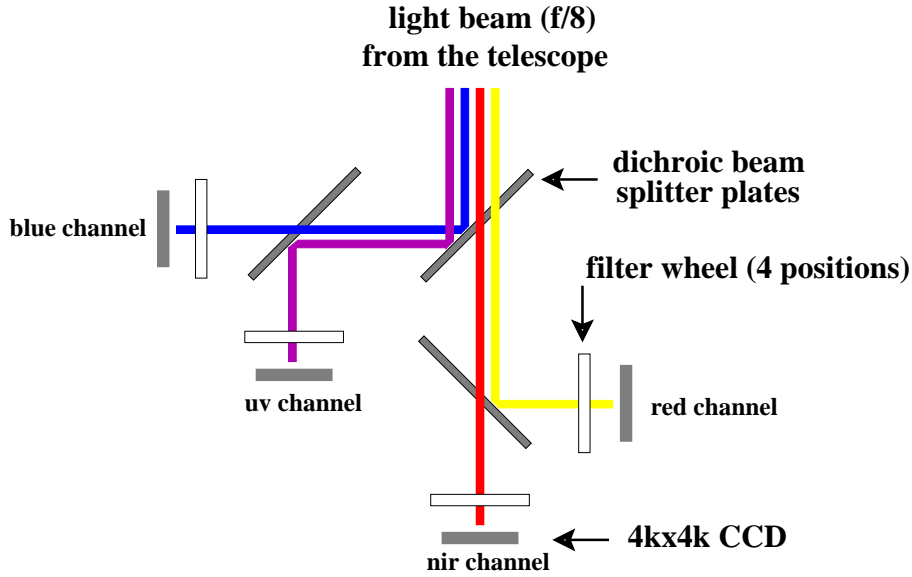


Figure 2.2: The way of the light beam coming from the telescope through the BUSCA beamsplitter

against the first plate (see Bagschik 2001). All dichroic plates in BUSCA are positioned such that the light in the ultraviolet channel (a twice reflected beam) and in the visual infrared channel (transmitted two times) needs no correction. Only the blue-green and yellow-red light beam are affected by the astigmatism effect because these are once transmitted and once reflected. For correction extra glass plates are installed behind the last dichroic plates. These glass plates have the same optical behaviour as the dichroic plates (except the reflection properties) for the transmission light beam. After the additional transmission these beams are now also astigmatism corrected.

For special colour selection a filter wheel with four positions for each BUSCA band is installed. The primary filter set is the complete Strömrgren filter system u , v , b , y , $H\beta_{\text{small}}$ and $H\beta_{\text{wide}}$. Due to the fact that no Strömrgren filter is defined which fits in the near-infrared channel a Cousins- I filter is installed. In comparison to the small band Strömrgren filters the Cousins- I is a broad band filter. This affects the exposure time which has to be chosen for all channels. The infrared image with this filter combination tends to be overexposed much faster than in the other channels.

The installation of a second filter set, the Thuan-Gunn set (u , v , g , and r) is possible but not yet realised. Similar to the Strömrgren filter set the Thuan-Gunn u and v filter fit into the ultraviolet, the g filter into the blue-green, and the r filter into the yellow-red channel. Data taken with a BUSCA Thuan-Gunn set can then be used in combination with data from, e.g., the Sloan Digital Sky Survey (SDSS) which uses a modified Thuan-Gunn set (u' , v' , g' , and r'). The SDSS set was also extended into the infrared with the z' filter, which would fit into the BUSCA visual infrared channel, to cover the wavelength range from the ultraviolet to the visual infrared.

Filter sets consisting of overlapping filters, e.g., the Johnson-Cousins system U , B , V , and R cannot be used with BUSCA. To provide a possibility for broadband photometry white glass filters in combination with the beamsplitter itself define the intrinsic BUSCA filter system UV_B , B_B , R_B , and NIR_B . The thickness of the white glass filters is the same as for the Strömrgren filters and provides the same focal plane. Thus the use of white glass filters in combination with the Strömrgren filters without changing the telescope focus is possible. The white glass filters, while cheaper than interference filters, are also used for protecting the beamsplitter against dust and mechanical impacts during

dewar mounting and demounting.

In Tab. 2.1 the filter sets which are currently installed in BUSCA are listed giving centre wavelength and FWHM. The two not installed Thuan-Gunn and Johnson-Cousin filter systems are additionally mentioned. Fig. 2.3 shows the transmission curve of each BUSCA channel and the position of the Strömrgren filter set in comparison to the Johnson-Cousins filter set.

Table 2.1: Comparison of the different filter sets in BUSCA with the not installed Thuan-Gunn and Johnson-Cousin set. All filters are given with their specified centre wavelength and FWHM.

BUSCA Channel	λ [nm]	intrinsic filter	Strömrgren		Thuan-Gunn		Johnson-Cousin ¹				
			λ [nm]	FWHM [nm]	λ [nm]	FWHM [nm]	λ [nm]	FWHM [nm]			
ultraviolet	< 430	UV_B	u	350	38	u	353	40	U	365	54.2
blue-green	430 – 540	B_B	v	410	20	v	398	40	B	440	93.5
			b	470	20	g	500	70			
			$H\beta_n^2$	486.1	3						
			$H\beta_w$	486.1	15						
yellow-red	540 – 730	R_B	y	550	20	r	655	90	V	550	103.5
vis. infrared	> 730	NIR_B				z'^3	913	95	R	597.5	149.8
								I	795.6	122.2	

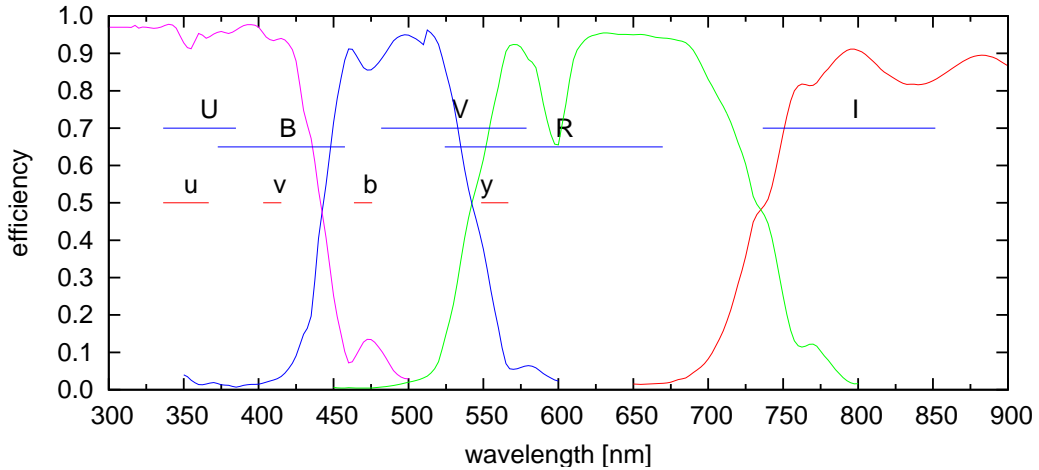


Figure 2.3: The transmission characteristics of the BUSCA channels and the position of the Strömrgren and Johnson-Cousins filters are shown. It is obvious that overlapping filter systems (such as the Johnson-Cousin system) cannot be used with BUSCA.

2.2 The BUSCA electronics

For controlling BUSCA, two control units the “Universal Control” (UC) and “CCD control unit” (CCU) were developed.

¹The Johnson-Cousin filter system does not fit into the BUSCA system and is only shown for comparison.

²There exists two $H\beta$ filters: $H\beta_n = H\beta(\text{narrow})$ and $H\beta_w = H\beta(\text{wide})$

³SDSS extension of the Thuan-Gunn filter definition

The UC is a micro-controller based system which controls the shutter, the temperature of the CCD chips, and the filter wheels. Also the evaporation of liquid nitrogen of the BUSCA dewars is monitored (see Sect. 2.4). All micro-controllers modules are connected by means of the CAN-bus. One of them, the interface module, has a serial line connection to the observers workstation.

The CCU used for BUSCA is a modified “Heidelberg-Controller” with four individual CCD channels. This controller type was developed at the MPIA in Heidelberg and is used with several standard instruments at the Calar Alto Observatory, e.g., CAFOS or MOSCA. Thus far it has only been used with one CCD channel. All the CCD data can in principle be read out parallel saving time in comparison to a sequential mode in which one CCD is read out after the other. The CCD data stream from the CCU to the computer is transferred serialised through a high speed fibre cable. It is then converted into a 16-bit parallel stream by a Sun/TAXI interface designed also at the MPIA in Heidelberg and read from a parallel S16d interface⁴ built in the SUN observing workstation. The CCU architecture also includes the possibility to define a sub frame out of the complete CCD frame. This reduces, in some cases, the amount of data and time and is very useful for single star photometry, e.g., standard star observation or for variable star photometry.

2.3 The Bonn Shutter



Figure 2.4: View of the Bonn Shutter before installing into BUSCA. The two black carbon blades are moved into the open state for testing.

One typical problem or limitation during an observing run is the minimum allowed exposure time. With the continuous increase in diameter of telescope mirrors the exposure time for e.g. bright stars drops rapidly. One example: the Strömgren standard stars (Perry et al. 1987) we used for calibration are in the range of 4-6 mag in y . The typical exposure time with good seeing conditions are below 1 s for these stars. As a consequence, BUSCA needed a shutter which guarantees a homogeneous illumination of the CCD at exposure times significantly below 1 s. The shutters which are commonly used in many astronomical instruments are iris type shutters. These are usually build for small $2k \times 2k$ CCDs. Iris type shutter have problems with short exposure times, since the opening resp. closing time of the iris in comparison to what BUSCA needs is too long. In the case of small exposure times the CCD would not be illuminated homogeneously and shutter correction images are needed for each

⁴Developed by Engineering Design Team, Inc.

exposure time. Fig. 2.5 shows such a correction image taken from the ESO public archive. This image was created for an exposure time of 0.5 s and a picture of the iris structure is clearly visible. On the right diagram the radial intensity distribution of this correction image which represents the flux loss is shown. The variation of 10 percent from the centre to the edges is caused by the opening and closing time of iris type shutters which are typically 20-30 ms.

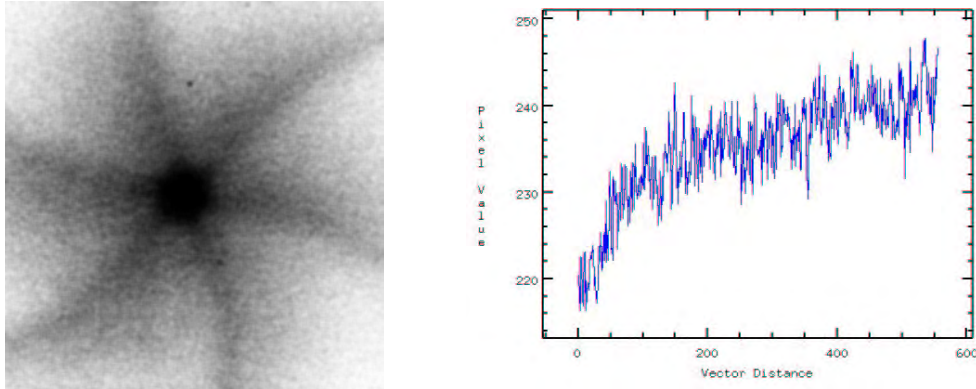


Figure 2.5: The left image shows a correction image for a science image made with an iris type shutter. The exposure time is 0.5 s. The right diagram shows the radial intensity distribution from the centre of the iris to one corner of this correction image. The flux loss of 10% corresponds to the opening and closing time of 20-30 ms of this type of shutters. (Data taken from the ESO public archive.)

To avoid the problem of an inhomogeneous illumination of the CCD it was decided to build a moving slit type shutter. The “Bonn Shutter” (see Fig. 2.4) consists of two carbon blades which move over the shutter aperture. The exposure starts with the motion of the first blade and after a delay, which is defined by the exposure time, the second blade moves with the same trapezoidal velocity profile (acceleration, maximum speed, braking). The moving direction of the blades changes after each exposure, therefore no reset drive between two exposures is needed. For long exposure times the shutter opens completely. On the other hand, for short exposure times the two blades form a small slit which is moving over the CCD. The slit is narrow at the edges (acceleration and slowing down phase) and maximum wide in the middle of the CCD. The different width of the slit is compensated by the speed of the slit to ensure a homogeneous illumination of the CCD. Limitations are due to the stepper motor resolution and the tolerances of the mechanics. The effect becomes more and more important for very short exposure times in the range of a few milliseconds. The performance of the Bonn Shutter is described in Sect. 5.2.

2.4 4k×4k CCDs

The most important part besides the optics are the CCDs (Charge Coupled Devices). For BUSCA four Loral CCD485⁵ 4k×4k CCDs with 15×15 μm pixels were bought. This type of CCD with the format of 6 cm×6 cm, the same format as an old negative film, was developed for digital home cameras in the first place. They provide an astronomical field of view of nearly 12′ × 12′ at the 2.2m telescope at Calar Alto. CCDs operating at room temperature produce a large dark current during long exposure

⁵From Lockheed Martin Fairchild Systems (formerly Loral)

times which is not preferable for astronomical observations. Therefore all CCDs used in astronomy are mounted into evacuated liquid nitrogen dewars with a window on top (sometimes lenses are used instead). The operating temperatures of the BUSCA CCDs are between -90° and -130° . This is done by an active temperature controlling provided by the UC (see Sect. 2.2). Figure 2.6 shows one of the CCDs before it was installed in one of the BUSCA dewars.



Figure 2.6: This figure shows one of the 3 “thick” CCDs in comparison to a one dollar bill just before mounting the device into one of the dewars.

Usually CCDs are “thick” which means that they are less sensitive in the ultraviolet part of the optical spectrum; the quantum efficiency goes steeply down towards the blue. Taking this into account, the CCD for the ultraviolet channel is specially thinned and coated which makes it much more sensitive in the blue. For comparison the quantum efficiency of both CCD types used in BUSCA are shown in Fig. 2.7.

Testing the CCD system one disadvantage of the three thick CCDs used in BUSCA was discovered. They all have a relatively poor “charge transfer efficiency” (CTE) which affects the data reduction (see Sect. 5.4.2). However, the thinned CCD does not show any CTE problems. In the future some of these “bad” CCDs should be replaced with CCDs with a better CTE.

Additionally to the temperature controlling the UC monitors the evaporation rate of the liquid nitrogen. Therefore the temperature of the evaporating gas is measured relatively to the temperature outside the dewar. This temperature difference is correlated to the evaporation rate. If the nitrogen approaches exhaustion this temperature difference starts to decrease after a few minutes. The temperature of the CCD, however, stays constant for at least 22 minutes before it increases as well, unless the dewar is refilled. The observer is also warned by the control software. The temperatures of the CCD and the amount of evaporating liquid nitrogen as a function of time are shown in Fig. 2.8. The point of warning can be easily determined while watching the slope of the evaporation function. The evaporation rate decreases rapidly after exhaustion while the CCD temperature stays constant for another 22 minutes.

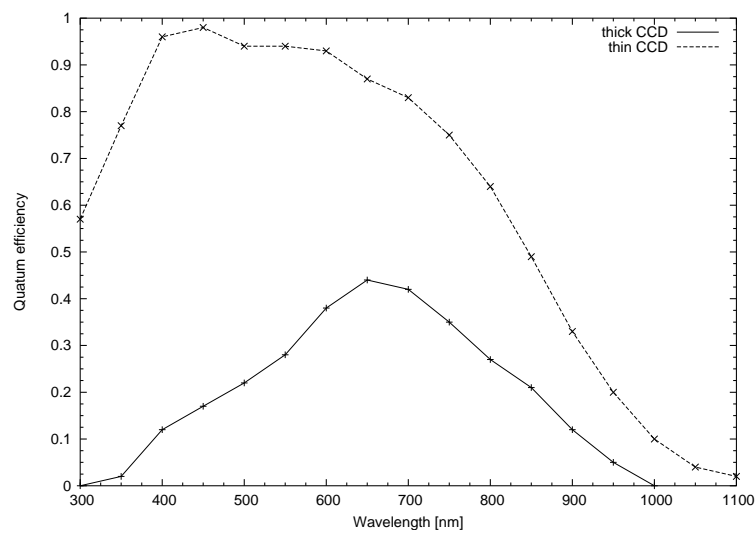


Figure 2.7: Quantum efficiency of the thick (solid line) and thinned CCDs (dashed line) used in BUSCA taken from the manufacturers CCD manual.

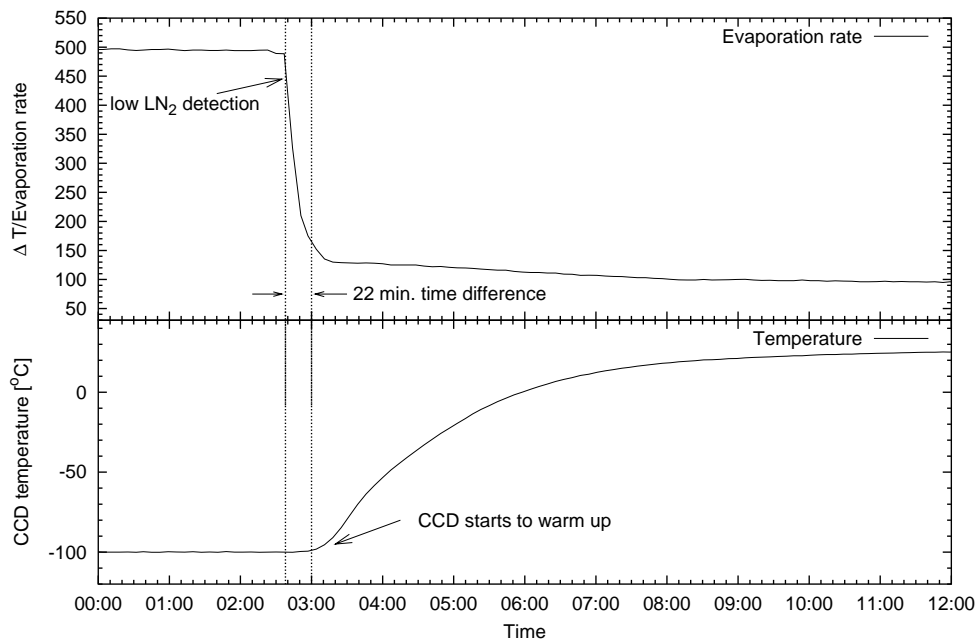


Figure 2.8: The temperature of the liquid nitrogen (LN₂) cooled CCD (bottom panel) and the measured temperature difference (see text) which is correlated to the evaporation rate (top panel, virtual units) are plotted against the time. One can clearly see the 22 minutes time difference between the decrease of the evaporation rate and increase of the CCD temperature.

3 BUSCA control software

During the development and construction phases of the BUSCA electronics the first BUSCA control software was developed by Kohley (1998). The program was running on an Alpha workstation under the IDL programming language. A driver written in C controlling the hardware parallel interface was used for the data acquisition. This software contained also several analysis tools for CCD frames which was useful to tune and optimise the CCD system of BUSCA. For then integration of the BUSCA system into the Calar Alto soft- and hardware environment (mostly SUN workstations) and because of speed and memory limits the IDL software package was no longer tenable. The software was completely rewritten now using a main program (MP) written in C and a graphical user interface (GUI) implemented in Tcl/Tk. The software provides an easy to use interface to control all important functions of BUSCA.

In this chapter the software developed as part of this reconstruction is described. Figure 3.1 shows the data flow diagram of the current BUSCA control software. The MP communicates via serial devices with the CCD controller (CCU) and the BUSCA device controller (UC). All CCD data are transferred over a parallel interface from the CCU to the workstation and are stored in FITS format on the hard disk. For interaction with the observer the MP receives commands from the GUI or via a TCP/IP interface. Thus all information is sent to the GUI or over the TCP/IP connection.

The following sections describe the MP, the GUI and the remote controlling via TCP/IP in detail. The last part of this chapter deals with some special exposure types which are helpful for observing with BUSCA.

3.1 The main program (MP)

The MP, the heart of the BUSCA control software, is invoked by the GUI during the start of the software and is connected to the GUI by a command pipe. This allows a bidirectional communication between the MP and the GUI. The MP controls the CCU and UC controller and responds to interactions from the GUI or from the remote control via the TCP/IP protocol. Further functions are implemented such as to control the focus of the telescope which is mainly used to obtain focus images (see Sect. 3.4.1) and to get the telescope position to be stored in the information header of each image.

During the program startup three tasks are initiated, the command task, the update task, and the exposure task. All tasks share the same environment (variables and functions) but they are running without direct interactions, except for the exposure task which is triggered by the command task. Messages from the MP, e.g., a new filter position, are sent directly to the GUI through the command pipe. Also, if a task needs interaction from the observer it will start a dialog box which is then displayed by the GUI. Appendix A.1 gives a complete list of all commands which are sent from the MP to the GUI.

The command task

The command task is a simple loop which reads commands from the pipe to the GUI or from the TCP/IP server which was started during startup (see Sect. 3.3). The commands are divided in two

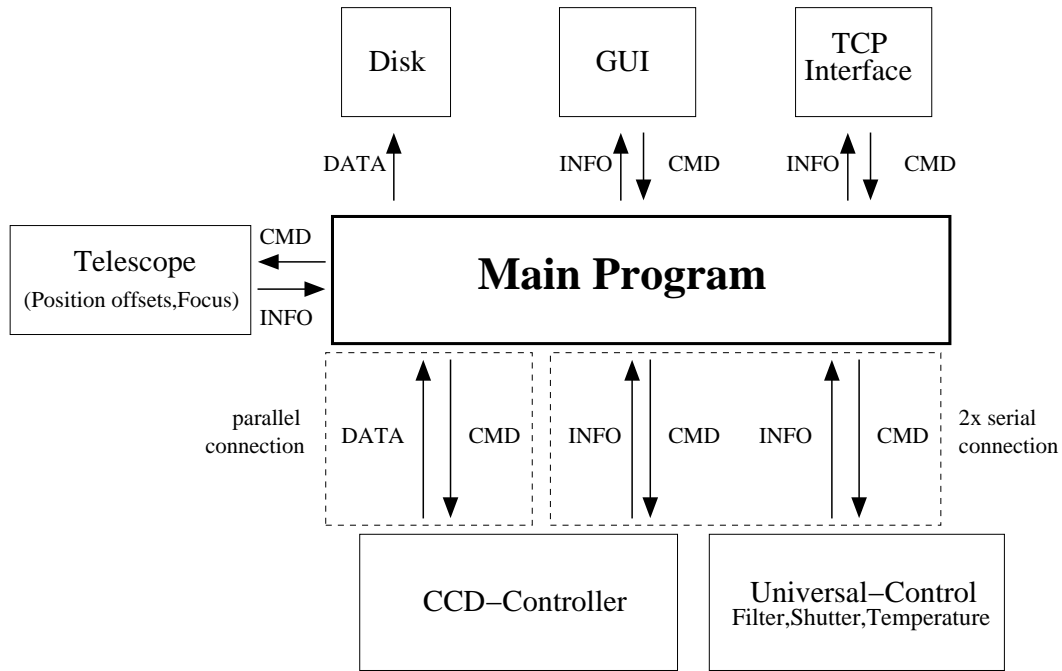


Figure 3.1: Data flow diagram of the BUSCA control software. The arrows labelled with DATA show the data flow from the controller to the hard disk. Commands (CMD) to the controller and to the telescope can be sent from the main program (MP) and it receives information (INFO) from these devices. The MP can be controlled by the graphical user interface (GUI) or via a remote TCP/IP network connection. Status information from the MP is displayed in the GUI or sent to the user over TCP/IP.

types. One type are real commands which start an action, e.g., changing a filter. The second category are request commands from the GUI to get status information. If a command is received and executed the task is not able to respond to other commands during its execution. The only exception is the command to start a new exposure. Therefore the command task only initiates the exposure task. This enables the sending of a break or pause command during an exposure, which has to be handled first of all by the command task.

In Appendix A.2 all commands which are recognised by the MP are listed.

The update task

The update task (a background task) regularly checks temperature and evaporation rates of the CCDs. The observer will be informed in the case the liquid is exhausted (see Sect. 2.4). When a new filter was selected and the filter wheel is moving the task also checks the status and the position of the filter wheel until the new position is reached.

The exposure task

The most complex task is the one for taking exposures. When the observer starts an new exposure the GUI transfers all parameters necessary for an exposure to the MP, e.g., exposure time, CCD parameters, and object name. Then the exposure task is triggered from the command task. Depending on the type of exposure (bias, flat, dark or special exposure (see Sect. 3.4) the exposure task first sends commands to clean the CCDs and then performs the real exposure. After this the CCD frame is read

out. During the real exposure the observer can stop the exposure by pressing the *Break* button on the GUI. It is on the other hand not possible to interrupt the readout process. All other actions, e.g. changing a filter, are blocked during the exposure process.

3.2 The graphical user interface (GUI)

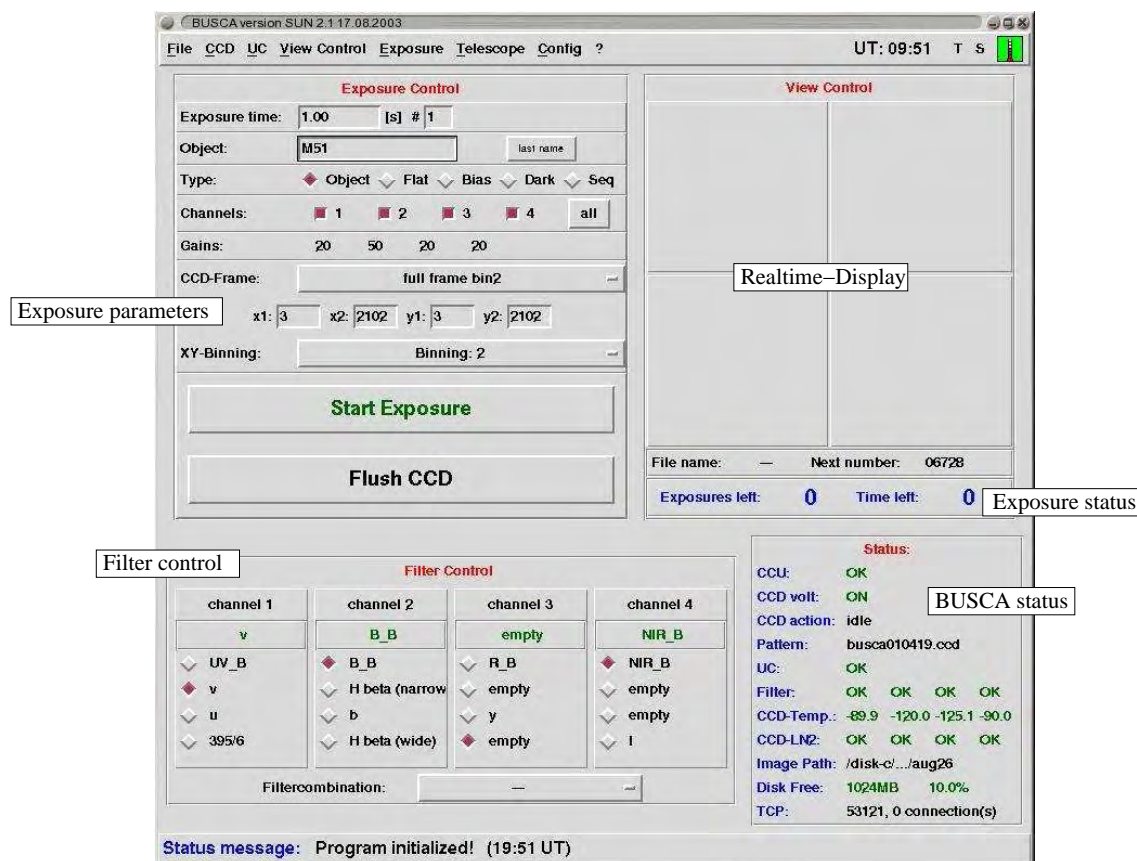


Figure 3.2: Screenshot of the BUSCA GUI with the five main panels: the exposure parameter panel, the realtime display panel, the filter control, the exposure status, and the BUSCA status panel.

The graphical user interface (GUI) is divided in five panels (see Fig. 3.2). The **exposure parameter panel** at the top left of the main window controls all parameters for a simple exposure (see Sect. 3.4 for special exposures). The observer can set the exposure time, the number of exposures, and the exposure type. For each exposure an object name must be given. The button with the label *last name* selects the object name used for the last image.

In the middle of this panel the observer can choose the image frame size and a binning mode for the readout process. The default frame size and binning is the full frame (2048×2048 pixel) with a 2×2 binning. The large button, labelled with *Start Exposure* at the bottom of the panel, starts the exposure. With the other button, *Flush CCD*, the CCDs can be cleaned in the case that the previous image was overexposed. This action performs a single and fast readout process of the CCD without transferring the data and removes all leftover charges from the CCDs. During the exposure the function of these two buttons changes. Pressing the upper button will then stop the exposure until the observer wants

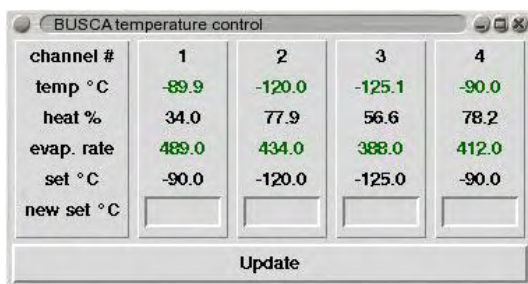
to restart or quit the current exposure. The lower button quits the exposure immediately.

The **exposure status panel** below the realtime display shows the remaining exposure time. In the case of multiple exposures it also displays the number of exposures left.

In the **filter control panel** the observer can change individual filters or select a filter combination, e.g. *vbyI* for a Strömgren set plus the Cousins I filter.

On the top right side of the GUI a **realtime display** is implemented. During the readout process the incoming data is scaled into a 150×150 pixel thumbnail for each channel. The display is arranged such that the thumbnails of the UV and blue channel are placed in the first and the thumbnails of the yellow-green and near-infrared channel in the second row. The user can define a minimum and maximum value in the realtime dialog accessible from the *View control* submenu of the GUI in which the data values are displayed in greyscales. Pixels below the minimum are black and above the maximum value yellow. All values higher than 60000 are displayed in red, because then the image will probably be overexposed.

The status of the BUSCA system is summed up in the **BUSCA status panel**. It gives all important status information about CCDs, temperatures, liquid nitrogen, and filter wheels. For detailed information about the CCDs the user can open a temperature dialog (see Fig. 3.3) with the button *T* from the menu bar. It shows the temperatures, heating powers, and evaporation rates for each dewar. The observer can change the operating temperature of each CCD. For this dialog as well as for the BUSCA status panel green values signify normal operation; yellow or red colours indicate problems.



channel #	1	2	3	4
temp °C	-89.9	-120.0	-125.1	-90.0
heat %	34.0	77.9	56.6	78.2
evap. rate	489.0	434.0	388.0	412.0
set °C	-90.0	-120.0	-125.0	-90.0
new set °C				

Update

Figure 3.3: This dialog shows all temperatures, heating powers and evaporation rates (in arbitrary units). The observer can change the operating temperature of the CCDs individually. Green values signifying the OK status. If a colour turns yellow or red this informs the observer that there is a problem with one of the dewars.

3.3 Remote control

One important aspect of the software development was to create the possibility to have access to the MP via a remote TCP/IP connection. With this network connection the BUSCA team can check all important status information of the BUSCA system in Bonn and can give assistance to the Calar Alto staff in the case of problems with BUSCA. The status includes all information of the “BUSCA status” section of the GUI plus all filter positions. Additionally logging information, which is also saved in a log file, is sent over the remote connection. An open connection can be used to send commands similar to the commands of the GUI to the MP to control BUSCA.

The MP invokes a TCP/IP server during startup which listens on port 53121 for incoming connection requests. If this port is already in use the MP increments the port number by one until it finds a free TCP/IP port.

Figure 3.4 shows an active remote network session to the MP. It shows the current status of the BUSCA system while the last lines give the logging output of the background temperature update. It signifies that the measured evaporation rate is constant over the last measured time period of 5 minutes. This

means that there is enough liquid nitrogen in the dewars.

```

aibn32:/user3/ocordes
Welcome to CBUSCA tcp-port (host 127.0.0.1 port 46004)

CBUSCA V2.0 (C) 1999,2000,2001 by STW University Bonn

IPL 28.10.2003 20:09.39 :: TCP: connection established
IPL 28.10.2003 20:09.39 :: TCP: 1 active connections
cbusca tcp>status

cbusca status:

CCU: (active)
voltages      : on
conscan       : off
exposing      : no
dsp version   :
pattern name  : /disk-a/busca/pattern/busca010419.ccd

UC: (active)
temperatures  : -89.9 -120.0 -125.1 -90.0
temperatures (set): -90.0 -120.0 -125.0 -90.0
heat power [%] : 34.0 77.9 56.6 78.2
LN2 (in)      : 1000.0 945.0 899.0 923.0
LN2 (out)     : 511.0 511.0 511.0 511.0
LN2 (status)  : ok ok ok ok
filter active  : ok ok ok ok
filter status  : ok ok ok ok
filter position : 7200 50 21600 50
filter pos. (enc) : 7200 50 21600 50
filter name    : v B_B empty NIR_B

OBS:
observers name : Alises y Guijarro
save image path : /disk-c/service/masegosa/aug26/
file prefix     : bu
next image number : 06728
disk free      : 1024 MB

cbusca tcp>
IPL 28.10.2003 20:09.53 :: ln2_analysis: dewar 0 ln2 slope 0.000
IPL 28.10.2003 20:09.53 :: ln2_analysis: dewar 1 ln2 slope 0.000
IPL 28.10.2003 20:09.53 :: ln2_analysis: dewar 2 ln2 slope 0.000
IPL 28.10.2003 20:09.53 :: ln2_analysis: dewar 3 ln2 slope 0.000
cbusca tcp> quit

aibn32 20:09:58 ~>

```

Figure 3.4: Screenshot of a terminal window which is connected to the BUSCA main program. The output of the “status” command which displays all important status values, e.g. CCD status, temperatures, can be seen as well as the logging output of the background temperature update which indicates a stable evaporation rate of the dewars.

3.4 Special exposure types

3.4.1 Focus exposures

To find the best telescope focus the observer can use an implemented automatic focus procedure. In the focus exposure dialog (see Fig. 3.5), opened from the submenu *Exposure* an initial focus position, a focus increment and the number of focus values as well as an exposure time and a shift value can be chosen. The shift value is the number of lines the CCD frame is shifted after each single exposure.

Using this routine the focus of the telescope is obtained in the following way: the telescope is pointed on a field containing several stars and the default focus value is set. Between every exposure of the sequence the telescope focus is incremented and the CCD frame is shifted. Before the last exposure the CCD image is shifted twice, so the stellar images are separated from their neighbours by a twice as large distance on the frame. The image is then read out with the parameter given in the “Exposure parameters” section of the GUI. After the optimum focus is inferred, the observer can set the preferred telescope focus position with the implemented focus function from the *Telescope* menu of the GUI. As an example, Fig. 3.6 shows one focus image taken in May 2003.

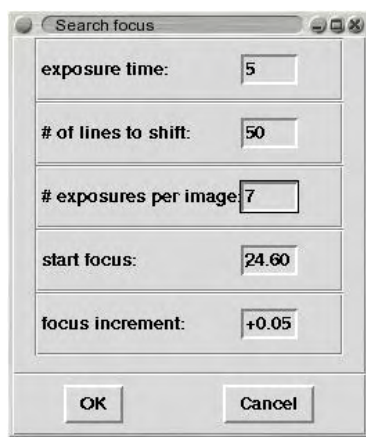


Figure 3.5: Dialogbox for the parameters for a focus exposure.

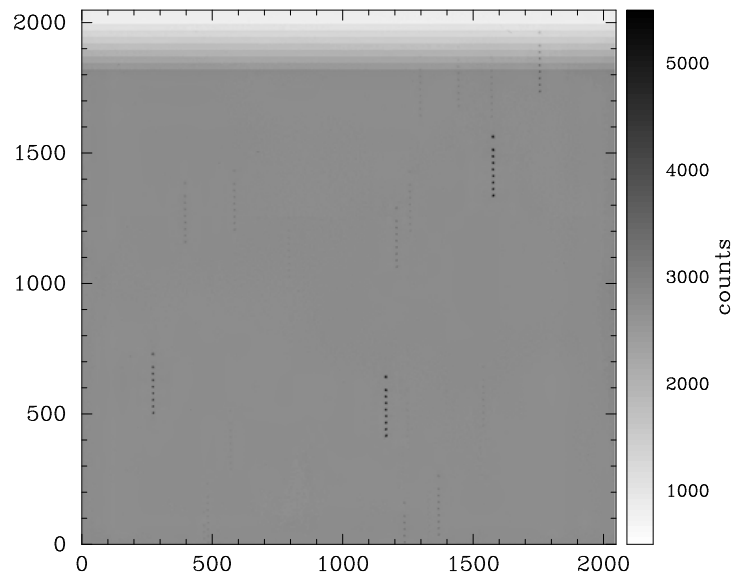


Figure 3.6: A sample image of a focus exposure. Each vertical line of objects is an image of a single star with different telescope focus positions. The steps in intensity at the top of the image signify the brightness steps and the movement of the image between each single exposures.

3.4.2 Sequence exposures

To obtain a multiband photometric lightcurve of, e.g., the variable sdB star PG 1627+017 (similar to PG 1605+072, see Ch. 7) using an automated observing sequence with BUSCA would be convenient and efficient. Until the observing run in May 2003 it was not possible to obtain these kind of time sequences with more than one filter set automatically with BUSCA. So a new complex exposure type was created which allows to take image sets with different filters and individual exposure times.

The observer has to setup this observation mode with the sequence dialog box (see Fig. 3.7) opened from the submenu *Exposure*. First the the number of different exposure configurations (= number of images per image set) has to be set. The maximal number is limited to four which should be sufficient for all observation strategies. Each configuration is defined by a filter set and an exposure time. Exposure times can be set individually or global for all configurations or relative to each configuration. In the latter mode for each configuration a fraction of the global exposure time has to be given. This is

useful e.g. when changing from the BUSCA broadband to the Strömgren filters. Then only the global exposure time has to be changed in the case of a poorer transparency.

To activate this observing mode the observer has to select the *Seq.* button in the “Exposure parameters” section of the GUI and then press the *Start Exposure*-button. The number of exposures in this section now describes the number of image sets. Starting this sequence mode for each configuration the chosen filters are selected and an exposure with the given exposure time is taken.

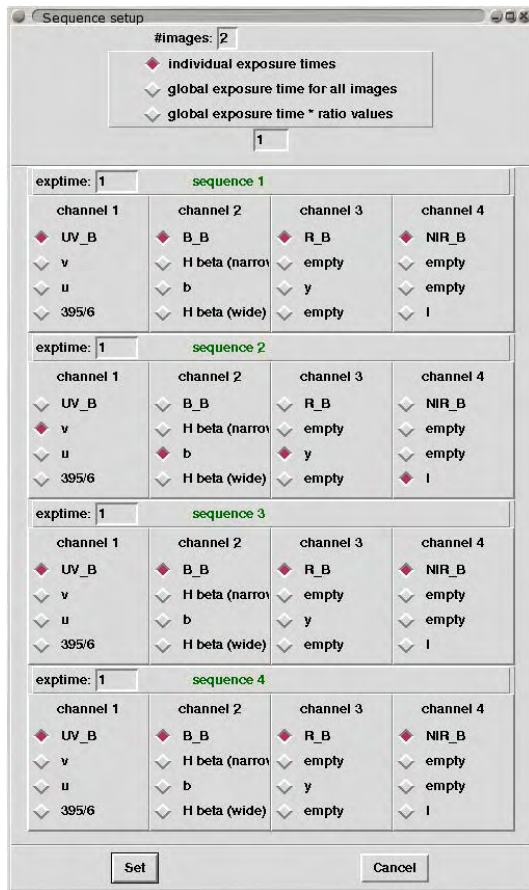


Figure 3.7: Dialog to enter the parameters for the sequence mode. The user can select the number of different exposure configurations and the global exposure time (top). Filters and individual exposure times filter can be defined for each exposure configuration.

4 Data and data reduction

The data which are used in this work were mainly obtained in four observing runs at the Calar Alto observatory between April 2000 and May 2001. Some of the data used for the performance verification (see Sect. 5) were additionally taken in the laboratory of the Sternwarte of the University of Bonn or at the Hoher List observatory near Daun/Eifel.

Before Feb. 2001 only a small $2k \times 2k$ (pixel size $15 \times 15 \mu\text{m}$) CCD chip for the ultra-violet was available. The CCD has a front side UV sensitive coating (Lumogen) which enhances the quantum efficiency of the CCD in the ultraviolet and the blue to 10-15%. The field of view of this CCD is only $6' \times 6'$ and is located in the centre of the $4k \times 4k$ CCDs. In Feb. 2001 a thinned ultraviolet sensitive $4k \times 4k$ CCD was installed in BUSCA to complete the CCD set of BUSCA.

The first part of this chapter describes the basic data reduction, the transformation of raw images into usable science frames, consists of three parts: bias correction, flat field correction, and the correction for bad pixels. This reduction is a kind of standard reduction which is well established in optical astronomy. For the data reduction the astronomical package IRAF “*Image Reduction and Analysis Facility*”¹ was used. In the second part, the data reduction steps necessary for the globular cluster data analysis are described. It deals with the PSF photometry, star pairing and photometric reduction.

4.1 Basic data reduction

4.1.1 Bias correction

In this section the bias correction, one major part of the CCD data reduction (see See 4), is discussed. The bias (for each pixel) plays an important role whenever electronic effects influence the science frames.

During the readout process the number of electrons in a pixel of the CCD is converted into a digital number. In this process it is electronically necessary to add a small voltage to the analogue signal from the CCD. This also assures that the CCD controller produces only positive values. Otherwise without this offset the noise which is caused by the electronics can lead to negative signals. These signals need a elaborate hardware to convert into digital numbers. This small voltage is visible in a science image as an offset to the value of each pixel, the bias value. This offset has to be corrected, because it pretends light which is not present. Normally the bias value is constant for all CCD pixels.

The bias value can be determined statistically with a bias image or with the overscan or prescan region of a science frame. A bias image is a dark image with an exposure time of 0 s. Overscan or prescan regions are no physical regions on the CCD. To achieve the overscan region the controller reads more pixels per line than physically present. Some CCD/controller combinations allow to read dummy pixels ahead of physical pixels. This region is called prescan region. All dummy pixels show the same behaviour, so the bias value can be derived statistically. The standard deviation represents the CCD readout noise.

¹see <http://iraf.noao.edu>

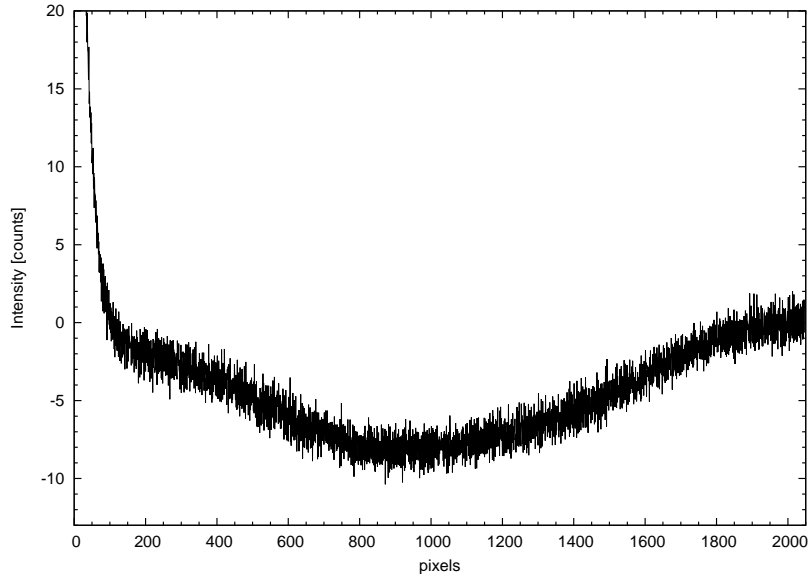


Figure 4.1: The line bias structure in x-direction with an amplitude of nearly 10 counts found in the masterbias of channel b. The scatter of ~ 1 count in the profile is due to the readout noise in the image.

During this work with BUSCA it turned out that the bias value was not constant over the whole CCD chip. However, these bias structures are stable for each image during a typical observing run of a couple of days.

Two primary bias effects are observed during the test phases. One effect has a “sinusoidal” structure with an amplitude up to 10 counts in the blue channel. In the other channels the amplitudes are smaller but also in comparison to the typical readout noise of a few counts the effect is not negligible. Fig. 4.1 shows a typical bias structure found in the masterbias (averaged bias frame) for the blue channel. The explanation of this effect is interference of the digital part with the analogue part of the CCD controller. Whenever the charge of one pixel is digitised the data of the previous pixel are transferred to a computer. This “transportation” mechanism influences the voltages in the analogue part of the controller. As before, this effect is the same for each line so that it appears as a regular pattern. Unfortunately this problem cannot be solved with a controller fine tuning. Also the effect was only visible whenever all four BUSCA channels are read out simultaneously. The read out of one, two or three channels does not show any bias effects. The reason for this behaviour is unexplained and may depend on the controller architecture.

The other effect shows up as an additional gradient at the beginning of each CCD line. The reason for therefore is a slightly detuned control sequence. The small voltage which is added to the analog signal is not constant during the read out process of the serial register. Since the same control sequence is used for all lines the effect is visible as a gradient in each line. Typically the bias level for full frame images decreases for the first 30-100 pixels of the line and stays constant afterwards. This effect was almost eliminated by the time the fine tuning of the CCD electronics was complete. The masterbias used for Fig. 4.1 was taken before the fine tuning. In this case the bias level decreases the first 100 pixels before the sinusoidal structure was overlayed.

There exist different techniques for the correction of all these bias effects. In the standard procedure single bias frames are combined to one masterbias which then has to be subtracted from each flat or

science frame. The main disadvantage of this method consists of the CCD readout noise, since the noise will decrease by only a factor of \sqrt{N} (N is the number of the bias frames used) combining several bias frames. In a second method an artificial bias frame is created which fits to all bias structures without noise. This artificial frame replaces the masterbias. This latter method is described in detail in Appendix B. As an example Fig. 4.2 shows the artificial bias frame generated for the yellow-red channel.

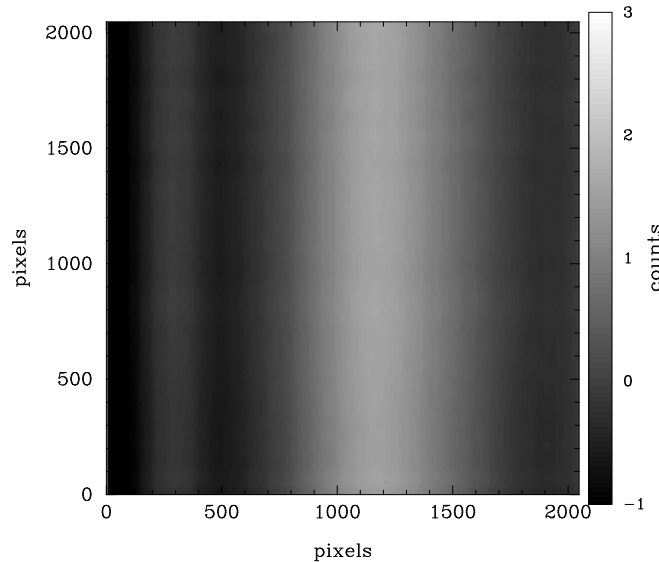


Figure 4.2: Example artificial bias frame for the BUSCA yellow-red channel. The wave like pattern in x-direction with an amplitude of 3 counts is clearly visible in the middle of the image.

4.1.2 Flat-field correction

Another important step in the data reduction of science frames is the flat fielding process. Using flat field images one can correct for different pixel sensitivity and for several optical effects like vignetting or dust which influence the light passing through the instrument.

One characteristic property of CCDs is the fact that each pixel has an individual sensitivity. The variation of the sensitivity can be intrinsic due to inhomogeneities in the CCD raw material or may be caused in the production process e.g. during the thinning of blue sensitive CCDs. Another cause which gives similar effects are dust particles on the optical elements in the instrument. These are not lying in the focal plane and produce unfocused images with ring or “doughnut” like shapes. These rings are caused by particles on the filters and on the CCD window. Figure 4.3 shows a typical flat image of the glass filter taken with the thinned $4k \times 4k$ CCD in the UV channel. Sensitive areas of the CCD appear brighter in this image in comparison to the insensitive darker parts. One can also see the “dust rings” over the whole image. The large structure at the bottom of the image is caused by the thinning process of this CCD.

To correct all the described effects twilight sky flat images or dome flat images are taken. This has to be done before and after an observing night, because more dust can fall into the instrument. These flat images are combined to a master flat image and each bias corrected science frame is divided by this master flat.

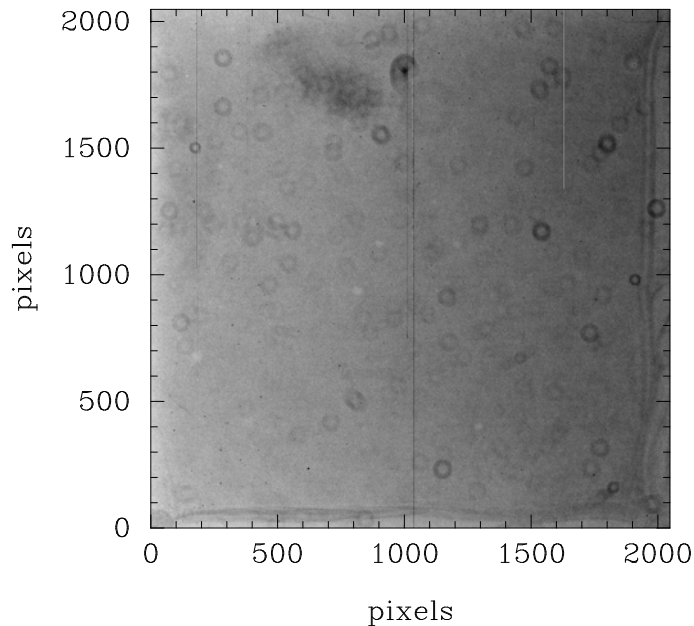


Figure 4.3: This picture shows the flat image taken in the UV channel with the UV_B filter. The brighter areas indicate CCD parts which are more sensitive than the darker areas. Many doughnut rings are visible indicating a lot of dust particles on the filter and on the CCD window. Note that the brightness levels presented lie between 18000 and 22000 counts while a CCD can reach a maximum of 65000 counts.

4.1.3 Bad pixel correction

Pixels which show a non normal behaviour are called “bad pixels”. Typical types of misbehaviour are:

- non linearity; the ratio of the pixel value of two frames is inconsistent with the exposure time ratio
- “hot” pixel; the pixel produces charges from an error in the CCD. This pixel is typically the lowest one of a bad column. For all other pixels above this bad pixel additional charges are produced when those charges are moved over this broken part of the CCD. In the resulting image it seems that there exists a column of “hot” pixels.
- “cold” pixel; the pixel does not detect any light or is very insensitive or works like a charge-hole. On some CCDs there are also bad columns with no charge, because the charges are moved into this charge-hole during readout.

Images can be corrected for bad pixels during the standard reduction in which the flux of this pixel can be interpolated with the flux of surrounding good pixels. Therefore a bad pixel mask is created from flat images with different intensities which are divided by each other. Pixels which show a non normal behaviour can be identified easily in this image. This mask is typical for the particular CCD and changes only slightly over months². Figure 4.4 shows one example of a bad pixel image from

²This is true for most instruments mounted on ground based telescopes. The bad pixel masks e.g. for the CCDs on board the Hubble Space Telescope can vary from day to day. This is caused by a high cosmic-ray flux which can destroy or

the small $2k \times 2k$ CCD used in the BUSCA UV channel during the test phases. The number of bad columns for this CCD is high and not typical for CCDs. The central columns are useless for the data analysis and therefore had to be masked out. However, the presently used $4k \times 4k$ CCDs have very few bad pixels and columns (less than 0.1% of all pixels).

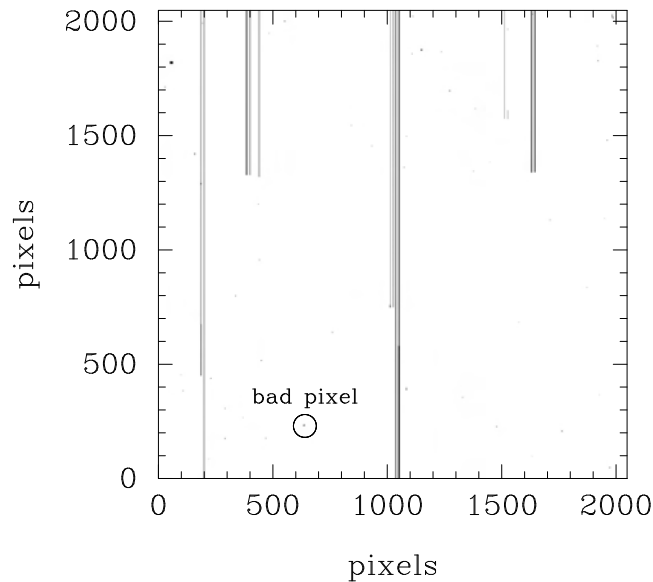


Figure 4.4: An example of a bad pixel image of the early $2k \times 2k$ CCD in the BUSCA UV channel. This CCD has a large number of bad pixels and columns in particular in the centre of the CCD which makes the central region unusable. The circle marks one small area which contains a few bad pixels.

paralyse a pixel. Paralysed pixels can again become good pixels after a certain time.

4.2 Globular cluster photometry

For the analysis of the globular clusters photometric data obtained in Sep. 2000 at the Calar Alto observatory was used. Images were taken in the Strömgrenfilters v , b and y . Additionally, to take advantage of all four BUSCA channels the Cousins- I filter was put into the near-infrared channel. For each target a short exposure and two or three long exposures were taken. The short exposures are necessary for the bright foreground or bright red giants stars of the cluster, which may be saturated in the long exposures. The I -frames were not useable, because most of the stars in the long exposed as well as in the short exposed frames are overexposed. Additionally the sky illumination from the moon was very high rendering these frames useless.

4.2.1 PSF photometry

After the basic data reduction of the globular cluster science frames the typical three available science frames with identical exposure time were stacked. This reduces cosmic ray events on the frames and improves the signal to noise ratio.

Then a PSF (Point Spread Function) photometry was performed with the DAOPHOT II package (Stetson 1991) running under the IRAF environment. In the first step stars with a positive identification signal higher than the determined background variation were detected. From this sample PSF stars were selected automatically by the software and manually proofed to be good sample stars for a uniform PSF for the science frame. From these stars a model PSF was generated and as a last step fitted to each prior detected star.

Additionally to frames with long exposure times (900 s) for each target also a short exposure was available. On these only the bright stars, which are typically overexposed on the long exposed images, show up and none of the faint stars. The bright stars from the short and the faint stars from the long exposed images are then combined to one list.

As to the CTE-effect (see Sect. 5.4.2), the calculated PSF from the DAOPHOT program to fit magnitudes was monitored carefully. Fortunately this PSF does not show variations over the frame, nor other surprising features. Stars lying in areas of reflections (see Sect. 5.3.2) or misidentifications were sorted out by selecting only stars with small errors.

4.2.2 Star pairing

After the PSF reduction the stars in the different filters have to be identified and matched to one catalogue. Typically this star pairing is an easy task, because the position of a star (x, y) on the CCD frame does not change significantly during successive observations. So the star pairing task has to perform only a simple position identification to combine the magnitudes for each star derived from the various exposures.

For BUSCA, however, the star identification is not that simple. The problem is caused by the optical arrangement of the four CCDs. The optical centre in each channel is shifted by up to 100 pixels in every direction. Also some dewars are rotated against each other.

A linear transformation is necessary to perform an accurate identification especially for crowded star fields (e.g., globular clusters). For BUSCA a first order linear transformation which provides rotation and translation is used. Scaling is not essential in this case since all CCDs are lying in the same focal plane. In Eq. 4.1 star coordinates (x, y) are transformed into (x', y') of another CCD frame. High order linear transformations do not yield to better results and are not used in this work.

$$\begin{pmatrix} x' \\ y' \end{pmatrix} = \begin{pmatrix} a & b \\ c & d \end{pmatrix} \begin{pmatrix} x \\ y \end{pmatrix} + \begin{pmatrix} e \\ f \end{pmatrix} \quad (4.1)$$

An automatic algorithm was implemented to determine the transformation parameters using the analytic solution of this equation (see Appendix C). As a first step a minimum of six stars has to be identified optically to generate a star transformation. With these parameters the program tries to identify as many stars as possible in a given error circle of typically one pixel radius. This set of stars provides a new transformation which is used again to identify the stars. Typically in this step further stars will be matched which were left out before, because their coordinates lay outside the identification circle. This recursive algorithm stops working if no additional stars can be identified.

4.2.3 Photometric calibration

For calibration of the science frames several standard stars were observed over the night. One problem with the calibration using the Strömgrenfilter system is the lack of standard fields in the northern hemisphere. For observations on the southern sky there exist several well known E-region standard fields with accurate photoelectric $uvby\beta$ photometry (e.g., Jönch-Sørensen (1993)). In this work a sample of Strömgren standard stars from Perry et al. (1987) was used. This catalogue contains mostly bright stars, so only the “faintest” were chosen as standard stars. Also these stars must be observed individually which is quite time consuming. The typical exposure time for these stars was between 0.01 and 1 s Instrumental magnitudes are then obtained by applying aperture photometry on the standard stars. The diameter of the chosen aperture was 32 pixels (corresponding to 11 arcsec) to ensure the star is completely inside the aperture. To calibrate the instrumental magnitudes the following equations were used:

$$y_i = y_0 + z_y + k_y \cdot X + c_y \cdot (b - y)_0 \quad (4.2)$$

$$b_i = b_0 + z_b + k_b \cdot X + c_b \cdot (b - y)_0 \quad (4.3)$$

$$v_i = v_0 + z_v + k_v \cdot X + c_v \cdot (v - b)_0 \quad (4.4)$$

y_i , b_i and v_i are the instrumental magnitudes, z stands for the zero point, k for the extinction coefficient in combination with the airmass X and c for the colour term. All other magnitudes are taken from the standard star catalogue. After performing the calibration for each night it became visible that for most of the nights the observed y magnitude in the beginning was smaller ($\sim 20\%$ of the flux were lost) than at the end of the night. The only reasonable explanation of this effect is the change of the zero point in this channel in combination with some electronic problems with the CCD controller. The effect was not reproduceable afterwards in the laboratory nor appeared in the following observing runs. Also unphotometric conditions which were not seen in the other bands can explain this lack of flux. So all such faulty y magnitudes were excluded from the calibration.

Since all PSF magnitudes are smaller than the aperture magnitudes, they need to be corrected. This shift based on the fact, that the PSF magnitude is calculated out of the integral flux (up to infinity) of the PSF model generated from the PSF stars. To calculate the PSF-aperture shift aperture photometry was applied on a sample of stars in each science frame. Ideally, the aperture diameter should be the same as for the standard stars used for the calibration. Unfortunately, the seeing in each science frame was different, so the aperture diameter of 10 pixels for the standard stars was not usable the science frames. To find the optimum aperture for each science frame, stars were selected which have no nearby neighbours. For these stars magnitudes for apertures with different radii were calculated

and the magnitudes were plotted against the aperture radius. From this curve of growth the optimum aperture radius can easily be determined. Fig.4.5 shows an example of the data reduction of M71 with an optimal radius of 10.2 pixels.

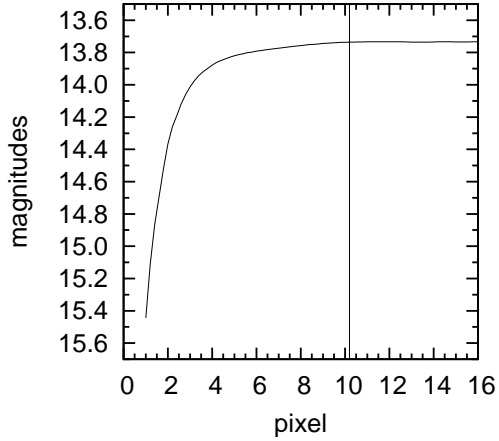


Figure 4.5: Curve of growth of the brightness aperture of a sample star in the M71 field. The enlargement of the aperture radius leads to smaller magnitudes until the optimal radius of ~ 10 pixel is reached. From this point on the star is completely encircled by the aperture.

Aperture photometry with this radius was applied to all stars with no nearby neighbours on one science frame. Then the difference between the PSF and aperture magnitude gives the PSF-aperture shift for this science frame.

Tab. 4.1 gives all calibration parameter for the globular cluster data reduction in this work for the days 04./05./06. Sep. 2000.

Table 4.1: Calibration parameters for the 04./05./06. Sep. 2000 with zero-points z , extinction coefficients k , colour terms c and the PSF-aperture shift.

	04.09.2000			
filter	z	k	c	shift
y	4.378 ± 0.005	0.310 ± 0.062	-0.014 ± 0.003	-0.023 ± 0.001
b	3.774 ± 0.005	0.117 ± 0.066	-0.014 ± 0.008	-0.023 ± 0.001
v	4.043 ± 0.006	0.085 ± 0.001	-0.028 ± 0.017	-0.034 ± 0.001
	05.09.2000			
filter	z	k	c	shift
y	4.555 ± 0.017	0.174 ± 0.014	-0.055 ± 0.008	-0.038 ± 0.005
b	3.531 ± 0.024	0.225 ± 0.020	-0.010 ± 0.012	-0.013 ± 0.006
v	3.719 ± 0.044	0.241 ± 0.038	-0.078 ± 0.017	-0.020 ± 0.007
	06.09.2000			
filter	z	k	c	shift
y	4.606 ± 0.009	0.145 ± 0.011	-0.055 ± 0.017	-0.084 ± 0.005
b	3.576 ± 0.003	0.225 ± 0.026	-0.019 ± 0.007	-0.002 ± 0.006
v	3.644 ± 0.005	0.345 ± 0.007	-0.044 ± 0.011	-0.064 ± 0.055

5 BUSCA performance verification

5.1 Introduction

After the completion of BUSCA the instrument has undergone a large number of tests to verify the readiness for the 2.2m telescope at Calar Alto observatory. The main tests such as the determination of the CCD parameters and the shutter performance were done in the laboratory in Bonn and at the Hoher List observatory. During the first test runs at Calar Alto the optical quality and the overall performance of the BUSCA instruments were checked. The stability of colour indices obtained simultaneously during bad weather conditions was somewhat difficult to check. The reason was the lack of bad observing conditions (a situation which no observer wants to have, because observing time is rare), in particular clouds which are passing over the telescope. Fortunately, longterm observations at Hoher List and Calar Alto provided two opportunities to perform this test and they gave good results.

All tests are described in detail in the following sections.

5.2 Exposure uniformity

The next step in the BUSCA science verification is the evaluation of the quality of the Bonn shutter in regard to a homogeneous illuminated CCD frame at short exposure times. For that purpose several flat images were taken in the laboratory with the same light source. Because the moving direction changes after each single exposure, for each direction one image is used. Nonuniformity is expected due to mechanical and electrical limitations only at very short exposure times. The exposure times ranged from 10 s down to one 1 ms. Every image, bias corrected, was divided by the 10 s image. This exposure time was chosen because at 10 s and longer nonuniformities are below the detection limit. Since nonuniformity effects should be only in the direction of the moving shutter blades, which is the y-axis of the CCD image, all columns were averaged to reduce the influence of noise.

The results are shown in Figure 5.1 in which the variation of the mean intensity is plotted versus the row numbers of the CCD. At an exposure time of 100 ms no nonuniformity over the CCD x-axis is measurable. The nonuniformity at 10 ms is less than one percent and about 10% at 1 ms.

The forward and reverse motions of the shutter blades show no effect on the results.

From experience at Calar Alto the smallest exposure time used for sky flats and bright standard stars was 50 ms, so for all practical exposure times the shutter works perfectly and no correction images for shutter effects are necessary.

5.3 Optical quality

In this section the analysis of the optical quality of BUSCA is discussed. The main focus is on the shape of the PSF (Point Spread Function), the CCD performance (e.g., CTE), and reflections seen in the CCD frames.

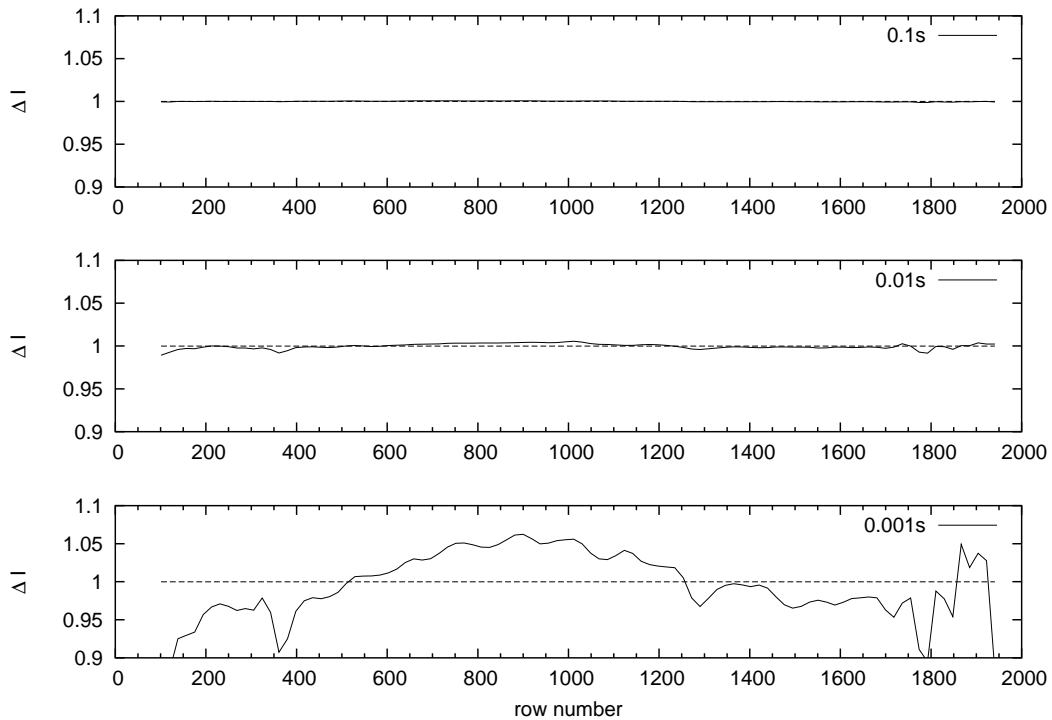


Figure 5.1: The relative intensity ΔI plotted versus the row number (parallel to the moving direction of the two shutter blades) for different exposure times of 100 ms (top) down to 1 ms (bottom). The exposure inhomogeneity is at 1 ms about 10% and at 10 ms $<1\%$. Smaller variations in the bottom diagram are due to noise at 1 ms as well as bad pixels which cannot be reduced completely.

5.3.1 The PSF

As a first test for the optical quality the PSF (Point Spread Function), i.e. the image of a point source, was analysed. A constant PSF which does not depend of the x,y -coordinate on the CCD is desirable. Any variable PSF can cause unpredictable errors in the photometry. Tests on several images under different seeing conditions indicate that the PSF does not change over the CCD field. Nevertheless under good seeing condition of less than $1.3''$ the PSF shows some “curious” behaviour in all channels. The PSF (see Fig. 5.2) is slightly symmetrically elongated in approximately left-right direction. Technical information of the 2.2m telescope indicates that the telescope oscillates in east-west direction. Fig. 5.2 shows a sample PSF for the near-infrared channel from the data reduction of the Globular Cluster M3 (see Sect. 4.2.1). Using the USNO-A2.0 catalogue¹ (Monet 1998) as an astrometric reference the determined small rotation angle of $\sim 7^\circ$ of the PSF is compatible with the position angle of the CCD, which is not perfectly east-west aligned.

5.3.2 Reflections from bright stars

Bright stars outside of the BUSCA field can cause reflections which are visible in the CCD field. Fig. 5.3 shows as one example these reflections at the lower left part of the image. The reflections are typically seen in all channels, so that the reflection must take place in front of the beam splitter. On

¹A catalogue of astrometric standards of the United States Navy Observatory

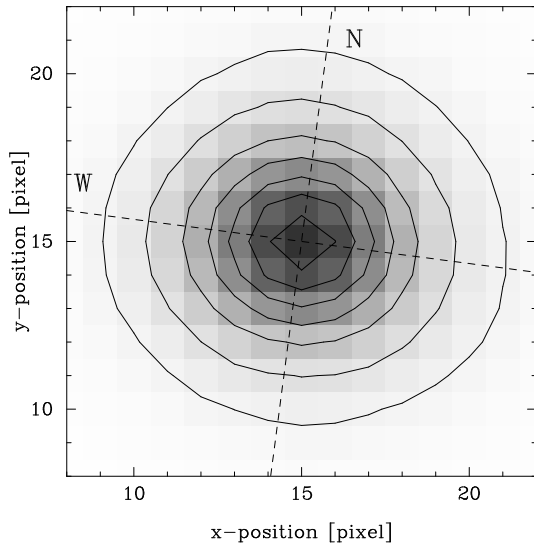


Figure 5.2: Sample PSF in the near-infrared channel of BUSCA. The contour plot indicates an elongation ($\epsilon=0.058$) due to small telescope movements in east-west direction. The dashed cross signifies the north-west orientation of the image. In general, the dewars are not perfectly aligned with RA & DEC. In this case there is an angular offset of $\sim 7^\circ$.

the other hand, a few reflections are visible in only one channel. In this case the bright star is reflected inside the dewar. The points and components which cause the reflections are not clear, a head of a screw inside the light beam or in the dewar is possible.

The important question is how reflections influence the photometry. In case of the PSF photometry (see Sect. 4.2.1) the reflections do not play an important role. The reflection itself is not detected as a stellar object. The reflections lead only to a variable sky background which can be compensated for by the IRAF reduction software. Aperture photometry does not work reliably in the affected region.

5.3.3 Star ghosts

Another type of reflections is also seen in some images. A Saturn like picture can be found 260 pixels (2×2 binning mode) down and five pixel to the left of a very bright (e.g., overexposed) star. These “ghost” images come from a secondary reflection at one beam splitter in the BUSCA cube (see Sect. 2.1). Normally the light is reflected at the front layer of the dichroic plate. Although the back side surfaces are anti-reflection coated a small fraction of the transmitted light beam is reflected. From the geometry of the beam splitter the reflected beam has an offset of 7 mm to the original beam which results in a distance of about 260 pixels on the CCD between the star and its reflection. Also the “ghost” is quite out of focus which is shown by the Saturn like shape. The flux ratio from the “ghost” and the real object is of about 0.25%. For stars which are not overexposed the “ghost” is usually not visible. Since the ghosts are not typical objects the PSF photometry and also the aperture photometry are not influenced.

5.4 CCD characteristics

5.4.1 Noise, fullwell and conversion factor of the CCDs

The most important parameter of CCD astronomy is the limit noise of the measured signal poses for the photometry. In addition the gain and fullwell of a CCD are important to define the maximum possible exposure time. The dark current, as mentioned in Sect. 2.4, can be neglected since the CCDs

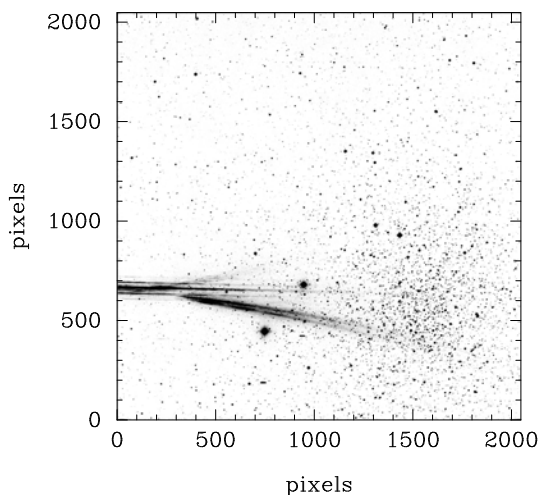


Figure 5.3: Image of the globular cluster NGC 6366 in the yellow-green channel. The streaks at the lower left are reflections inside BUSCA coming from bright stars outside the CCD field.

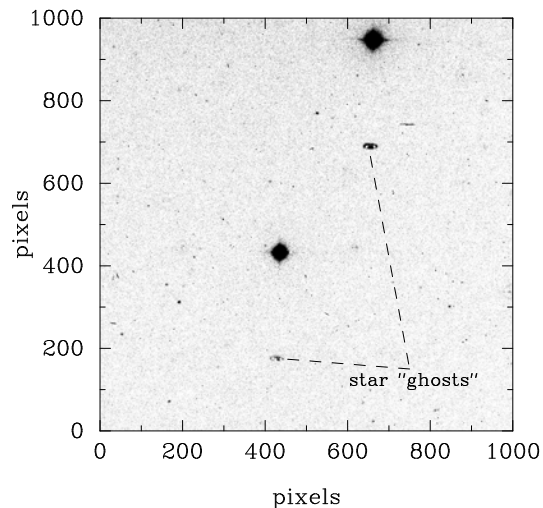


Figure 5.4: This image shows “ghosts” pictures of the two overexposed bright stars. The “ghosts” are coming from secondary reflections in the beam splitter. The flux ratios of the ghosts to the stars are $\simeq 0.25\%$.

are cooled down commonly to -100° or below.

The noise, seen as the standard deviation in the data frames, can be divided into three parts, the photon shot noise, the read-out noise (RON) and “pixel response non uniformity” (PRNU).

Photon shot noise is a fundamental property of the quantum nature of the light. According to quantum theory the number of the infalling photons I and the induced electric charges will exhibit a Poisson distribution. The standard deviation of the noise equals the square root of the corresponding flux.

Noise from the preamplifier on the CCD and the analog signal chain in the CCD controller are called read-out noise (RON) and depend on the CCD read-out speed. The BUSCA CCD controller is tuned for less RON and fast read-out speed. All four $4k \times 4k$ CCDs can be read out in 500 seconds. Because the typical seeing at the Calar Alto Observatory is larger than $0.9''$ (corresponding to 5 pixels) the BUSCA standard observing mode is to read out the CCDs in a 2×2 binning mode. This mode combines 2 physical pixels to one image pixel and 2 lines to one line, respectively. It provides an acceptable sampling and gives a pleasantly short read-out time of 260 s. The best read-out noise measured lies between 6 and 10 electrons (see Tab. 5.1).

There is no possibility to avoid the photon shot and read-out noise.

The “pixel response non uniformity” (PRNU) is caused by different responses of pixels to the incoming photon flux. The response varies from pixel to pixel leading to a non-uniformity across the CCD. The behaviour of this effect is similar to incoming flux variation caused by dust on optical elements in the light path such as filter or CCD dewar window². Since the non-uniformity is constant for each pixel, the effect can be corrected for by dividing the image with a normalised flat image.

All noise components can be summarise by the following equation:

$$\text{Noise}_{e^-}^2 = \text{RON}_{e^-}^2 + I_{e^-} + (\text{PRNU} \cdot I_{e^-})^2 \quad (5.1)$$

²Normally dust causes diffuse so called flat field structures in comparison to PRNU pixel effects.

Beside noise the fullwell of a CCD is of special interest. A CCD enters a state of fullwell, when a single pixel is no longer able to accumulate charge. Any further charge generated by incident light will spill over into close-by pixels containing less charge, primarily along columns. This effect is known as “blooming” and is usually caused by overexposed objects. Region which are affected by blooming cannot be used for further analysis. There exist anti-blooming techniques (see Kohley 1998) but none of them are implemented in the CCD controller of BUSCA.

The last CCD parameter which should be mentioned in this section is the conversion factor (CF). The number of measured electrons of each CCD pixel is transformed to an analogue voltage value by the CCD on-chip amplifier. This signal has to be converted into digital units (ADU) by an analogue-to-digital converter. The gain g of all amplifiers is set in such a way that the maximum value delivered by the typically 16-bit converter (range from 0 to 65535) is encountered at signal levels less than in fullwell state. The conversion factor is given in electrons/ADU.

For measurements of the CCD quantities flat image pairs (two images with the same exposure time) with different exposure levels were taken and bias corrected. Both images from each pair were subtracted by each other which corrects for the “pixel response non uniformity” (PRNU). Starting with Eq. 5.1 the standard deviation only depends on the RON and the photon shot noise:

$$\text{RMS}_{e^-}^2 = \text{RON}_{e^-}^2 + I_{e^-} \quad (5.2)$$

Multiplying with g^2 transforms this equation into ADU. Thus:

$$\text{RMS}_{\text{ADU}}^2(I_{\text{ADU}}) = \text{RON}_{\text{ADU}}^2 + I_{\text{ADU}} \cdot g \quad (5.3)$$

The noise of each image can now easily be measured by taking the standard deviation of the before subtracted flat image. Assuming a Gaussian distribution of the two source images the variance has to be corrected by a factor of $1/\sqrt{2}$ to get the value of the real noise. If this corrected variance is plotted against the intensity in logarithmic scale one gets the following typical diagram, the CCD “Transfer Curve” (see Fig. 5.5). As can be seen the noise increases with intensity which is the effect of the photon shot noise. At a certain intensity the noise drops rapidly indicating the full well state. As mentioned before the flux now spills over from “full” pixels into neighbouring pixels which are nearly full, reducing the variation from pixel to pixel. In a digital units transfer curve the slope in the region of increasing intensity and noise represents the gain (as seen in Eq. 5.3). The gain and therefore the conversion factor CF as well as the readout noise can then easily be determined.

Table 5.1: CCD characteristics of all BUSCA CCD’s

BUSCA channel	CF [e^-/ADU]	fullwell e^-	readout noise e^-
ultraviolet	3.13585	131500	9.58
blue-green	3.03402	121000	6.37
yellow-red	2.96736	155000	7.60
infrared	2.93033	128500	8.38

Table 5.1 shows the values for the conversion factor, the fullwell, and the read out noise for all BUSCA CCDs.

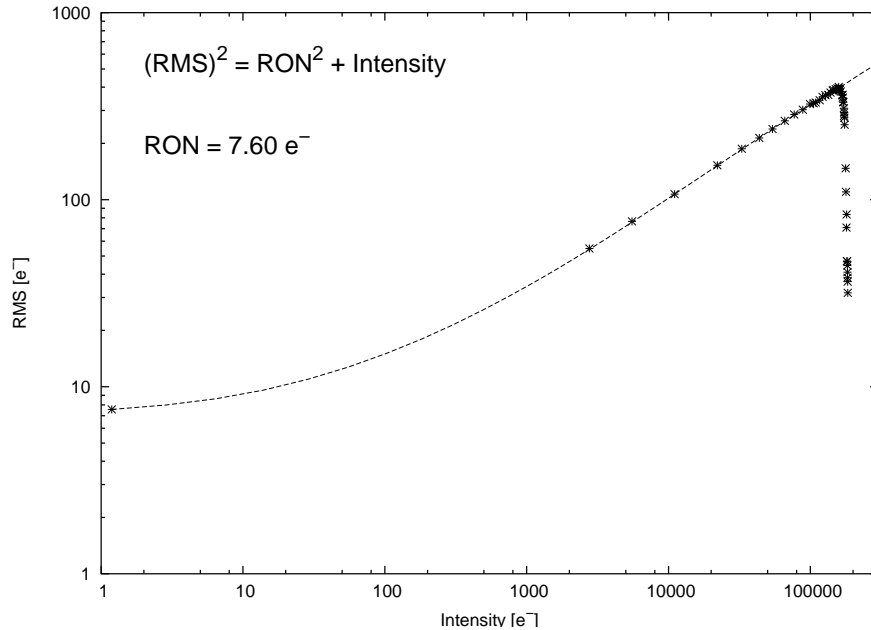


Figure 5.5: The behaviour of the RMS in relation to the intensity in logarithmic scale for the yellow-red BUSCA channel is shown. The intensity drops abruptly at the full well point of 155000 electrons. The dashed line is the fit of the linear slope in logarithmic scale. The determined CF is $2.96736 e^-/\text{ADU}$.

5.4.2 CTE effects

A major aspect of the BUSCA testing phase was to check the behaviour of the CCDs under observing conditions and to optimise the performance of the CCD system. The major attention was turned to the thick CCDs in BUSCA which have, as mentioned before, a non perfect CTE (Charge Transfer Efficiency), in particular the CCD used in the near-infrared channel. The thinned CCD mounted in the ultraviolet channel is a second generation $4k \times 4k$ CCD which has a good CTE.

The CTE characterises the efficiency of the transport mechanism when moving a charge packet from line to line (vertical CTE) or from pixel to pixel in the serial register (horizontal CTE) during the readout process. Preliminary studies by Harbeck (2000) of the thick $4k \times 4k$ CCDs show a non perfect CTE performance of the CCDs. He used a radioactive Fe^{57} source which produces single pixel events with a well defined count rate. These events can easily be used to measure the CTE statistically. The vertical CTE is nearly 1 but the horizontal CTE was found to be 0.99995 which means a flux loss of 18.5% after moving the charge 4096 times (read out of a pixel near the right border of the CCD). The lost flux is “smeared” over many trailing pixels. The CTE itself depends highly on the CCD operating temperature and the CCD control voltages. If a CCD is cooled down to -100° to avoid the dark current the CTE is getting worse. At a temperature of -30° the CTE is better but then the dark current is not negligible any more. The studies showed also that at lower temperatures (less than -120°) the CTE of the tested CCDs is better but this CCD state is much more critical in a physical sense (e.g. differential thermal expansion) which can cause a non repairable CCD damage. However, the CCDs in the blue and yellow-red channel are cooled down to -120° resp. -125° without any harm for the CCDs. The near-infrared channel CCD on the other hand is only working in a temperature range above -100° , because at a temperature lower than -103° the CCD lost its electric connection in its

package and is not useable.

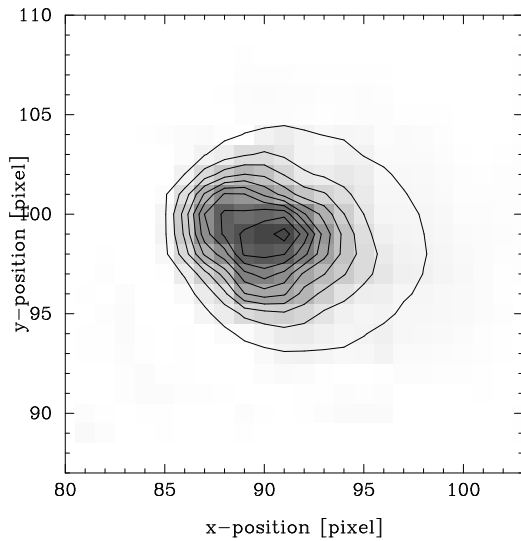


Figure 5.6: CTE effect of a standard star in the near-infrared channel of BUSCA. The PSF is somewhat rotated and elongated (as in Fig. 5.2) and then wider to the right caused by the CTE effect in x-direction.

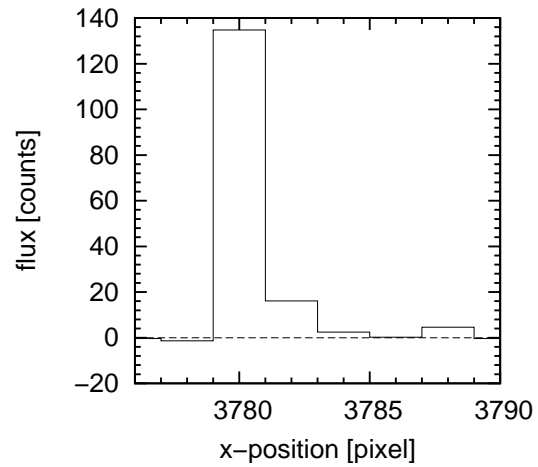


Figure 5.7: Flux distribution along serial readout direction of a single pixel cosmic event with CTE effect near the right border of the blue channel CCD. The determined CTE value of this cosmic of 0.99996 is compatible to the value of the radioactive Fe^{57} source.

In Fig. 5.6 the shape of one standard star in the near-infrared channel is displayed. The star is elongated due to telescope oscillations (see above) and additionally smeared to the right. The analysis of one single cosmic event in one of the science frames yields to the result, that the flux which should be concentrated in one pixel is significantly smeared over two additional pixels to the right (see Fig. 5.7). In this blue channel image the trailing pixel contains only $\sim 86\%$ of the total flux of the cosmic event which corresponds to a CTE value of 0.99996. This value is compatible to the CTE value determined with the Fe^{57} source. To get the whole flux of the cosmic event a small aperture of ~ 8 pixels (resp. $1.4''$ in non-binning mode) is sufficient. For aperture photometry at the 2.2m telescope at Calar Alto with a typical seeing value of about $1-1.5''$ with an usual aperture radius of 2-3 times of the seeing value the CTE effect is no problem for aperture photometry.

5.5 Colour stability

The last important test which was made with BUSCA was the testing of the colour stability under non-photometric conditions. To explain the photometric condition the measured or instrumental magnitude has to be defined. The instrumental magnitude V_{inst} is the apparent magnitude V affected by atmospheric extinction, and possibly a colour term c_V plus an instrumental offset of

$$V_{\text{inst}} = V + \text{airmass} \cdot \text{ext} + c_V \cdot (B - V) + \text{ofs}$$

where ext is the zenith extinction. The airmass is given relatively to the zenith, the shortest path length possible. Atmospheric extinction is caused by scattering or absorption of light by molecules or other particles. Most of the extinction in the visual window is due to Rayleigh scattering by air molecules. Another important contributor to the extinction is scattering and absorption by small liquid or solid

particles of various sizes called aerosols (e.g. Cousins & Caldwell 1998).”Photometric conditions” means, that the extinction value is constant for a long time period, e.g. hours or the whole night.

The idea behind the colour stability of simultaneous observations in different colour bands with BUSCA was the assumption that atmospheric extinction variations are “grey”. Variable extinction e.g. thin clouds (droplets, ice crystals), and dust can cause a non photometric observing condition in an otherwise clear night. Simultaneous observation then provides colour photometry with the same atmospheric extinction in all bands. The resulting colour index is the same as a colour index taken under photometric conditions. Furthermore the colour index should be stable if the photometric conditions are time dependant and changing during the night.

To explain this mechanism and to see the advantage of simultaneous photometry against “standard” photometry one can start with the observed magnitudes B and V which are taken at different times t_1 and t_2 :

$$\begin{aligned} B(t_1) &= B_{\text{phot}} + a_B(t_1) \\ V(t_2) &= V_{\text{phot}} + a_V(t_2) \end{aligned}$$

The values B_{phot} and V_{phot} describe the apparent magnitude under photometric conditions whereas $a_B(t_1)$ and $a_V(t_2)$ stand for the additional atmospheric extinction at t_1 and $t_2 \neq t_1$. All magnitudes should be airmass free. The resulting colour index $B - V$ can be written as:

$$B - V = (B - V)_{\text{phot}} + a_{(B-V)}$$

The colour extinction term $a_{(B-V)} = a_B(t_1) - a_V(t_2)$ is zero under photometric conditions because of $a_B(t_1) = a_V(t_2) = 0$. If the atmospheric extinction is variable this term does not vanish and absolute photometry is not possible. If on the other hand the magnitudes B and V are taken simultaneously, the extinction reduces the flux in all bands by the same percentage. This works only under the assumption that the extinction causing the flux loss is grey. In this case the variability of the extinction does not affect the photometry and the colour index $B - V$ is stable.

First tests made at Hoher List Observatory in 1998 offered the opportunity to check if the assumption of a grey extinction was right and the colour index remains stable. The left panel in Fig. 5.8 shows the Strömngren magnitudes (v, b and y) of a single star during a 70 minutes passage of a cloud which causes a flux loss of over two magnitudes. The simultaneous colour indices ($v - b$ and $v - y$) plotted in the lower part of the diagram show only small variations (max. 0.05 mag) while y varied over 2 mag. For comparison the colour index is plotted in the right panel as if the colour index were determined “classically” sequentially. This method obviously fails to give acceptable photometry.

During the observation of the variable sdB star PG1605+072 in May 2001 at Calar Alto observatory (see Ch. 7) several clouds passed the observatory, so it was also possible to study the colour stability there as well. Fig. 5.9 shows the lightcurve and the colour index $v - y$ of one of the comparison stars of PG1605+072 during a period of 195 minutes. The data were airmass corrected. The used extinction coefficient was determined from parts of the data taken in non cloudy periods.

Similar to the lightcurve presented before this lightcurve show maximum flux variation due to cloud extinction of 2 mag. Again the colour index $v - y$ shows only small variations (up to 0.06 mag during the maximum 2 mag cloud). As one can see the maximum deviation corresponds to the maximum flux loss (e.g., at 12 min) and the value of the colour index is reduced. This indicates that at this time the cloud changes the colour index only very slightly to the blue (at $E_V = 2$ mag) which disproves that the colour of the cloud is perfect grey. This topic and additional analysis is show in Ch. 6.

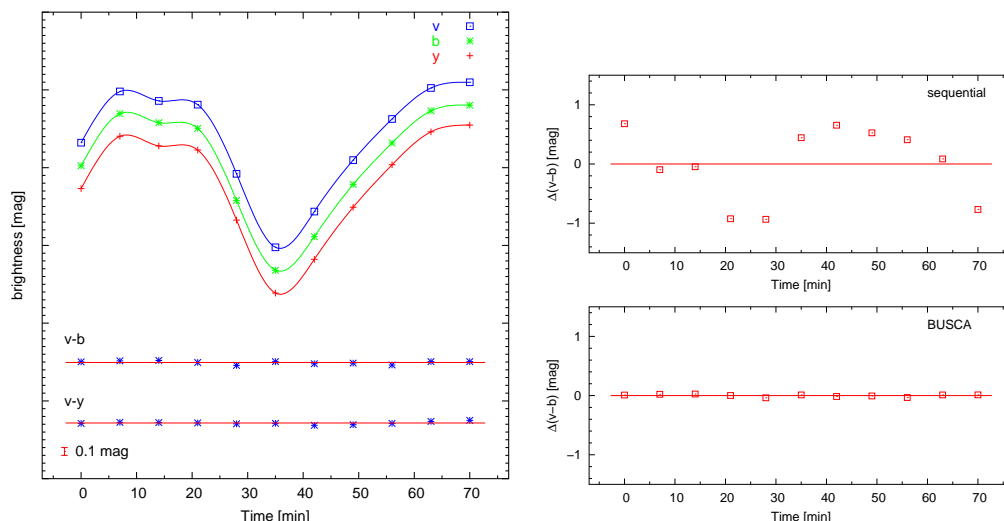


Figure 5.8: The lightcurve of a non variable star during a 70 min cloud passage over the telescope. In the lower left panel two Strömgen colour indices are plotted which show no significant variability. The right panel indicates the advantage of the simultaneous colour determination against the “classical” sequential method which shows a large deviation.

5.6 Summary and conclusions

After all test were passed the main conclusion is that BUSCA is working fine at the 2.2m telescope at Calar Alto observatory. The optical part of BUSCA results in images of good quality even though very bright stars in and outside of the BUSCA field cause reflections. From experience it is possible to adjust the telescope position to reduce the effect of reflections. “Star ghosts” are not avoidable but with the Saturn like shape of such reflection images they can be easily detected. The PSF photometry will not be influenced. The shutter is working fine and provides accurate short exposure times down to 0.01 s with a homogeneous illumination of the whole CCD. The test of the colour stability proves that simultaneous observing in four individual bands can avoid the effect of small and thin clouds. The variation of a determined colour index is reduced by a factor of more than 30 compared to the variation in each individual channel.

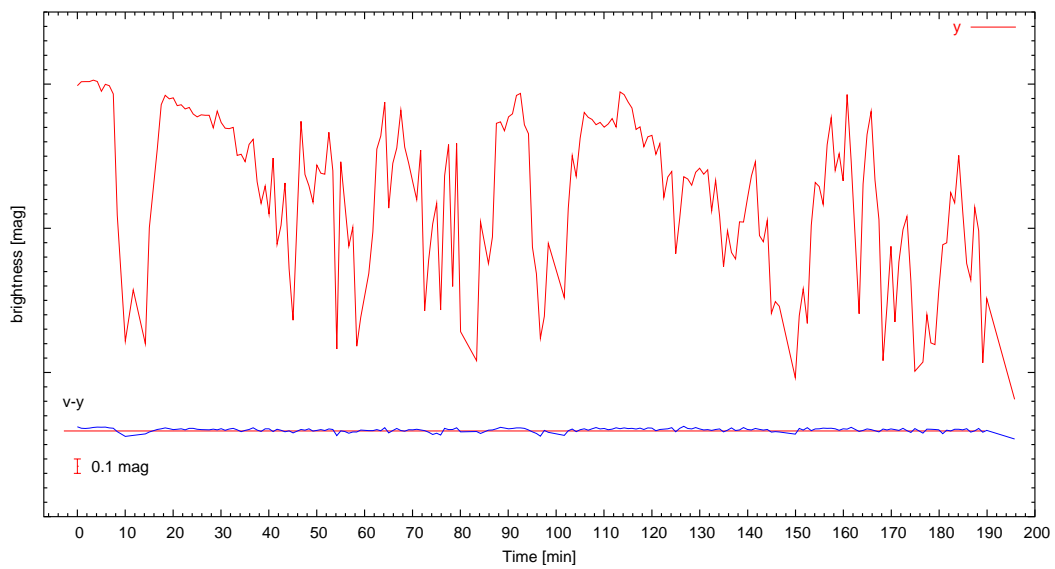


Figure 5.9: The upper part shows the y lightcurve of one of the comparison stars of PG1605+072. The colour index $v - y$ is below ± 0.06 mag while the y -magnitude varies by more than 2 mag.

6 Are clouds really grey? – Thick clouds observed with BUSCA

Analysing the data taken in the observing run in May 2002 at Calar Alto observatory – the target was the rapidly variable sdB-star PG 1605 – not only the colour stability but also the influence of clouds on the extinction could be investigated. For this work (as already described in Sect. 5.5) the fluxes of the two reference stars were used.

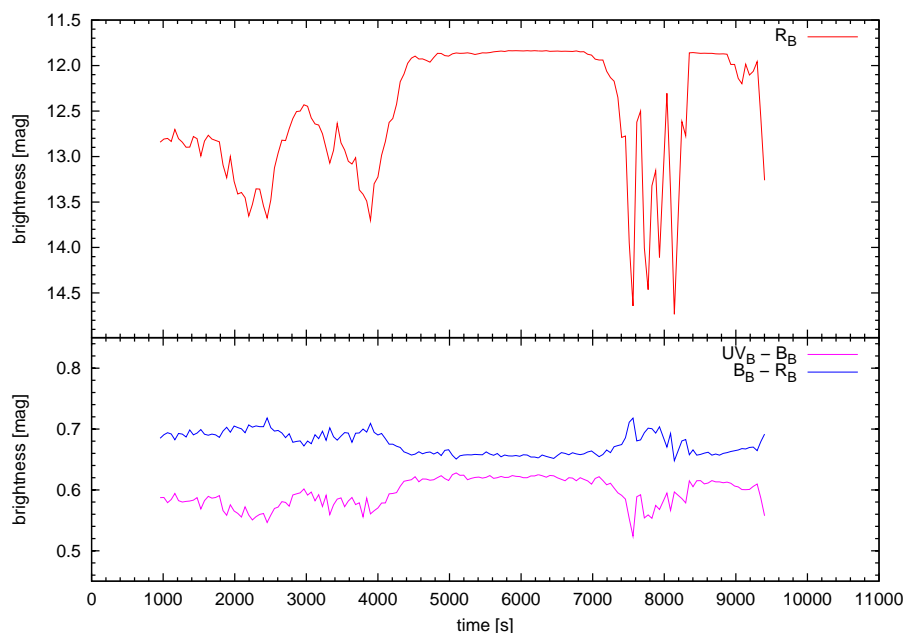


Figure 6.1: The summed light curve of the reference stars and the colour index curves $UV_B - B_B$ and $B_B - R_B$. Both curves are scaled with a factor of 5 and show clearly an anti-correlation in the behaviour during higher cloud extinction.

During these observations the colour index remained almost stable although the flux of the reference system varies up to 2 mag. Looking into the detail of the colour curve in comparison to the light curve, the variations of the colour curve concur with the peak depressions of the light curve. The first impression was that the colour index $B_B - R_B$ became redder whenever the cloud extinction increased. But on the other hand the colour $UV_B - B_B$ got bluer at the same time (see Fig.6.1). The amplitude of these variations is small (about 0.02 mag) but significant (at $\Delta V \sim 2$ to 3 mag). Thus, the prior assumption that clouds causing this extinction are grey is disproved at the 1% level. However, if the extinction is small then the change of the colour index is negligible and can in normal photometry be neglected.

6.1 Data analysis

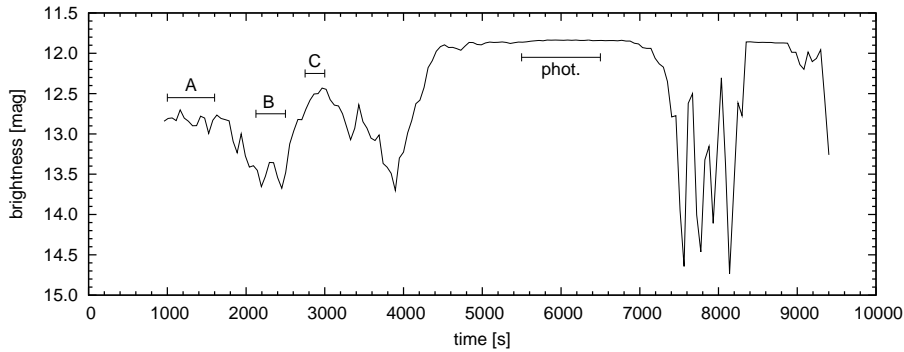


Figure 6.2: This diagram defines the time periods belonging to the “clouds” A,B and C. The period labelled with “phot.” is used as a reference period and shows no signs of clouds.

For a closer inspection of the extinction nature of the clouds, three time periods A, B, and C in the light curve (see Fig. 6.2) are defined. In each time period the strength of the extinction is different. A median flux in each time period for each BUSCA band was calculated. These flux values were transformed into the magnitude scale relative to the flux of a reference time period with little extinction. To obtain the deviation from the supposed grey extinction, the difference of the brightness in each band to the brightness averaged over the four BUSCA bands are calculated. Tab. 6.1 contains the time-definition of the cloud and of the reference period, the magnitudes for all BUSCA bands, and the grey magnitude. Fig. 6.3 shows the deviation of the magnitudes normalised to the grey magnitudes in a spectrophotometric kind of view. For a discussion of the uncertainties see the end of this section.

Table 6.1: Definition of the “cloud” periods A,B, and C as well as the extinctions determined for the BUSCA bands. The “phot.” period is used as a reference period without cloud influence. The right column shows the mean extinction of all clouds.

cloud	period [s]	UV [mag]	blue [mag]	yellow-red [mag]	near-infrared [mag]	[mag]
		“Extinction”				
A	1000 - 1600	0.991	1.030	0.995	0.997	1.003
B	2125 - 2500	1.661	1.725	1.677	1.685	1.687
C	2750 - 3000	0.697	0.727	0.704	0.705	0.708
phot. (no cloud)	5500 - 6500					

In principle all clouds show the same behaviour. Through clouds a star becomes significantly fainter in the blue band than in all other bands. The most interesting features are visible in cloud B. It has the maximum extinction of ~ 0.4 mag relative to the grey magnitude in the blue but the extinction in the ultraviolet is 0.15 mag lower than for clouds A and C. The extinction in the red and near-infrared bands is essentially identical to cloud A.

To characterise the colour of the cloud based on the observed colour indices, one could say that cloud B appears violet and faintly red. Cloud A shows the medium blue extinction and has a violet and red colour. In comparison Cloud C has the smallest blue and the highest red extinction and the colour is

bluer than the colour of cloud A.

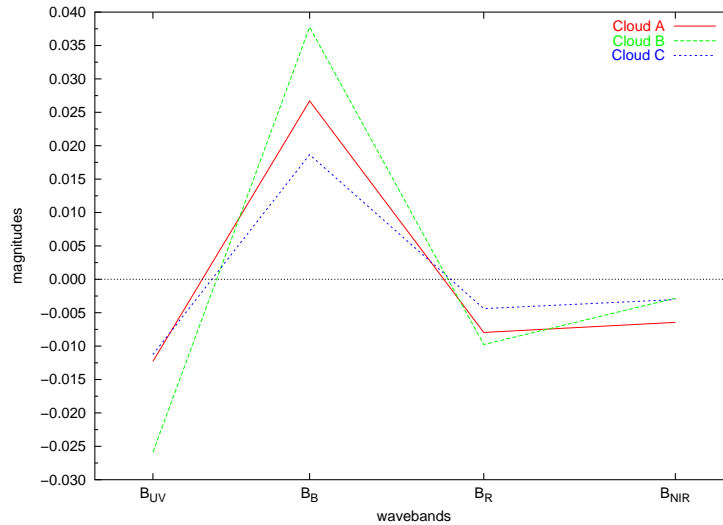


Figure 6.3: This graph shows the deviation of the intensity in the BUSCA bands for the three example clouds A,B,C. The intensities are normalised to the assumed grey colour of each cloud. Higher magnitudes indicate larger extinction.

Different colours of clouds are depend on the size of water drops in the clouds. Following the explanation of (Minnaert 1993, Ch. 10) water drops of different size can change the scattered light and also work like small prisms in the case they form rainbows. He claims that water drops with a diameter between one and two millimetres form a bow with violet, red, and green parts and barely with blue. If the diameter drops to 0.5 mm also the red in the bow is becoming weaker.

If his explanations apply to the results of the cloud analysis with BUSCA, cloud B with the strong extinction in the blue band consists possibly of large water drops. Then the diameter of the drops in cloud C should be smaller. A possible explanation for the behaviour of cloud A can be that it consists of a mixture of larger and smaller water drops. Since the nature of the clouds could not be studied by eye it is not possible to say something about the type of the clouds or if there were perhaps two clouds lying above each other.

The last point which has to be discussed in this section is the error of this special analysis and the significance of the results for the photometry. The photometric errors of the reference stars used for the light curve in Fig. 6.2 are very small, <0.001 mag for cloud A and C and 0.002 mag for cloud B. The deviation from the assumed grey colour is significantly higher than the photometric errors while systematic errors are negligible, so the effect seen is not an artificial one.

6.2 Summary and conclusions

The photometric analysis of the clouds with BUSCA shows that clouds are not really grey as predicted in Sect. 5.5. During large cloud extinction (~ 2 to 3 mag) the maximum deviation from the assumed grey colour is up to 0.4 mag. All analysed clouds have a blue extinction which makes the BUSCA $B_B - R_B$ colour index redder and the $UV_B - B_B$ bluer.

A conclusive explanation for this behaviour cannot be given. Also there is no proof that, in general, all

clouds have a non-grey colour, but this effect should be further studied in future. However, for typical observations under photometric conditions or with small thin clouds this effect plays a negligible role.

7 BUSCA Application I: The rapid variable sdB star PG1605+072

Falter S., Heber U., Dreizler S., Schuh S.L., Cordes O., Edelmann H., 2003, A&A 401, 289

7.1 sdB stars

Subluminous B (sdB) stars dominate the population of faint blue stars of our Galaxy and are found in the disk (field sdBs), in globular clusters (Moehler et al. 1997), and in the halo of our Galaxy (Altmann et al. 2004). These stars play an important role in the “UV upturn phenomenon” observed in elliptical galaxies and galaxy bulges (Greggio & Renzini 1990, 1999). According to observations with the Ultraviolet Imaging Telescope (Brown et al. 1997) and the Hubble Space Telescope (Brown et al. 2000) sdB stars are sufficiently numerous to be responsible for the excess UV flux.

It is generally accepted that sdB stars belonging to the extended Horizontal Branch (EHB) burning He in their cores (Heber 1986; Saffer et al. 1994). The hydrogen envelope surrounding the core of about half a solar mass is very thin ($< 2\%$ by mass) and therefore inert. These EHB stars will continue their evolution directly towards the white dwarf graveyard, avoiding the AGB and planetary nebular phases (Dorman et al. 1993).

How sdB stars evolve towards the EHB with effective temperatures up to 40 000 K remains a puzzle. The star must have lost all but a tiny fraction of the hydrogen envelope and the He core has attained the minimum mass ($\approx 0.5M_{\odot}$) required for the He flash. This challenges every mass loss mechanism in aspects of timing and effectivity. Recent findings (Maxted et al. 2001; Saffer et al. 2001; Heber et al. 2002) emphasise the significance of close binary evolution.

7.2 The V361 Hya class of stars

Some of the sdB stars were recently found to exhibit rapid multi-periodic light variations ($P \approx 80 - 600$ s) of low amplitudes (a few mmag). They form a new class of pulsating stars named V361 Hya stars¹. Since then more than 30 sdB pulsators are known (Charpinet 2001; Piccioni et al. 2000; Silvotti et al. 2000). Observed brightness variations are caused by radial and non-radial, low degree and low order acoustic pulsation modes. The driver for the pulsation is an opacity bump due to Fe and other metals (Charpinet et al. 1997) at a temperature of $\approx 2 \times 10^5$ K in the sdB envelope.

Stellar pulsations allow insight into the structure of the stellar atmosphere and therefore indirectly into the evolutionary history. The frequencies or periods of the pulsation modes probe the chemical stratification and the mass distribution which otherwise is impossible to determine. The power of asteroseismological tools has been demonstrated in the field of pulsating white dwarfs for which stellar parameters like mass, luminosity or thickness of the envelope were derived (e.g. Winget et al.

¹The former name of this class was EC 14026 named after the prototype of this type of pulsating sdB stars (Kilkenny et al. 1997)

1991). In the case of variable sdB stars these parameters will constrain the evolutionary history and consequently shed more light on the origin of these stars.

Identification of pulsation modes (characterised by spherical harmonics with the indices l and m) is a prerequisite for asteroseismology. Brassard et al. (2001) have successfully carried out an asteroseismological analysis for the sdB star PG0014+067. For the first time they were able to determine the stellar mass ($M_*/M_\odot = 0.490 \pm 0.019$) as well as the envelope mass ($\log(M_{\text{env}}/M_\odot) = -4.31 \pm 0.22$) and both are in excellent agreement with predictions from evolutionary models (Dorman et al. 1993).

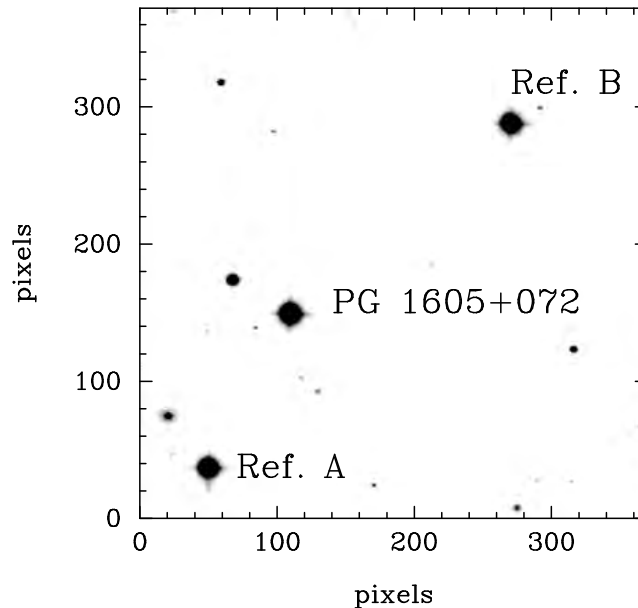


Figure 7.1: The field of the target star PG1605+072 is shown, and the two comparison stars “Ref. A” and “Ref. B” used for the relative photometry are indicated.

7.3 PG1605+072

Pulsations produce not only photometric variations but also line profile variations that offer an alternative approach towards mode identification. PG1605+072 is the ideal target for a photometric and spectroscopic analysis, because it has the longest pulsation periods (≈ 500 s) known for this class of variable stars so that spectra with reasonable S/N can be obtained covering all aspects of each pulsation period. Moreover, this star has the largest variations of all known sdBVs (0.2 mag in the optical) and by far the richest frequency oscillation spectrum (> 50 modes, Kilkenny et al. 1999). A recent spectroscopy study revealed this star to be a rather rapid rotator ($v \sin i = 39 \text{ km s}^{-1}$, Heber et al. 1999) which may complicate the identification of modes due to non-linear effects on mode splitting.

For the photometric studies of PG1605+072 BUSCA was chosen which exploits the possibility to get colour information during each single measurement. The simultaneously observed data avoid the problem of deriving colour indices through interpolation in perhaps photometrically poor data sequences.

7.4 Data and data analysis

The photometric data were taken at the 2.2m telescope at Calar Alto observatory in 3 nights during a five night run between May 14 and 18, 2001. No data could be achieved at the other nights due to bad weather. For the observations a CCD window of 346×400 pixels (corresponding to $121'' \times 140''$) was chosen, which covers the target star and two comparison stars “Ref. A” and “Ref. B” (see Fig. 7.1). The advantage of the small window is the short readout time per exposure, so the full cycle time is only 51 seconds. The total of 880 measurements resulted in an observed coverage of nearly 12.5 hours of PG1605+072. Fig. 7.2 shows the light curve for each night. The gaps signify the periods of bad weather.

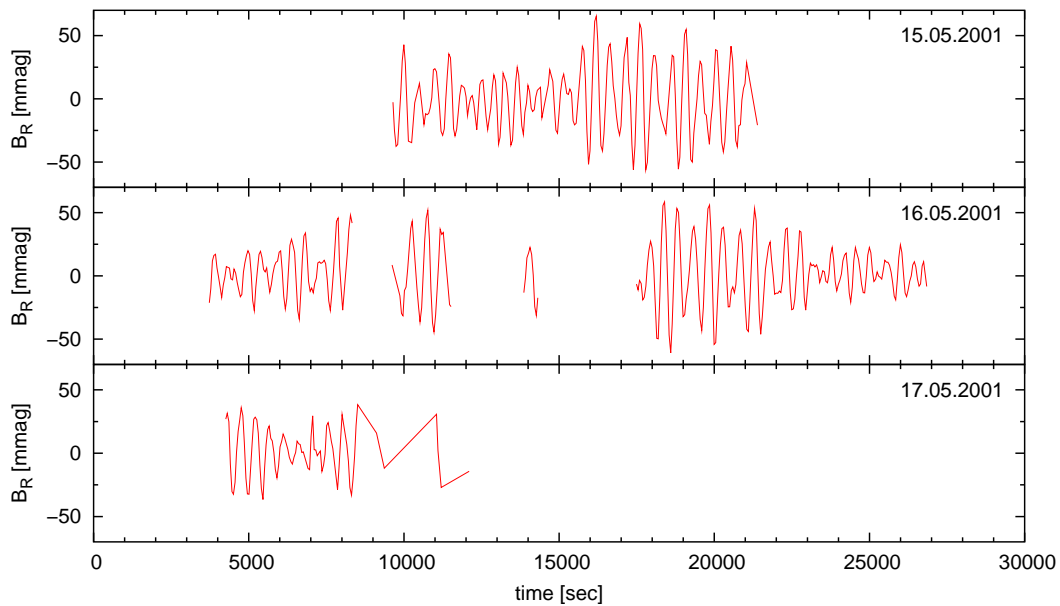


Figure 7.2: Light curve of PG1605+072 in the BUSCA band R_B for each night. The zero magnitude refers to the median magnitude of the star. The gaps signify the periods of bad weather in which no data were taken.

The basic data reduction was done as described in Chap. 4. For the star flux measurements the TRIPP (Time Resolved Imaging Photometry Package, see Schuh et al. 2000) software package running under IDL was used. TRIPP is based on the CCD photometry routines written by Geckeler (1998) and performs aperture photometry. The most important step is the determination of the relative flux of the target star with one or more stars as comparisons objects. The detection of variations of the order of a few mmag is only possible when comparison stars and sky background are recorded simultaneously (especially under comparatively poor conditions). TRIPP is also used for calculating periodograms, confidence levels and fits with multiple sine functions (see Dreizler et al. 2002, for more details).

Fig. 7.3 shows the Lomb-Scargle periodograms of all BUSCA bands. This data set spans a period of three nights. The gaps of daytime or due to bad weather cause the effect of aliasing² which is clearly visible with small peaks to the left and right of the main peak frequency. To take this into account the frequency resolution is determined to $\Delta\nu = 5.68 \mu\text{Hz}$. A prewhitening procedure was applied in order to remove all insignificant peaks from the periodogram. From the “clean” diagram

²For full description of this sampling effect in the fourier space see Bracewell (1965).

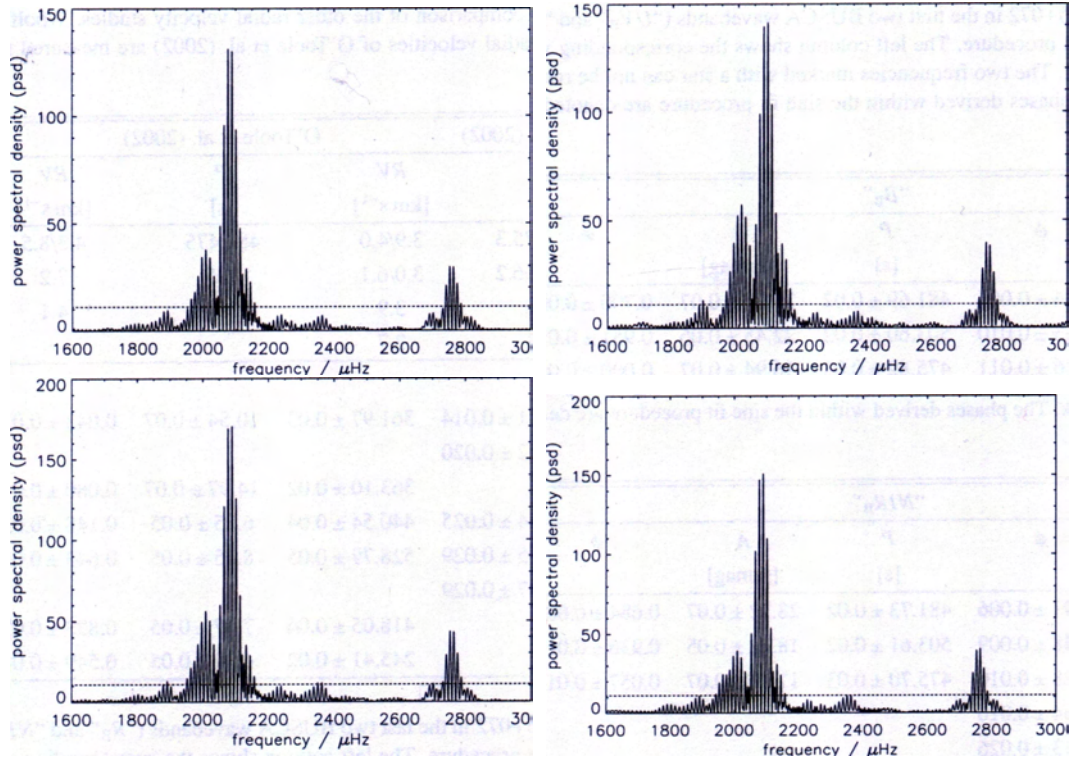


Figure 7.3: Lomb-Scargle periodograms of the light curves of PG1605+072 in the BUSCA bands UV_B , B_B (top), R_B and NIR_B (bottom). The horizontal line in each panel represents the confidence level of 99% (3σ -level).

the amplitudes for each frequency are obtained. The horizontal line in the diagrams indicates the 3σ confidence level above which we assume the detected frequencies to be real. All peaks with the same frequency can be identified in all BUSCA bands (see Tab. 7.1). The errors for the frequencies and amplitudes given are formal fit errors from the sine fit procedure. The accuracy of the amplitudes can be determined by calculating the median value of the white noise in the frequency range 3–5 mHz where almost no frequencies are seen. The values for the accuracy for the BUSCA wavebands are 1.52 mmag for UV_B , 1.53 mmag for B_B , 1.12 mmag for R_B and 1.37 mmag for NIR_B , respectively. In all four wavebands five peaks with the same frequency can be identified. The dominant frequency is found at 2.076 mHz. Additional frequencies are located in the region around 2.74–2.78 mHz, but these peaks are closely spaced so that a corresponding identification in all BUSCA bands due to the medium frequency resolution was not possible.

Fig. 7.4 shows the semi-amplitudes for four selected frequencies as a function of the effective wavelength of the bands. In Fig. 7.5 the relative change of the semi-amplitudes of each waveband is displayed. The deviation with respect to the mean is largest for the UV_B band. The other channels, considered separately, behave rather similar showing much smaller deviations from the mean brightness. This can be explained through the fact that the UV_B band lies blueward the Balmer jump and the other redward of it. The opacity changes a lot across this wavelength range and thus the stellar flux originates from different atmospheric depths.

The data also indicates that there is no correlation between the wavebands and the phases derived from the sine fit procedure.

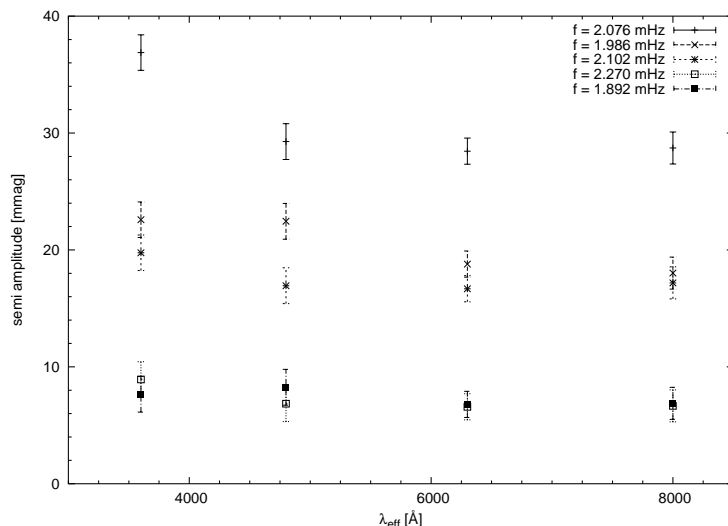


Figure 7.4: Semi-amplitudes of four selected pulsation frequencies of PG1605+072 as a function of effective wavelength.

7.5 Summary and conclusions

The photometric multi-site long term campaign (14 days in April/May 1997) of Kilkenney et al. (1999) discovered more than 50 frequencies in their analysis of PG1605+072. The five frequencies (2.076, 1.9865, 2.102, 2.2695 and 1.8912 mHz) detected in all BUSCA wavebands were also present in their data. Some of the other can be identified with the Kilkenney data (e.g. 4.0631 mHz) and other cannot (in particular at 2.7866 mHz). A closer inspection of these frequencies shows that all of them are very close to one-day aliases ($\pm 11.57 \mu\text{Hz}$) of the extracted frequencies of the BUSCA data or Kilkenney's data to within the frequency resolution of $5.68 \mu\text{Hz}$ (Kilkenney, $1.2 \mu\text{Hz}$). Small deviations in this measurements can also be explained by the shorter time spanned by the BUSCA data (≈ 48 hours compared to ≈ 218 hour). In contrast to the analysis presented here, Kilkenney et al. (1999) were able to resolve closely spaced frequencies, e.g., at 2.1017 mHz and 2.1033 mHz (see Tab. 7.1).

Parallel to the photometric study of PG1605+072 with BUSCA spectroscopy with the TWIN spectrograph at the 3.5m telescope at Calar Alto observatory was achieved. From this data radial velocity curves for the Balmer lines H_β and H_γ with a resolution of $51 \mu\text{Hz}$ were extracted. Analysis of this data shows 3 frequencies at 2.078, 2.756 and 1.985 mHz which are consistent to the BUSCA data. The time base of this investigation is too short to resolve other frequencies. Additional spectroscopic data analysis in 1999 and 2000 (O'Toole et al. 2000, 2002; Woolf et al. 2002) show the same frequency distribution but also a change in the amplitudes and, in particular, that no power was detected at 2.076 mHz in 1999. The power at 2.076 mHz appeared again in 2000 but it was at that time weaker than before. This means that the power switches within a few years. The spectroscopic data from May 2001 show that the power distribution switched back to that of 1997 measured by Kilkenney et al. (1999).

The main conclusion from this investigation (see Falter et al. 2003) is that BUSCA can be used to observe pulsating sdB stars with periods of a few minutes. The frequencies measured in the BUSCA light curves are consistent with those of Kilkenney et al. (1999) although the time basis of all observations is much too short to resolve the full frequency spectrum of this star. More than 50 frequencies have

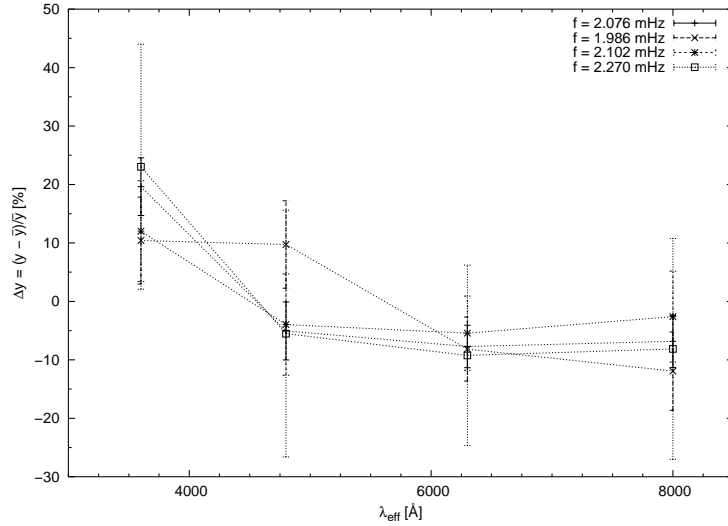


Figure 7.5: Relative semi-amplitudes of the four selected frequencies from Fig. 7.4 of PG1605+072. These are calculated by $\Delta y = (y - \bar{y}/\bar{y})$. y is the semi amplitude of the wavebands.

been resolved in their long photometric study. Consequently, a new data set with a longer time basis is needed. For that reason a combined photometric and spectroscopic multi-site campaign termed the MSST (Multi Site Spectroscopic Telescope) project (Heber et al. 2003) was organised which also includes BUSCA. The observations planned covered a period of one month in May/June 2002 and were successfully accomplished. The obtained data are now in the process of reduction and analysis.

Table 7.1: Frequencies and corresponding periods as well as semi-amplitudes derived for PG1605+072 in all BUSCA bands. The errors of the periods and amplitudes are formal fit errors from the sine fit procedure. In comparison to the values derived in Kilkenny et al. (1999) the two with stars marked frequencies cannot be resolved in the BUSCA data.

Kilkenny 1999			UVB			B _B			R _B			NIR _B			
<i>f</i>	<i>P</i>	<i>A</i>	<i>f</i>	<i>P</i>	<i>A</i>	<i>f</i>	<i>P</i>	<i>A</i>	<i>f</i>	<i>P</i>	<i>A</i>	<i>f</i>	<i>P</i>	<i>A</i>	<i>θ</i>
[mHz]	[s]	[mmag]	[mHz]	[s]	[mmag]	[mHz]	[s]	[mmag]	[mHz]	[s]	[mmag]	[mHz]	[s]	[mmag]	
2.0758	481.75	27.4	2.0760	481.69±0.02	36.88±0.12	0.684±0.006	481.69±0.02	29.27±0.07	0.700±0.008	481.71±0.01	28.45±0.05	0.691±0.006	481.73±0.02	28.72±0.07	0.684±0.007
1.9853	503.70	3.3	1.9861	503.51±0.03	22.59±0.09	0.953±0.010	503.60±0.02	22.45±0.06	0.951±0.010	503.58±0.01	18.79±0.04	0.948±0.009	503.61±0.02	18.02±0.05	0.936±0.011
*2.1017	475.82	15.4	2.1020	475.74±0.04	19.76±0.11	0.026±0.011	475.82±0.03	16.94±0.03	0.000±0.013	475.76±0.02	16.68±0.05	0.028±0.010	475.70±0.03	17.18±0.07	0.057±0.012
*2.1033	475.45	15.9													
2.7613	362.15	1.8	2.7631	361.92±0.03	16.01±0.16	0.051±0.014	361.97±0.03	10.54±0.07	0.043±0.021						
-	-	-	2.7530							363.23±0.01	17.15±0.04	0.054±0.010			
2.7663	361.49	2.0	2.7668	361.43±0.06	10.94±0.15	0.192±0.020				358.87±0.03	6.22±0.04	0.213±0.026			
-	-	-	2.7554				363.10±0.02	14.97±0.07	0.080±0.015						
2.7427	364.60	15.1	2.7427												
-	-	-	2.7637										364.60±0.02	10.37±0.06	0.043±0.019
2.2701	440.51	5.2	2.2700	440.52±0.05	8.92±0.08	0.144±0.025	440.54±0.04	6.85±0.05	0.148±0.032	440.56±0.03	6.58±0.04	0.133±0.024	440.60±0.04	6.66±0.05	0.183±0.030
1.8914	528.70	13.9	1.8915	528.69±0.06	7.65±0.09	0.675±0.029	528.79±0.05	8.25±0.05	0.643±0.027	528.71±0.04	6.79±0.04	0.670±0.024	528.90±0.06	6.88±0.05	0.625±0.029
2.7173	368.01	0.6	2.7191	367.77±0.06	7.45±0.10	0.897±0.029									
2.3920	418.05	2.2	2.3921				418.05±0.04	7.87±0.05	0.833±0.028	418.06±0.03	5.80±0.04	0.811±0.028	417.94±0.04	6.44±0.03	0.821±0.031
-	-	-	4.0748				245.41±0.02	4.39±0.05	0.549±0.049						
4.0618	246.19	1.2	4.0624				246.16±0.01	4.47±0.04	0.458±0.036	246.17±0.02	5.38±0.05	0.413±0.037			

8 BUSCA Application II: Strömgren photometry of Globular Clusters

8.1 Introduction

One of the most frequently discussed topics during the construction and test phases of BUSCA was the question of what are suitable targets to be observed with BUSCA. One answer was the observation of many globular cluster (GC) stars to get accurate photometrical metallicity determinations.

In several publications (e.g. Richtler (1989); Grebel & Richtler (1992); Richter et al. (1999)) it was shown that Strömgren photometry allows to get a reliable metallicity indicator. The position of late type (G and K) stars in the Strömgren $(b-y)$ vs. m_1 diagram is correlated to their metallicity. Since the Strömgren v filter includes several iron absorption lines, this filter as well the $m_1 = (v-b) - (b-y)$ index are sensitive to the iron abundance. In contrast the $(b-y)$ colour index does not depend on metal lines. Within a certain colour range of $0.5 < (b-y) < 1.1$ mag, giant and supergiant stars with a constant iron abundance lie on an approximately straight line. For giants redder than $(b-y) = 1.1$ mag TiO and MgH absorption in the y band breaks down this calibration. Since the “old” metallicity calibrations are based only on metal-rich stars, they failed to reproduce the slope of constant metallicity lines in the $(b-y), m_1$ diagram for metal poor GCs. Hilker (2000) revised the metallicity calibration by adding metal poor stars to the Grebel & Richtler (1992) sample.

For the photometric metallicity investigation a sample of GCs of the northern hemisphere was observed with BUSCA. First results of the GCs M 10, M 72, and NGC 6394 were presented by Wittlich (2002). The values they derived for these clusters fit well to the literature values. With this first work BUSCA was also shown to be suitable for GC observations.

For the metallicity studies in this work two GCs, M 12 and M 71 were selected. Both clusters are well studied but up to now no Strömgren metallicity studies were available. Moreover, M 71 shows additionally CN variations among the red giant branch (RGB) and main sequence (MS) stars. These variations were detected spectroscopically for only few RGB and MS stars. With this available data set more stars of the RGB can be investigated photometrically, which can give new hints of the origin of the CN variations.

Table 8.1: Coordinates and positional properties of the two globular clusters M 12 and M 71 taken from Harris (1996).

Name	α_{2000}	δ_{2000}	l	b	R_{sun} kpc
M12 NGC 6218	16 47 14.5	-01 56 52	15.72	+26.31	4.9
M71 NGC 6838	19 53 46.1	+18 46 42	56.74	-04.56	3.9

Tab. 8.1 gives the coordinates and positional parameters of the two globular clusters. M 12 is located above the Galactic plane and is an old and metal poor Galactic globular cluster. The cluster shows several structural similarities with the GC M 10, e.g., age, metallicity, distribution of stars. Moreover,

since both clusters have the same distance of ~ 5 kpc and their angular separation does not exceed 3° , they are proposed as a couple of interacting GCs (Buonanno et al. 1976). The position of M 71 is in the Galactic plane, so the images of the cluster are contaminated by field stars. However, there are proper motion studies by Cudworth (1985) and Geffert & Maintz (2000) who separate cluster members from the field stars. It is then possible to do the metallicity and CN analysis on cluster members without the influence of the field stars. In Tab. 8.2 the BUSCA observations of M 12 and M 71 were listed.

Table 8.2: Observational properties of the data set.

Name	Date	Exptime [s]	comment
M12 NGC 6218	2000/09/05	120,900	field 1
	2000/09/07	120,900	field 2
M71 NGC 6838	2000/09/04	120,900	field 1
	2000/09/06	120,900	field 2

8.2 CN variations in Galactic globular clusters

Following standard formation scenarios all stars in a GC have formed at the same time from a single gas cloud. Consequently, they have the same age and the same initial chemical composition. From investigations it is known that the iron abundance spread among cluster members is smaller than typical spectroscopic or photometric measurement errors (e.g. as reviewed by Suntzeff (1993) or Gratton et al. (2001)). Detailed studies have revealed significant star-to-star abundance variations of certain light elements including sodium, aluminium, carbon, nitrogen and oxygen in GCs (e.g. as reviewed by Kraft (1994)). One of the first discoveries of chemical inhomogeneities in GCs was made by Osborn (1971). He found two red giant stars in M 10 and M 5 to have enhanced CN molecular absorption strengths compared to other stars in these clusters. In further studies stars from the tip of the red giant branch (RGB) down to the subgiant branch (SGB) were investigated (e.g., Bell et al. 1983, 1984; Hesser et al. 1984; Smith et al. 1989; Suntzeff & Smith 1991; Briley et al. 1992; Cohen et al. 2002)). With the capability of larger telescopes and improved instruments also stars down to the main sequence (MS) of a few nearby GCs have been spectroscopically observed (Hesser 1978; Briley et al. 1991; Suntzeff & Smith 1991; Cannon et al. 1998; Cohen 1999a,b; Briley & Cohen 2001; Gratton et al. 2001; Harbeck et al. 2003).

The CN abundance is usually defined through two (spectro-)photometric indices. The definition of the indices is as follows:

$$S(3839) = -2.5 \log_{10} \frac{I(3846, 3883)}{I(3883, 3916)}$$

$$S(4142) = -2.5 \log_{10} \frac{I(4120, 4216)}{I(4216, 4290)}$$

For the photometry the presence of CN molecules influences the Strömgren photometry. The CN band at 4215 \AA is located at the right edge of the v band. Therefore strong CN absorptions decrease the flux in the v band significantly. The absorption also changes the $(b - y), m_1$ diagram of a GC with star-to-star CN variations. The loci of CN strong stars is above the line of constant iron abundance (Hilker 2000). The CN band at 3883 \AA is not covered by the v filter.

The origin of the abundance inhomogeneities, especially in the CN molecule, among GC stars is still unresolved. Three scenarios are discussed in the literature: (i) abundance changes in GC stars due to the evolution of the GC stars, (ii) GC self-pollution and (iii) primordial inhomogeneities. An excellent review on these scenarios was written by Cannon et al. (1998) and is summarised here.

Stellar evolution

If all stars in a globular cluster have started with the same initial chemical composition, the surface abundances of the CN molecule must have changed in the stars during their subsequent evolution. In the stellar evolution scenario the CNO-cycle processed material from the interior of hydrogen-burning stars is dredged up (e.g., by rotational mixing) to the stellar surface. The efficiency of this dredge up is reflected by changes in the surface chemical composition. This scenario can explain why chemical inhomogeneities are generally found in the CNO elements, but not in the iron-peak elements. Although according to conventional stellar evolution models the dredge up of processed material only happens on the RGB, CN variations are evident along the RGB, SGB and at the MSTO of a number of GCs such as 47 Tuc, M 71, M 5 and, M 22. In many clusters the CN band strengths at a given stellar luminosity show a bimodal distribution (e.g., Norris 1987; Smith 1987) which cannot be accounted for by the stellar evolution scenario. The origin of this bimodality is not yet understood. Instead of the bimodality this scenario implies a more uniform distribution of the CN abundances.

Self-pollution

Asymptotic giant branch (AGB) stars with masses of $\sim 5M_{\odot}$ eject stellar winds that contain considerable amounts of CNO processed material (e.g., Ventura et al. (2001)). Other types of stars such as planetary nebula progenitors or novae could also eject CNO enriched material. These stellar winds may be accreted by other stars, including the present MSTO, SGB and RGB stars. Such stars which have accreted this material would show surface compositions different from that of stars without any material accretion. If only the stellar surfaces were polluted, deep convective mixing during the evolution along the RGB should dilute the chemical inhomogeneities. This effect is not seen in the case of the nitrogen abundance, although the [C/Fe] abundance is found to decrease with luminosity on the RGB in some clusters such as M 92 and M 13 (Carbon et al. 1982; Suntzeff 1981). Also a bimodal abundance cannot be explained from this scenario; one might expect rather a range in the surface contamination.

Primordial variations

The assumption that all stars in a globular cluster have the same chemical composition from the very beginning may not necessarily be true. For instance, two molecular clouds of different chemical composition could have merged and formed a globular cluster. If the gas was not mixed, stars would reflect the chemical composition of one or the other cloud. Here, a bimodality distribution is explainable. Also the first supernovae during the star forming epoch of an GC may have polluted the parent molecular cloud. Many elements in stars that formed after these events would be enriched. These two primordial scenarios can explain abundance variations in the CNO elements, but they lack an easy explanation of the chemical homogeneity of the iron-peak elements. In a third primordial scenario two globular clusters merged after they have had completed their star formation. The result would be a bimodal abundance distribution, but again the homogeneity of the iron-peak elements is a problem.

8.3 Results for the individual clusters

8.3.1 M12 (NGC 6218)

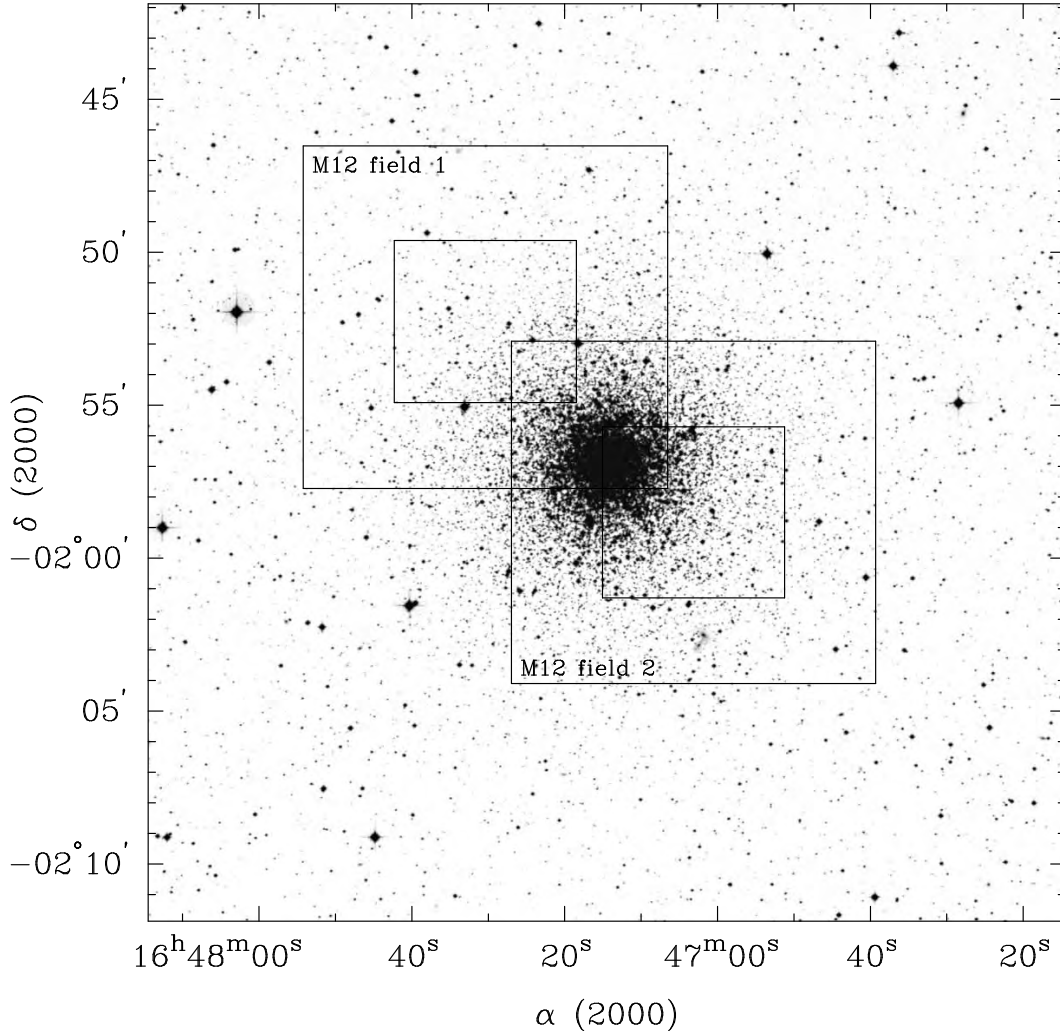


Figure 8.1: The two BUSCA pointings on M12 are shown overlain on a map from the DSS. The smaller inner rectangles indicate the small fields available in the UV channel.

8.3.1.1 Photometry

The observation of the globular cluster M12 was divided into two pointings, field 1 and field 2, to cover the whole M12 field. At the time of the observing only the small $2k \times 2k$ CCD was installed in the BUSCA ultraviolet channel. Fig.8.1 shows the coverage of M12 by the two BUSCA pointings.

The data were reduced (see Ch. 4) and the stars of the inner fields with v , b and y magnitudes were matched using the special pairing algorithm (see Sect. 4.2.2). Unfortunately, the inner region of field 1 has only a small overlap with the centre of M12, so there are only a few matched stars left. Consequently, field 1 was completely disregarded for the further investigation. The resulting photometric

catalogue of M 12 contains 1365 stars. This low number can be explained with the poor sensitivity of the CCD in the BUSCA ultraviolet channel in comparison to the other BUSCA CCDs. This catalogue was calibrated using the equations 4.2ff and the PSF-aperture shift was applied. The calibrational parameters for the 05. Sept. night were taken from Tab.4.1.

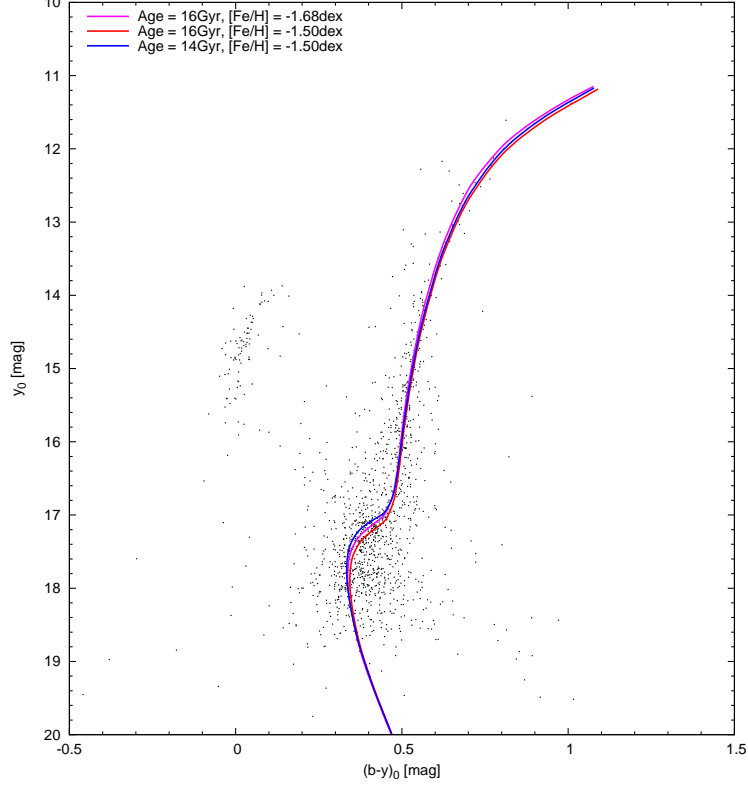


Figure 8.2: CMD of M 12 of all matched stars having v , b , and y magnitudes. Additionally three isochrones were shown which match the data. The best isochrone fit gives an age of 16 Gyr and a metallicity of $[\text{Fe}/\text{H}] = 1.59$ dex.

In Fig. 8.2 the calibrated “Colour Magnitude Diagram” (CMD) of M 12 with all matched stars with v , b and y magnitudes is given. M 12 has a blue horizontal branch and a well populated red giant branch down to the main sequence turn off (MSTO) point. The red part of the horizontal branch is not populated. The main sequence is hardly visible. Overlaying to the CMD Isochrones from Bergbusch & Vandenberg (1992) were fitted. The fit process itself is difficult due to the lack of a clearly visible main sequence. Matching the isochrones to the giant branch gives an easy metallicity determination. The value of the metallicity is between -1.68 and -1.50 dex. The age determination is more critical. Adopting the distance of M 12 from von Braun et al. (2002) (vB hereafter) of $d = 4.9$ kpc (from the distance modulus of $(m - M)_V = 13.46$ mag), the best fitting isochrone gives an age of 16 Gyr. In the CMD isochrones of 14 resp. 16 Gyr in age, and -1.68 resp. -1.50 dex in metallicity are shown. The isochrone with younger ages than 16 Gyr does not fit well the TOP region. The result from the BUSCA data is an age of 16 ± 1 Gyr and a metallicity of -1.59 ± 0.09 dex which is in good agreement to the values of vB and other studies [e.g. Hargis et al. (2004)].

In contrast to vB a constant extinction value was used for the BUSCA M 12 field. vB found a reddening zero point of $E(B - V) = 0.17$ mag and a differential extinction in a field of $25.9' \times 25.9'$ of

$\delta E(B - V) = 0.029 \pm 0.042$ mag and $\delta E(B - V) = 0.006 \pm 0.011$ mag for the inner region of M 12. Since the field of the BUSCA data is located close to the centre of M 12 the differential extinction can be neglected. The BUSCA data result in a reddening of $E(B - V) = 0.26 \pm 0.02$ mag which is higher than the vB value.

8.3.1.2 Metallicity

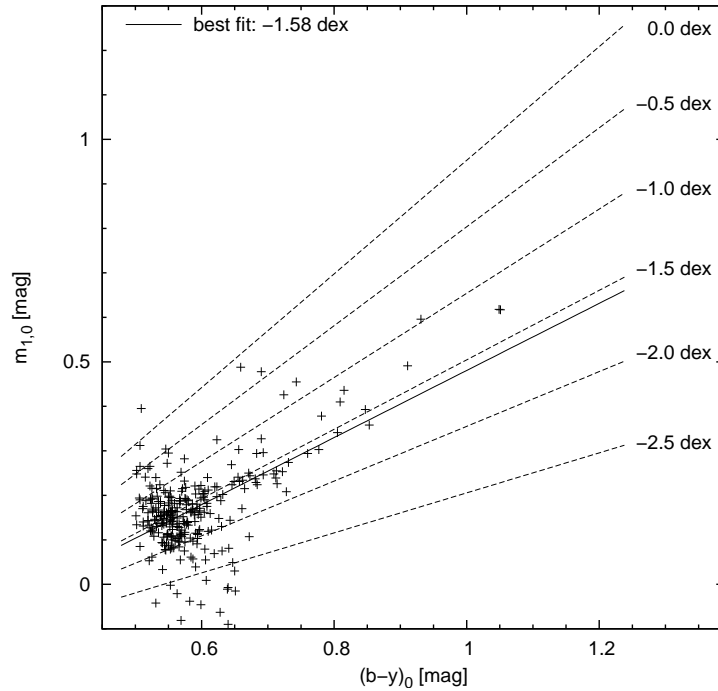


Figure 8.3: m_1 vs. $b - y$ diagram of the red giant branch stars of M 12. The dashed lines indicate isometallicity lines ranging from -2.0 up to 0.0 dex. The metallicity determined by the calibration of Hilker (2000) is $[\text{Fe}/\text{H}] = -1.58 \pm 0.05$ dex.

For the $m_1, b - y$ diagram only RGB stars in the colour range of $0.5 < (b - y) < 1.1$ mag were selected (see Fig. 8.3). The diagram shows there is a strong correlation between a the $(b - y)$ colour and the m_1 index. The bump on the left side is caused by the stars near the TOP region which fall in the specified $(b - y)$ colour range. In the diagram also isometallicity lines calculated from Hilker (2000) ranging from -2.5 to 0.0 dex were plotted. Using the metallicity calibration of Hilker (2000) yields to a metallicity of $[\text{Fe}/\text{H}] = -1.58 \pm 0.05$ dex which is in good agreement to the metallicity determined by the isochrone fit.

8.3.1.3 Summary for M 12

The main results from the isochrone fitting of the M 12 BUSCA data are an age of 16 ± 1 Gyr and a metallicity of $[\text{Fe}/\text{H}] = -1.59 \pm 0.09$ dex, similar to the values found in the literature (von Braun et al. 2002). Also the independent metallicity determination from the $(b - y), m_1$ diagram yields a consistent metallicity value of $[\text{Fe}/\text{H}] = -1.58 \pm 0.05$ dex. The latest studies of the cosmic background radiation data from the “Wilkinson Microwave Anisotropy Probe” *WMAP* have found the age of the universe

to be 13.7 ± 0.2 Gyr (Spergel et al. 2003). With this result there is now a tight upper limit for the possible ages of Galactic globular clusters. One solution of this problem are recent α -enhanced stellar models including He diffusion calculated by VandenBerg (2000). Using these isochrones leads to new lower ages of the globular clusters of 0.5 – 2 Gyr. Hargis et al. (2004) found with these new models 12-13 Gyr as an age for M 12 which is then consistent with the *WMAP* results. Unfortunately, these new isochrones are not yet available for the Strömgren filter system.

8.3.2 M71 (NGC 6838)

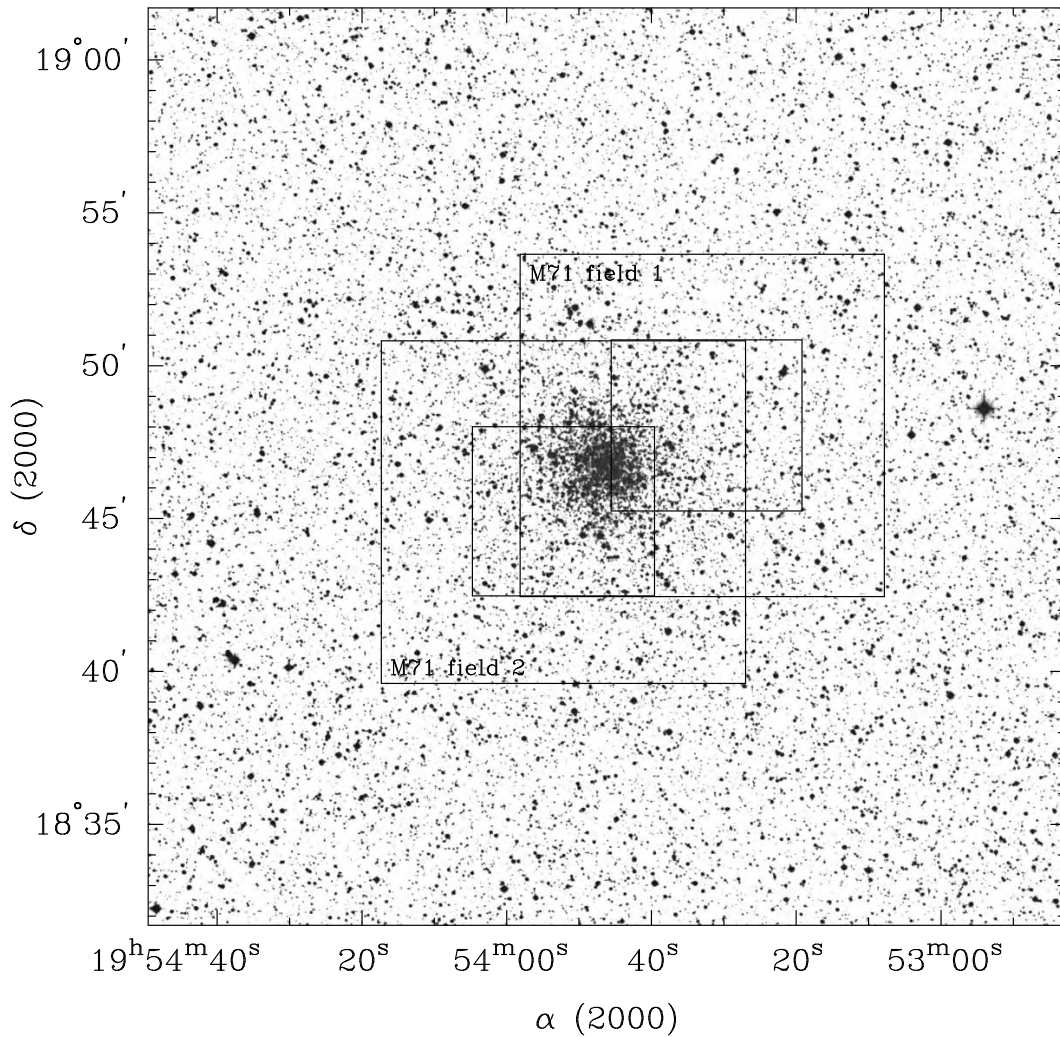


Figure 8.4: The two BUSCA pointings on M71 are shown overlain on a map from the DSS. The smaller inner rectangles indicate the small fields available in the UV channel.

8.3.2.1 Photometry

The globular cluster M71 was observed and reduced similar to M12. Frames of two pointings, field 1 and field 2 (see Fig. 8.4) were taken. Again only the small $2k \times 2k$ CCD was installed in the BUSCA ultraviolet channel. The resulting catalogue of both fields of M71 contain 4197 stars with v , b , and y photometry. This catalogue was absolute calibrated and reddening corrected using the extinction value of $E(B - V) = 0.28$ from Grundahl et al. (2002). Fig. 8.5 shows the CMD of the M71 BUSCA data. The limiting magnitude of the photometry is with $y = 20$ mag larger in comparison to the M12 data due to better seeing conditions. Due to the position of M71 in the galactic plane the CMD is contaminated by field stars. These are mostly located above the TOP. A red horizontal branch as well as the sharply defined red giant bump (as reported for the first time by Geffert & Maintz

(2000)) is clearly visible. Unfortunately for the metallicity studies the red giant branch is only sparsely populated.

Fitting isochrones of Bergbusch & Vandenberg (1992) to the data gives an age of 12 Gyr and a metallicity of -0.98 dex for the best fit. From the fit also a distance modulus of $y = 13.50 \pm 0.10$ mag was derived. The distance modulus as well as the age and metallicity are consistent with the Strömgen photometry by Grundahl et al. (2002).

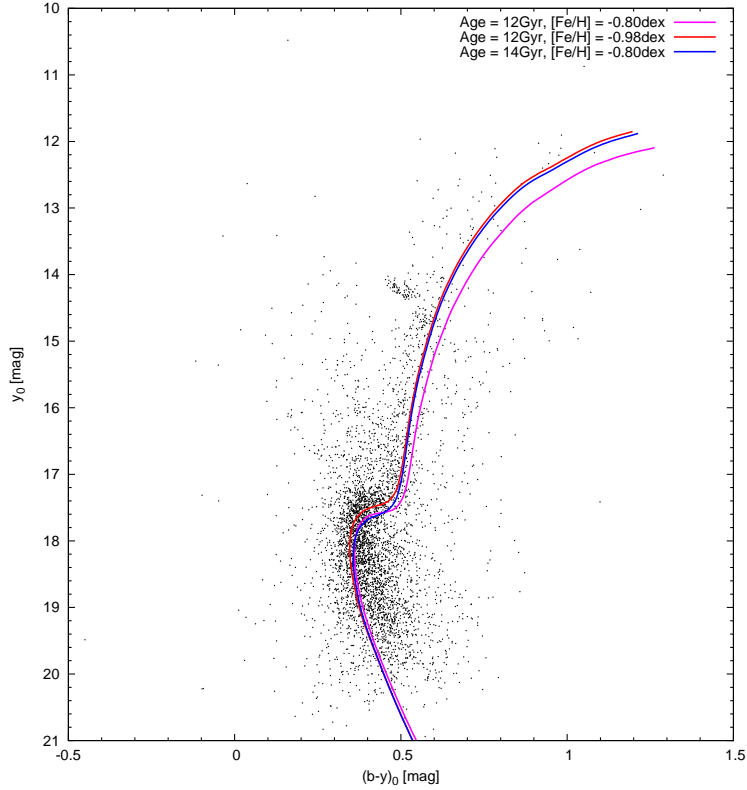


Figure 8.5: CMD of M 71 of all matched stars having v , b , and y magnitudes. Overlaid are three isochrones, two with an age of 12 Gyr and a metallicity of $[\text{Fe}/\text{H}] = -0.80$ and -0.98 dex which fit well the MS and the TOP region, and an isochrone with a larger age of 14 Gyr.

For the metallicity calibration all RGB stars in the colour range $0.5 < (b - y) < 1.1$ mag were selected. The $(b - y), m_1$ diagram (Fig. 8.6) shows large scatter and not as clear a correlation as in the M 12 data, caused again by the contamination of field stars. So a metallicity determination using the calibration of Hilker (2000) is not possible.

8.3.2.2 Membership analysis

One goal of the investigation of M 71 was to perform the metallicity calibration only on cluster members. Since M 71 is located at low galactic latitude ($b = -5^\circ$) many disturbing field stars are expected, which have to be eliminated before an accurate metallicity calibration is possible.

For the identification of the cluster members the work of Geffert & Maintz (2000) was used. They used CCD images (taken in 1993 and 1995) in combination with photographic plates (from 1967) for a proper motion analysis of the stars in a field of $20' \times 20'$ around the centre of M 71. In this study 320

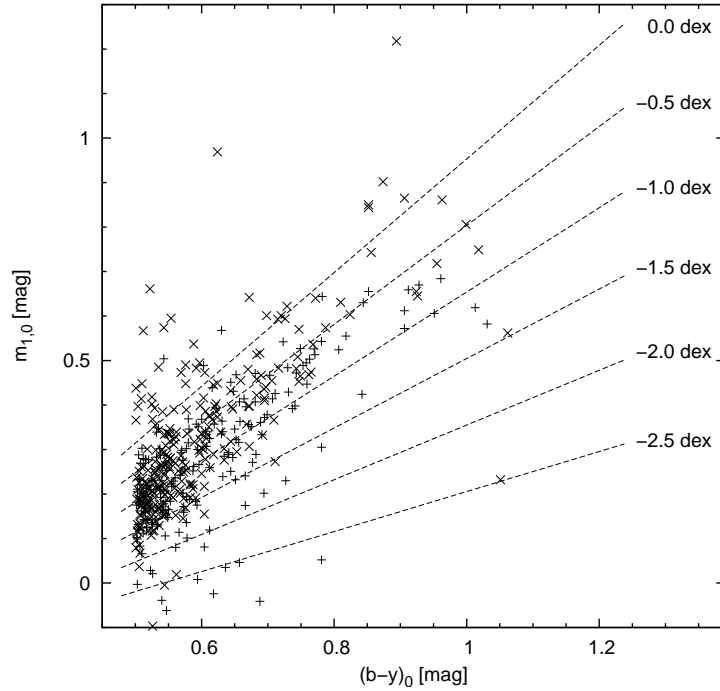


Figure 8.6: m_1 vs. $b - y$ diagram of the red giant branch stars of M 71. the dashed lines isometallicity lines ranging from -2.0 up to 0.0 dex. The relatively large scatter in this plot is caused by contaminating field stars, so a metallicity determination is not possible.

probable cluster members (membership probability $> 60\%$) up to a limiting magnitude of $V = 18$ were identified.

In a first step to look for cluster members in the BUSCA data 6 stars in this sample were identified in the overall astrometric calibrated sample of Geffert & Maintz (2000). These stars were used to establish a linear transformation of the x, y -CCD-coordinates into absolute sky coordinates. With this transformation 128 member stars of the Geffert & Maintz (2000) sample were identified in the BUSCA sample. Stars are regarded as identified when they lie within in circle with of $0.5''$ radius of the calculated position. Thus a double or misidentification was unlikely.

Fig. 8.7 shows the CMD of the identified members. Most of them belong to the red giant branch, so a determination of the age and metallicity of M 71 by fitting of isochrones is not appropriate. However, the best fitting isochrone of 12 Gyr and a metallicity of $[\text{Fe}/\text{H}] = -0.98$ dex (see Sect. 8.3.2.1) fits well to the data. The metallicity calibration for the cluster members works fine. The plot of the globular cluster members in Fig. 8.8 shows stars with a $b - y$ colour larger 0.65 mag in almost perfect alignment in comparison to the complete sample shown in Fig. 8.6. The fitted metallicity for the cluster members is $[\text{Fe}/\text{H}] = -0.76 \pm 0.06$ dex in good agreement with the literature.

8.3.2.3 CN variations

As seen in Fig. 8.8 the isometallicity fit of $[\text{Fe}/\text{H}] = -0.76 \pm 0.06$ dex has some scatter. One explanation of this scatter is small local reddening variation over the cluster field. Stars with a higher $E(B - V)$ would have a lower m_1 and would appear to be redder. In the metallicity diagram these

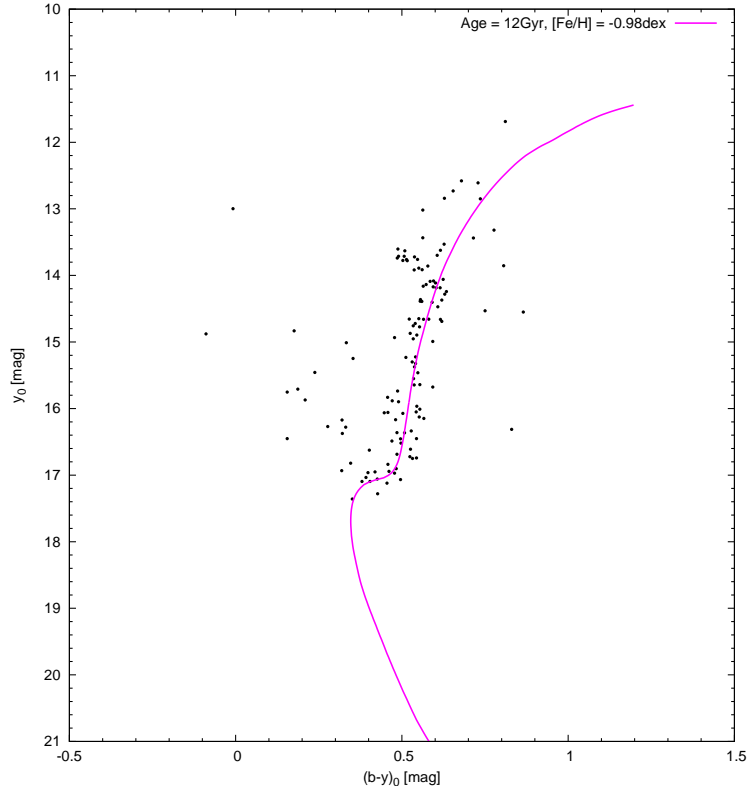


Figure 8.7: CMD of the identified cluster members of M 71 together with an isochrone of 12 Gyr and a metallicity of $[Fe/H] = -0.98$ dex from Bergbusch & Vandenberg (1992).

stars seem to be metal poorer. The second possible explanation of the scatter can be CN variations among the stars. This is not unlikely since this variation is confirmed spectroscopically for some red giant branch stars by Penny et al. (1992). For their analysis they choose red giant branch stars with a relatively high probability ($> 80\%$) of membership in M 71 as determined by Cudworth (1985) from his proper motion study. Additionally Briley & Cohen (2001) found also CN variations among main sequence stars.

Table 8.3: Member stars of M71 used for photometric calibration of the CN line indices $S(3839)$ and $S(4142)$. The spectroscopic data were taken from Penny et al. (1992).

Name	y	$b - y$	m_1	$S(3839)$	$\delta S(3839)$	$S(4142)$	$\delta S(4142)$
KC-302	14.992	0.563	0.159	0.335	0.027	0.040	0.014
KC-141	14.590	0.590	0.155	0.300	-0.022	0.040	0.009
KC-215	14.656	0.492	0.119	0.325	0.001	0.019	-0.013
I-111	14.243	0.604	0.248	0.621	0.277	0.170	0.132
I-109	14.187	0.573	0.219	0.552	0.207	0.101	0.062
I-75	14.185	0.585	0.238	0.781	0.435	0.203	0.164
KC-136	14.128	0.589	0.273	0.825	0.476	0.215	0.175
I-59	13.925	0.613	0.262	0.424	0.067	0.071	0.028

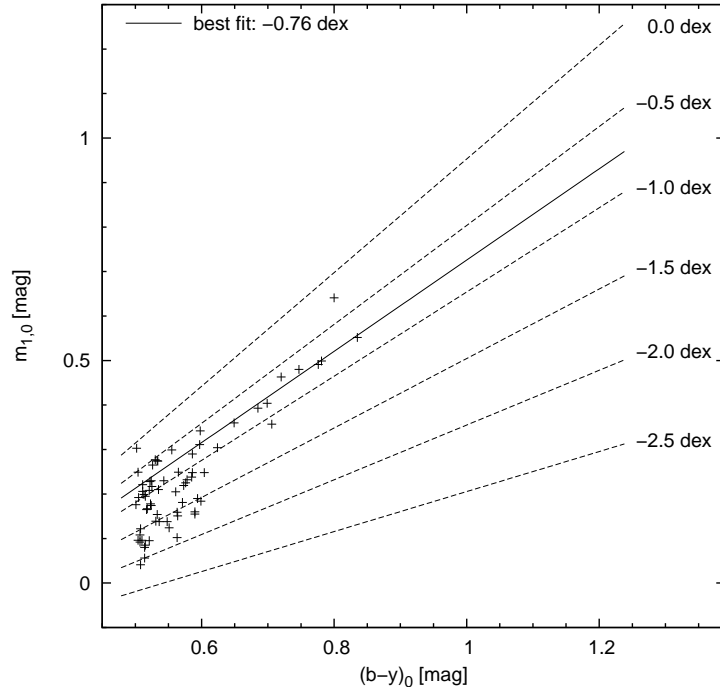


Figure 8.8: m_1 vs. $b - y$ diagram of the identified cluster members of M 71. The dashed lines indicate isometallicity lines ranging from -2.0 up to 0.0 dex. Using the calibration of Hilker (2000) a metallicity of $[\text{Fe}/\text{H}] = -0.76 \pm 0.06$ dex can be determined.

For the further analysis of the CN variations eight stars of the Penny et al. (1992) sample could be identified in the BUSCA data. Tab. 8.3 shows the published spectral CN abundance indices S(3839), S(4142) and the respective y , $b - y$ and m_1 BUSCA magnitudes. The formation efficiency of the CN molecule depends on the temperature and therefore the indices depend on the colour of the stars. $\delta\text{S}(3839)$ and $\delta\text{S}(4142)$ are the temperature normalised CN abundances so that the values are approximately zero for CN poor stars. For each of the stars a theoretical m_1 index was calculated for the previous determined metallicity of M 71 of $[\text{Fe}/\text{H}] = -0.76 \pm 0.06$ dex. In Fig. 8.9 the difference Δm_1 between the measured and theoretical m_1 index is plotted against the CN abundance index S(3839) (left panel) and S(4142) (right panel). Both indices clearly correlate with Δm_1 index. Stronger CN abundances correspond to higher Δm_1 values. However, the Δm_1 value of a CN weak star is negative whereas for the CN strong stars the Δm_1 is approximately zero. This effect is discussed later.

Adopting these relations between the spectroscopic CN abundance indices and the BUSCA Δm_1 a photometric CN abundance was calculated for each star of the sample of cluster members. In the left panel of Fig. 8.10 the photometric S(3839) CN index is plotted against the Strömgren y magnitude. In this distribution there is a gap in the S(3839) value between 0.4 and 0.6, so stars of $\text{S}(3839) < 0.4$ are marked as CN-weak stars (open circles) and stars of $\text{S}(3839) > 0.6$ are marked as CN-strong (closed circles). The right panel of this diagram shows the same distribution for the S(4142) index. The gap is also visible, but gets smaller for higher brightnesses. Penny et al. (1992) found a similar gap for their M 71 member sample. They conclude that this gap signifies a bimodality of the CN abundances among the M 71 RGB stars. Least squares straight lines have been fitted to the data points of CN-weak stars in Fig.8.9. The height of each S(3839) and S(4142) value above or below these baselines will be denoted as $\delta\text{S}(3839)$ and $\delta\text{S}(4142)$ respectively. This assures that CN-weak star have

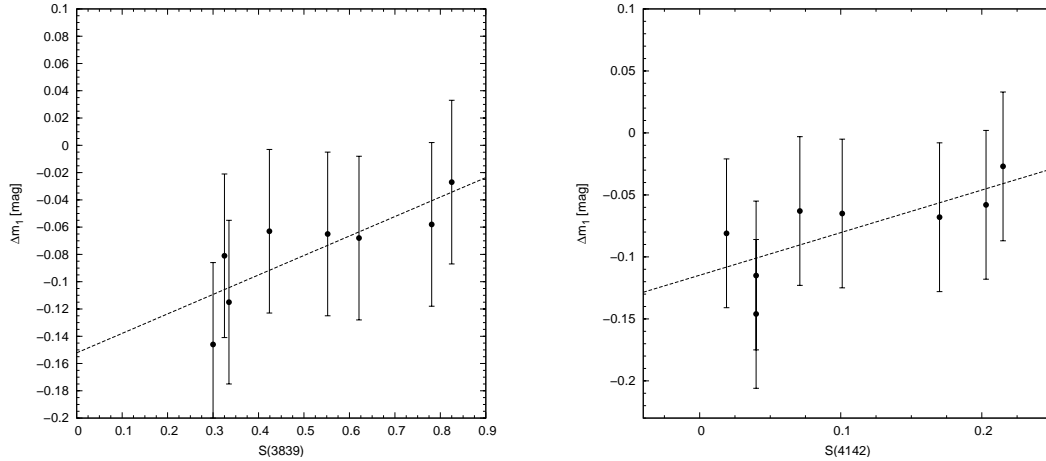


Figure 8.9: The normalised spectroscopic CN abundance index $S(3839)$ (left panel) and $S(4142)$ (right panel) vs. the difference of the measured and calculated Strömgen metallicity index Δm_1 for the CN calibration stars. The adopted metallicity of the calculated m_1 index is -0.76 ± 0.06 dex. The error bars represent the intrinsic uncertainty of the derived mean metallicity.

a approximately zero CN abundance values. For these two indices histograms were calculated (see Fig. 8.11). A bimodality appears to be visible for both indices.

The question of whether the incidence of CN-strong stars within M 71 might vary with evolutionary state cannot be answered. In opposite to Penny et al. (1992), who found a varying number ratio between CN-strong and CN-weak stars with a small value for the upper RGB and a larger value for the lower RGB, in the BUSCA data more CN-strong than CN-weak stars can be found in the upper RGB. Penny et al. (1992) also suggest that the cause of this variation in numbers may be deep mixing during the ascent of the RGB. In contrast Briley & Cohen (2001) found the bulk of stars with CN inhomogeneities near the main-sequence turnoff. Moreover, the shallow convective zones and low rates of CNO-cycle processing in low-mass cluster main-sequence stars make mixing of the main sequence an unlikely scenario.

As mentioned before there is an unknown offset in the relation between the spectroscopic CN abundance and the photometric m_1 deviation. One possible explanation may be that the metallicity calibration itself was influenced by CN strong stars. Then the isometallicity line of -0.76 dex in Fig. 8.6 would not represent the iron abundance but includes also the CN abundance. Also the metallicity value of the isochrone fitting of -0.98 dex (see also Geffert & Maintz (2000)) gives a hint for a lower metallicity of M 71. If one were to correct for the Δm_1 offset the iron metallicity would be ~ -1.5 dex. However, Ramírez et al. (2001) determined in their spectroscopic analysis of Fe lines of RGB stars a metallicity between -0.68 and -0.86 dex which is consistent to the metallicity calibration in this work.

8.3.2.4 Summary for M 71

For the globular cluster M 71 an age of 12 Gyr and a metallicity of $[\text{Fe}/\text{H}] = -0.98$ dex was found from the isochrone fitting to the BUSCA data. The independent Strömgen metallicity calibration of all stars in the M 71 field failed due to a large number of field stars, since M 71 is located in the galactic plane. Using the membership determination of Geffert & Maintz (2000) 128 members from

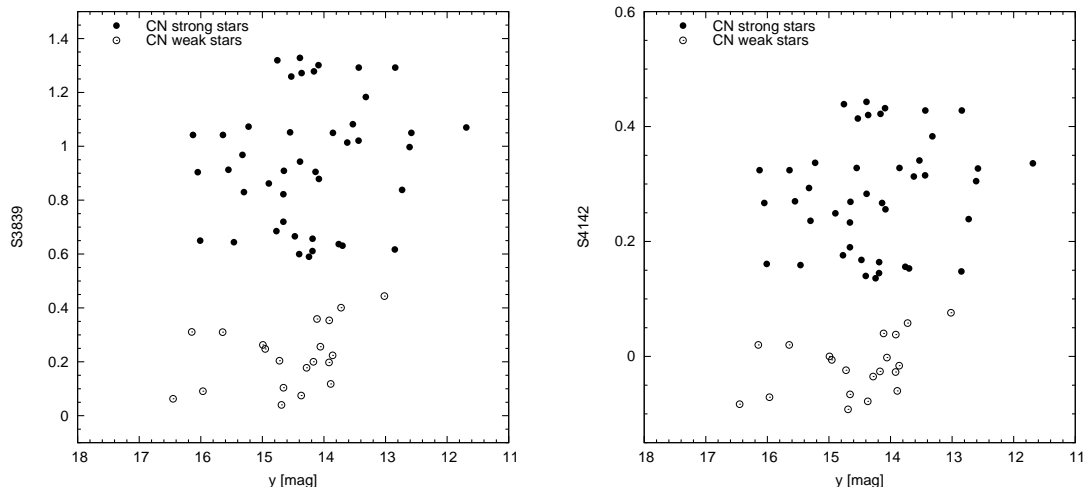


Figure 8.10: The left and right panels show plots of the photometric $S(3839)$ and $S(4142)$ indices vs. the Strömgren y magnitude. Filled and open circles are used to depict CN-strong and CN-weak stars respectively.

the BUSCA sample could be identified. For this member sample the metallicity calibration works fine and results in a metallicity of $[\text{Fe}/\text{H}] = -0.76 \pm 0.06$ dex in good agreement with the literature. The scatter in the $(b - y), m_1$ diagram can be explained by CN variation among the RGB stars. Using the spectroscopic CN abundances by Penny et al. (1992) photometric CN abundances could be calculated for the BUSCA sample. This sample shows a bimodal distribution similar to the results of Penny et al. (1992) and Smith et al. (1989) in their spectroscopic approaches by Penny et al. (1992) and Smith et al. (1989) on giant branch and red horizontal branch stars. Following Briley & Cohen (2001) who found CN variations as well as a bimodal distribution among M 71 main-sequence stars, the evolutionary scenario as an explanation can be excluded. Thus, the origin of the CN variations is still unknown.

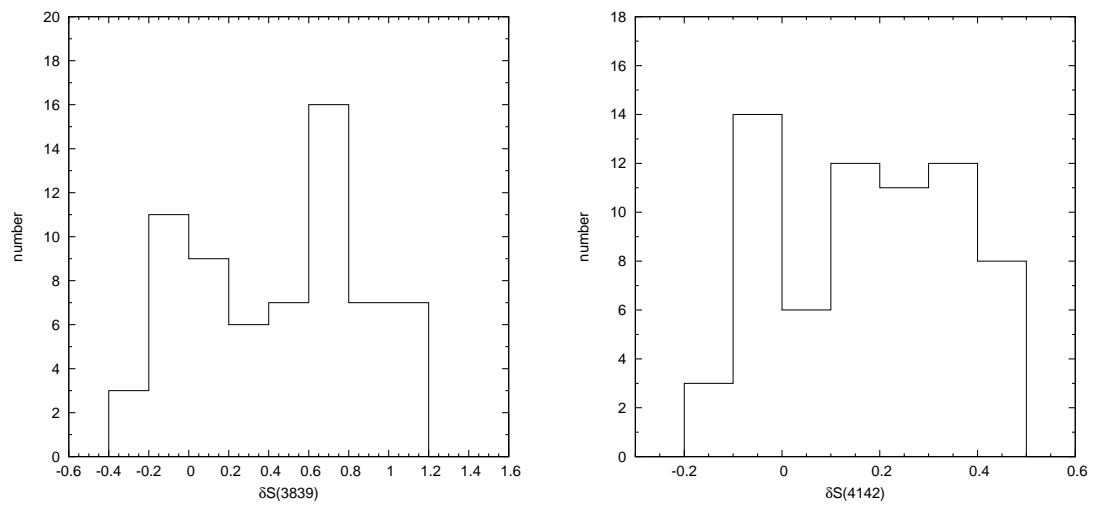


Figure 8.11: This diagram shows histograms of the CN residual indices $\delta S(3839)$ and $\delta S(4142)$.

9 Further scientific applications and the future of BUSCA

9.1 Photometric redshift determination of galaxy clusters

The detection of cosmic shear, the statistical distortion of distant galaxies by large-scale distribution of matter, has been one of the biggest observational efforts in the last years (see Bartelmann & Schneider (2000) for an extensive review on this subject). Starting with ground-based observations the cosmic shear was observed at angular scales between 1 to 10 arcminutes. But on scales smaller than 1 arcmin, where non-linear effects of structure formation are more important, high-resolution imaging provided by the Space Telescope Imaging Spectrograph (STIS) camera on board the Hubble Space Telescope (HST) is necessary. For this study a large amount of STIS data were analysed (e.g. Hämmerle et al. (2002)). The STIS images were taken without any filter in a clear mode, so for the further cosmic shear analysis no redshift information for the lensed galaxies is available. A rough knowledge of the redshift distribution of the source galaxy population would significantly improve the final accuracy on cosmological parameter estimates. The fastest way to obtain such information for is to use the photometric redshift technique. Based on the Hyperz photometric redshift code by Bolzonella et al. (2000) redshifts with an average accuracy of 0.1 can be reached using 4 different filters. The code uses a template fitting technique that accounts for the observing conditions as well as for the instrument characteristics. For this photometric analysis a project to obtain deep ground-based images (~ 10 hours) with BUSCA to observe two STIS fields with a known high number of galaxies (about 60 galaxies whereas only 20 were expected). The data for this project were taken in Jan. 2000, but the data analysis is still ongoing.

Fig. 9.1 shows one of the STIS targets observed in Jan. 2000. The same cluster observed in the four BUSCA bands UV_B , B_B , R_B , and NIR_B were shown in Fig. 9.2. In these the prominent members of this cluster are positioned in the middle and the lower right side of the images. The seeing conditions during the observing run with an average of $1.7''$ were poor. However, visible members of a known galaxy cluster (mainly red, elliptical galaxies) show decreasing intensities from the near-infrared to the ultra-violet channel. Rough determinations from the flux behaviour of the BUSCA data yields to a redshift estimate of $z \sim 0.4$ for this galaxy cluster.

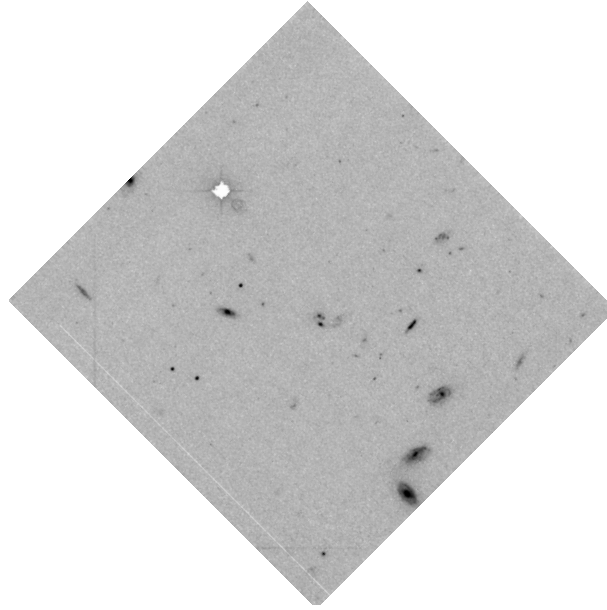


Figure 9.1: Galaxy cluster observed with the STIS camera on board the HST. The field size of the STIS camera is $\sim 50'' \times 50''$.

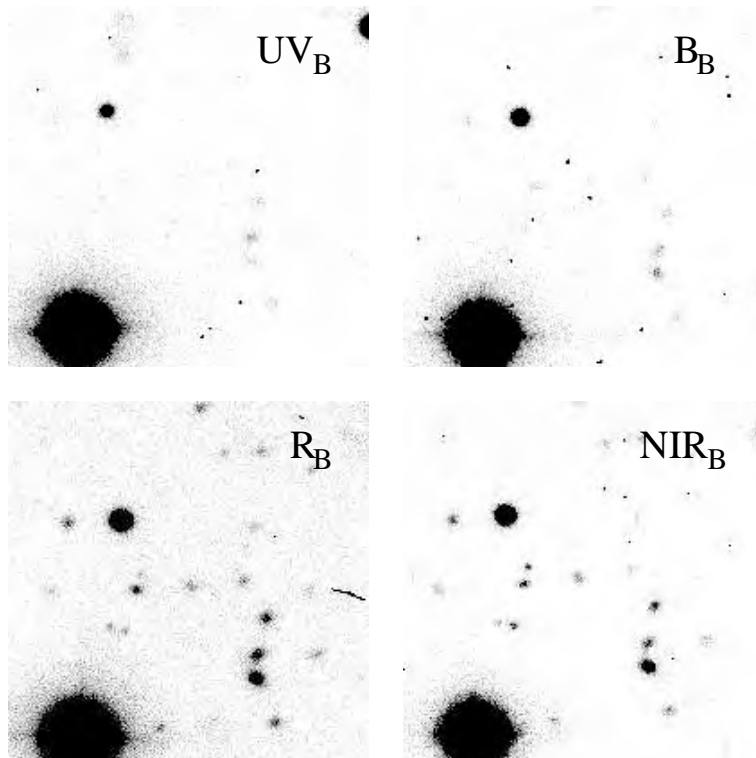


Figure 9.2: The same galaxy cluster field (see Fig. 9.1) observed in all four BUSCA bands UV_B , B_B , R_B and NIR_B . The images are scaled against each other. The galaxies of the cluster are getting fainter from the near-infrared to the ultra-violet band. From a rough investigation the redshift estimate for the cluster is $z \simeq 0.4$.

9.2 RR-Lyr stars

A further field of activity for BUSCA might be the time-resolved analysis of RR-Lyr stars with simultaneous Strömgren photometry. RR-Lyr are well known classical variables of the instability strip. The variability can be described by linear pulsation theory (e.g., Cox 1975), whereas nonlinear pulsation models were attempted to include effects of pulsational mode selection and convection (e.g., Stellingwerf 1982; Buchler & Kovacs 1986; Bono & Stellingwerf 1994). In these models the convective flux is enhanced during compression phases, diminishing the efficiency of the κ -mechanism. This may lead to brightness bumps in the ascending branch of the light curve (Stellingwerf 1984; Gehmeyr 1993). As reported in the review by Gautschy & Saio (1996) there is a considerable lack of good photometry data to verify these models.

An early attempt was the work by van Albada & de Boer (1975). They observed RR-Lyr stars photoelectrically with Strömgren filters u , v , b , and y and retrieved the actual stellar parameters T_{eff} , $\log g$ and R from a comparison with stationary model atmospheres (assuming a value for the mass of RR-Lyr stars, $M \simeq 0.7M_{\odot}$). Fig. 9.3 shows the observed light curve of an RR-Lyr star (left panel) and the corresponding atmospheric parameters Θ and $\log g$ as well the R variation (right panel).

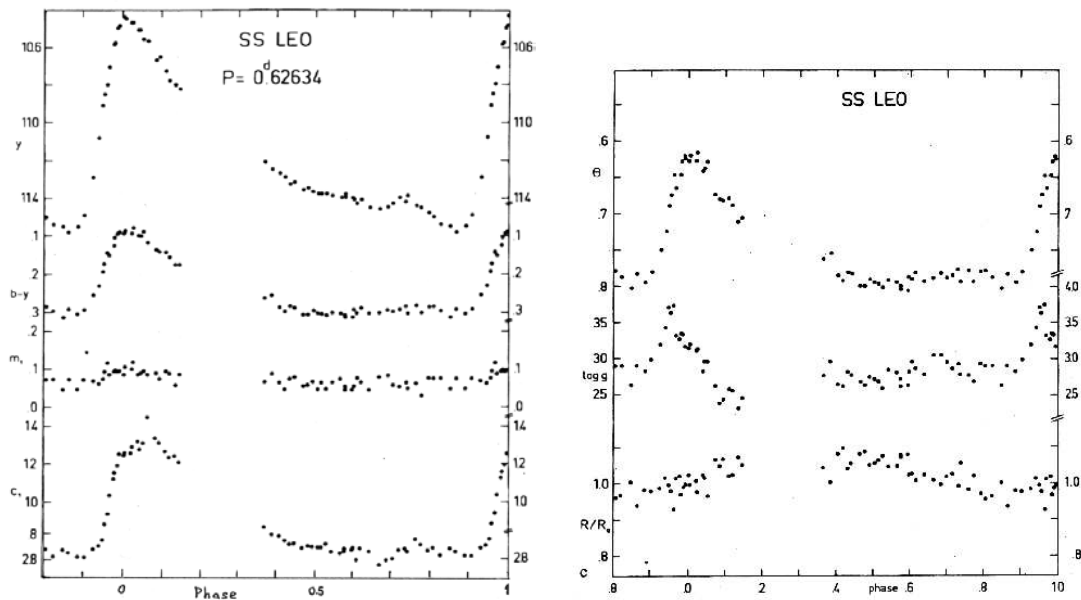


Figure 9.3: Lightcurve of the RR-Lyr star SS Leo from the Strömgren photometry (left panel) and the corresponding atmospheric parameters Θ and $\log g$, and the radius R (right panel). The bump in y at $\phi = 0.75$ with a related change in $b - y$ and c_1 shows no change in Θ .

At $\phi = 0.75$ a bump in the y brightness is clearly visible. But this photometry was done sequential (requiring interpolation in the brightness of each filter) and is in general not accurate enough to see finer details. The capability of BUSCA to observe a sample of RR-Lyr stars simultaneous in the filter u , v , b , and y will allow to investigate the nature of such bumps in more detail.

10 Summary and outlook

BUSCA

At the end of this work BUSCA is now located at the Calar Alto observatory in Spain. There BUSCA is used regularly at the 2.2m telescope. This work shows that BUSCA is fully operative after it passed all tests as shown in Ch. 5 including optical performance, the shutter, the CCDs, and the electronical system. A control software for BUSCA, which was developed during this work, is presented in Ch. 3.

The optical part of BUSCA results in images of good quality even though very bright stars in and outside of the BUSCA field cause reflections. From experience it is possible to adjust the telescope position to reduce the effect of those. The other effect, the faint Saturn like shape “star ghosts” are not avoidable but they can be easily detected. The PSF and aperture photometry will not be influenced.

The “Bonn shutter” is working fine and provides accurate short exposure times down to 0.01 seconds. A homogeneous illumination of the whole CCD can be assured.

One of the important tests made with BUSCA was to check the colour stability under non-photometric conditions. This test proves that simultaneously observing in four individual BUSCA bands can avoid the effect of small and thin clouds. The colour index variation is reduced by a factor of more than 30 compared to the variation in each individual channel, which means that clouds which cause this variation are essentially grey. However, detailed studies (see Ch. 6) show that the variations have a colour component. During large cloud extinction (~ 2 to 3 mag) the maximum deviation from the assumed grey colour is up to 0.4 mag. All analysed clouds have a slight excess in the blue extinction which makes the BUSCA $B_B - R_B$ colour index redder and the $UV_B - B_B$ bluer. A conclusive explanation for this behaviour cannot be given. However, for typical observations under photometric conditions or with small thin clouds this effect plays a negligible role.

Science projects

In the first science project of BUSCA the pulsation behaviour of the variable sdB star PG1605+072 (see Ch. 7) was analysed. In the photometric investigation in May 2002 five pulsation frequencies at 2.076, 1.9865, 2.102, 2.2695 and 1.8912 mHz in all BUSCA bands were detected. The frequencies measured in the BUSCA light curves are consistent with those of Kilkenny et al. (1999) although the time basis of all observations is much too short to resolve the full pulsation frequency spectrum of this star. More than 50 frequencies have been resolved in their long photometric study. However, the main conclusion from this investigation (see Falter et al. 2003) is that BUSCA can obtain significant results from observations of pulsating sdB stars with periods of a few minutes. Consequently, BUSCA is included in a new combined photometric and spectroscopic multi-site campaign. This project termed the MSST (Multi Site Spectroscopic Telescope) (Heber et al. 2003) makes use of different telescopes on different sites spread over the world. The observations planned covered a period of one month in May/June 2002 and were successfully accomplished. The obtained data are now in the process of reduction and analysis.

The second BUSCA science project presented deals with Strömgren photometry of Galactic globular clusters (see Ch. 8). Two globular clusters, M 12 and M 71, were observed with BUSCA. For M 12 an age of 16 ± 1 Gyr and a metallicity of -1.59 ± 0.09 dex were derived from isochrone fitting. Using the independent metallicity determination from the $(b - y), m_1$ diagram (Hilker 2000) a consistent metallicity value of $[\text{Fe}/\text{H}] = -1.58 \pm 0.05$ dex could be determined. The results are in good agreement to the values found in the literature (von Braun et al. 2002).

For the globular cluster M 71 an age of 12 Gyr and a metallicity of $[\text{Fe}/\text{H}] = -0.98$ dex was found from the isochrone fitting. The Strömgren metallicity calibration of all stars in the M 71 field failed due to a large number of field stars, since M 71 is located in the galactic plane. Using the membership determination of Geffert & Maintz (2000) 128 members from the BUSCA sample could be identified. For this member sample the metallicity calibration works fine and results in a metallicity of $[\text{Fe}/\text{H}] = -0.76 \pm 0.06$ dex, again in good agreement with the literature.

Additionally, photometric CN indices were calculated for the RGB stars of the cluster members based on the spectroscopic work by Penny et al. (1992). The CN indices show a bimodal distribution similar to the results of Penny et al. (1992) and Smith et al. (1989) in their spectroscopic approaches. The evidence of CN variation among M 71 main-sequence stars by Briley & Cohen (2001) leads to the conclusion that the discussed evolutionary scenario as an explanation for the CN variations can be excluded. Thus, the origin of the CN variations is still unknown.

Latest studies of the cosmic background radiation data from the “Wilkinson Microwave Anisotropy Probe” *WMAP* restrict the age of the universe to be 13.7 ± 0.2 Gyr (Spergel et al. 2003) which fits not to the ages of the old Galactic globular clusters, in particular the age of M 12. However, there exist new isochrones from α -enhanced stellar models including He diffusion which makes the ages of the globular clusters in general lower by 0.5 – 2 Gyr. A new age for M 12 was found to be 12-13 Gyr (Hargis et al. 2004). Unfortunately, these new isochrones are not yet available for the Strömgren filter system, so they could not be used in this work.

Future work

The studies of the CN variations of the stars in the Galactic globular clusters M 12, M 71 (this work), M 10, M 72, and NGC 6394 (Wittlich 2002) are not sufficient to understand the origin of the variations in general. To find new arguments for one of the presented scenarios (see Sect. 8.2) more data is necessary. Therefore for further studies additional data of some nearby globular clusters, e.g., M 3, M 5, and M 13 were taken with BUSCA and should soon be analysed.

Additionally, in Ch. 9 two projects, dealing with photometric redshift determination and RR Lyr stars were presented. For the first project the data was obtained. The data reduction and analysis is not finished yet. In the other project lightcurve irregularities should be studied in detail. For this observing time will be requested at the Calar Alto observatory.

11 Zusammenfassung und Ausblick (Summary in German)

BUSCA

Bei Abschluß dieser Arbeit befindet sich die BUSCA Kamera am Observatorium Calar Alto in Spanien. Dort wird diese regelmässig am 2.2m-Teleskop eingesetzt. Diese Arbeit zeigt die volle Einsatzbereitschaft der BUSCA-Kamera, nachdem alle relevanten Tests bezüglich der optischen Güte, des Shutter, der CCDs und des elektronischen Systems absolviert worden sind (siehe Kap. 5). Eine Steuerungssoftware für BUSCA, die während dieser Arbeit entwickelt worden ist, wird in Kap. 3 vorgestellt.

Die optische Qualität der Bilder, die mit BUSCA aufgenommen worden sind, ist ausgezeichnet. Einzige Einschränkungen bilden Reflektionen von hellen Sternen. Aus der Erfahrung bei den Beobachtungskampagnen kann man in den meisten Fällen die Anzahl der Reflektionen vermindern, wenn man die Teleskopposition um einen kleinen Offset verändert. Reflektionen, die als schwache saturnartige Ringe in der Nähe von hellen Sternen auftreten, lassen sich nicht verhindern. Jedoch wird dadurch weder die PSF- noch die Aperturphotometrie beeinflusst.

Der für BUSCA entwickelte "Bonn-Shutter" ermöglicht kurze Belichtungszeiten hinunter bis zu einer Länge von 0.01 Sekunden. Dabei kann eine homogene Ausleuchtung des gesamten CCDs garantiert werden.

Ein wichtiger Test der BUSCA-Kamera war das Verhalten der Farbindices unter nicht photometrischen Bedingungen. Dieser Test zeigt, daß durch die simultane Beobachtung in den vier individuellen BUSCA Farbbändern kleine und dünne Wolken keinen Einfluß auf die Photometrie haben. Die Variationen in den Farbindices sind um einen Faktor 30 kleiner als die Variation in jedem individuellen Farbband. Dies zeigt auch, daß Wolken im allgemeinen eine graue Farbe besitzen (in jedem Farbband wird der gleiche Anteil des Lichts absorbiert). Eine genauere Untersuchung dieses Verhaltens (siehe Kap. 6) jedoch zeigt, daß die Variationen der Farbindices eine Farbabhängig sind. Beim Durchzug von großen Wolken (entsprechend einer Abschwächung von ~ 2 to 3 mag) ist die Abweichung in den Farbindices von der angenommenen grauen Farbe etwa 0.4 mag. Alle untersuchten Wolken zeigen einen leichten Farbexcess, welches den BUSCA-Farbindex $B_B - R_B$ röter und den Index $UV_B - B_B$ blauer macht. Eine schlüssige Erklärung für dieses Verhalten kann nicht gegeben werden. Für typische photometrische Beobachtungen oder bei der Beobachtung durch dünne Wolken spielt dieser Effekt eine vernachlässigbare Rolle.

Wissenschaft mit BUSCA

In einem ersten wissenschaftlichen Projekt mit BUSCA wurde das Pulsationsverhalten des variablen sdB Sterns PG1605+072 (siehe Kap. 7) untersucht. Dabei wurden in den Beobachtungskampagnen im Mai 2002 fünf Pulsationsfrequenzen bei 2.076, 1.9865, 2.102, 2.2695 und 1.8912 mHz in allen BUSCA-Farbbändern gemessen. Diese Werte aus den Lichtkurven sind konsistent mit den

gemessenen Werten von Kilkenny et al. (1999), obwohl die Länge der Beobachtungen zu kurz war, um das Frequenzspektrum aller Pulsationen aufzulösen. Kilkenny et al. (1999) haben mehr als 50 verschiedene Frequenzen in ihren Studien gefunden. Ein wichtiges Resultat dieser BUSCA-Studie ist jedoch, daß mit dieser Kamera Pulsationsperioden bei variablen sdB Sternen im Minutenbereich nachgewiesen werden können (siehe Falter et al. 2003). Aus diesem Grunde ist BUSCA in einem neuen kombinierten photometrischen und spektroskopischen Projekt eingebunden. Dieses Projekt mit Namen MSST (Multi Site Spectroscopic Telescope) (Heber et al. 2003) macht Gebrauch von vielen Teleskopen an verschiedenen über die ganze Welt verteilte Observatorien. Die Beobachtungen sind für etwa 30 Tage im Mai/Juni 2002 geplant worden und wurden erfolgreich durchgeführt. Die dabei aufgenommenen Daten sind im Augenblick noch in der Phase der Reduktion und Auswertung.

Das zweite vorgestellte BUSCA Projekt behandelt die Strömgren-Photometrie von galaktischen Kugelsternhaufen (siehe Kap. 8). Dazu wurden zwei Kugelsternhaufen, M 12 und M 71, mit BUSCA beobachtet. Für M 12 konnte ein Alter von 16 ± 1 Gyr und eine Metallizität von -1.59 ± 0.09 dex durch Anpassung von Isochronen bestimmt werden. Die davon unabhängige Metallizitätsbestimmung mittels des $(b - y), m_1$ -Diagramms (Hilker 2000) liefert eine dazu konsistente Metallizität von $[Fe/H] = -1.58 \pm 0.05$ dex. Diese Resultate stehen im Einklang mit den Literaturwerten (z.B. von Braun et al. 2002).

Für den Kugelsternhaufen M 71 wurde ein Alter von 12 Gyr und eine Metallizität von $[Fe/H] = -0.98$ dex aus der Isochronenanpasung bestimmt. Allerdings schlug die Strömgren-Metallizitätskalibration aller Sterne in dem beobachteten M 71-Feld fehl. Dies liegt an der großen Zahl von Feldsternen in den Aufnahmen, welches von der Lage von M 71 in der galaktischen Ebene herrührt. Mittels der Arbeit von Geffert & Maintz (2000) wurden 128 Sterne als Haufenmitglieder identifiziert. Für diesen eingeschränkten Satz von Sternen gelang die Metallizitätskalibration und liefert eine Metallizität von $[Fe/H] = -0.76 \pm 0.06$ dex in guter Übereinstimmung zur Literatur.

Zusätzlich wurden für die roten Riesenaststerne (aus dem Mitgliedersample) photometrische CN-Indices auf Basis der Arbeit von Penny et al. (1992) berechnet. Diese CN-Indices zeigen eine bimodale Verteilung, wie sie ähnlich auch von Penny et al. (1992) und Smith et al. (1989) bei ihren spektroskopischen Untersuchungen gefunden haben. Der weitere Nachweis von CN-Variationen bei Hauptreihensternen von M 71 durch Briley & Cohen (2001) schließt das diskutierte Evolutionsmodell als Grund für die CN-Variationen aus. Die Ursache dieser CN-Variationen ist weiter unklar.

Neueste Untersuchungen der kosmischen Hintergrundstrahlung mit dem *WMAP*-Instrumentes (Wilkinson Microwave Anisotropy Probe) beschränken das Alter des Universums auf 13.7 ± 0.2 Gyr (Spergel et al. 2003). Diese Beschränkung paßt nicht zu den hohen Altern einiger galaktischen Kugelsternhaufen, insbesondere nicht zu M 12 mit seinen 16 Gyr. Es existieren jedoch inzwischen neuere Isochronen, die für stellare Modelle mit α -Elementanreicherung gerechnet wurden. Diese beinhalten zusätzlich Modelle zur He-Diffusion, welches das Alter der Kugelsternhaufen im allgemeinen zwischen 0.5 – 2 Gyr reduziert. Ein neues Alter von 12-13 Gyr für M 12 konnte von Hargis et al. (2004) bestimmt werden. Leider sind die neuen Isochronen nicht für das Strömgren-Filtersystem verfügbar und konnten nicht in dieser Arbeit verwendet werden.

Ausblick

Die Studien der CN Variationen in Sternen der galaktischen Kugelhaufen M 12, M 71 (diese Arbeit), M 10, M 72 und NGC 6394 (Wittlich 2002) sind nicht ausreichend, um die Herkunft dieser Variationen zu verstehen. Um das eine oder andere Modell zur Ursache der CN-Variationen zu untermauern, müssen weitere Daten gesammelt werden. Dazu wurden von mehreren nahen Kugelhaufen wie M 3,

M 5 und M 13 Daten mit BUSCA aufgenommen und sollen bald analysiert werden.

In Kap. 9 wurden zwei weitere Projekte vorgestellt. Im ersten sollen mit BUSCA photometrische Rotverschiebungen von Galaxien berechnet werden. Die Daten dazu wurden bereits im Januar 2002 aufgenommen, sind aber ebenfalls noch nicht analysiert worden. Im zweiten zukünftigen Projekt sollen Irregularitäten in den Lichtkurven von RR Lyrae-Sternen genauer untersucht werden. Dazu wird am Calar Alto Observatorium Beobachtungszeit beantragt.

A BUSCA software

A.1 Commands from the MP

The following sections list all commands which are sent from the main program (MP) to the graphical user interface (GUI). The list is divided into common commands and special commands for the filter and status panel in the GUI.

A.1.1 Common commands

CDD *min1 max1 ... max4*

sends the default minimum,maximum values for the realtime display; between these values all data points are plotted in greyscales

CDS *min1 max1 ... max4*

sets the minimum,maximum values for the realtime display (answer of the CCD request)

CDT

request for the size of the realtime display windows

CEC

changes the meaning of the two large buttons in the GUI from “Start Exposure” and “Flush CCD” to “Pause” and “Break”

CEF *name*

sets the name of the last taken exposure in the GUI

CEL *timeleft expleft*

sets the time and number left of the current exposure task in the GUI

CEN *nr*

sets the number of the next exposure in the GUI

CEO

inform the GUI that all exposures are finished

CEP

requests the data of the observer

CER *nr*

sends the highest number+1 of all stored files (answer of the CER request)

CFO

signals the end of the CCD flushing procedure

CIP

sets the path of the stored images in the GUI

IA

the MP is still running

ID *title {text} bitmap buttondefs*

invokes a dialog box with *title* and *text*; *bitmap* defines a bitmap in box: error, information, confirmation; with *buttondefs* the name of the used buttons are defined, e.g. Ok , Cancel

IE *colour msg*

writes the message *msg* with *colour* (0=black, 1=red, 2=green) into the errorlog window

IF

this is sent when the MP crashes with a segmentation fault

IQ

confirm of the quit request

IS *colour msg*

sets the message in the status bar to *msg* using *colour* (0=black, 1=red, 2=green)

LCDR *msg*

puts the message *msg* received from the CCD controller in the low-level terminal window

LCDS *msg*

puts the message *msg* send to the CCD controller in the low-level terminal window

LDDR *msg*

puts the message *msg* received from the UC controller in the low-level terminal window

LDDS *msg*

puts the message *msg* send to the UC controller in the low-level terminal window

UTE *chn1 chn2 chn3 chn4*

sets the current evaporation rate of the CCDs in the temperature dialog

UTH *chn1 chn2 chn3 chn4*

sets the current heating percentage of the CCDs in the temperature dialog

UTI *chn1 chn2 chn3 chn4*

sets the current temperatures of the CCDs in the temperature dialog

UTS *chn1 chn2 chn3 chn4*

sets the operating temperatures of the CCDs in the temperature dialog

A.1.2 Filter commands

UFA *nr name*

adds a new filter definition *name* to the filter set combobox

UFC

clears all filter set definitions

UFD *nr*

sets the status of of filterwheel *nr* to “driving”

UFF *nr*

sets the status of of filterwheel *nr* to “fail”

UFN *chn nr*

sets the name of the filter *nr* in channel *chn*

UFS *chn nr*
marks the filter *nr* in channel *chn* as selected

UFU *nr*
unlocks the filter control of filterwheel *nr*

A.1.3 Status commands

SA *msg*
sends the status of the CCDs, e.g. exposing to the GUI

SC *status*
sends the status of the CCD controller to the GUI (*status*=1 OK, =0 fail)

SD *usage free status*
sends the disk-free status of the used hard disk to the GUI, if *usage* is 1 there is less than 128MB free space left of the hard disk which is necessary to save a 4k×4k exposure

SF *chn status*
sends the status of filter wheel in channel *chn* to the GUI (*status*=0 OK, =1 fail)

SI *directory*
sends the image path to the GUI

SL *nr status*
sends the status of the LN2 of the dewar *nr* to the GUI (*status*=0 OK, =1 low, =2 fail)

SP *name*
sends the *name* of the current pattern file to the GUI

ST *status*
sends the current status of the TCP module to the GUI

SU *status*
sends the status of the UC controller to the GUI (*status*=1 OK, =0 fail)

SV *status*
sends the status of the voltages to the GUI

A.2 Commands from the GUI

In this section all commands which are sent from the GUI to the MP are listed. The list is divided into common, exposure, filter, temperature and shutter commands. At the end of this section the requests from the GUI are listed.

A.2.1 Common commands

CA
activate the CCD controller

CC *mode*
continuous scan mode on/off (*mode*=1 is on)

CDS *min1 max1 ... min4 max4*
set minimum,maximum value for the realtime display; between these values all data points are plotted in greyscales

- CDT *size_x size_y*
sets the size of the realtime display windows
- CF
flushes the CCDs
- CRS
resets the CCD controller via serial device
- CPD *file*
load the pattern from *file*
- CPR
reload previous loaded pattern file
- CV *mode*
switch voltages on/off (*mode*=1 is on)
- ID *answer*
return of the dialog request from the MP to the GUI; the value of *answer* is the number of the button pressed
- IQ
quits the program
- LCS *cmd*
sends the low-level command *cmd* to the CCD controller
- LDS *cmd*
sends the low-level command *cmd* to the UC controller
- UA
activate UC controller
- IQ
quits the program

A.2.2 Exposure commands

- CEB
pauses the current exposure
- CEC *x1 x2 y1 y2 binx biny act (4x) gain (4x)*
sets the CCD parameters, *x1*, *x2*, *y1*, *y2* and the binning mode; the four parameters *act* are set to 1 if the resp. channel is used, otherwise 0; four *gain* values are given for each CCD
- CEE *exptime nexp shift nshifts delay shiftmode startfocus incfocus exptype "object"*
sets the exposure parameters *exptime* and number of exposures *nexp*; the *shift*, *nshifts* and *delay* are used in the case the CCD frame has to be shifted; for focus images, the *startfocus* and the increment *incfocus* are given; *exptype* and *object* stands for the type and name of the next exposure
- CEF *name savepath prefix*
sets the observers *name*, the directory for storing the images and a *prefix* of the image names, e.g. prefix "bu" and the resulting image name "bu012456a.fits"
- CEI
breaks the current exposure

CEQ *nr exptime1 filter11 filter12 filter13 filter14 ...*

sets the configuration for sequence images; *nr* is the number of used configurations; each configuration consists of the exposure time *exptimeX* and the filter definitions *filterX1*, *filterX2*, *filterX3* and *filterX4*

CES *modus*

start a new exposure; *modi* are *normal*, *multiple*, *readout*, *shift*, *shutter* and *prepare*

A.2.3 Filter commands

UFP *nr*

selects filter combination *nr*

UFS *chn pos*

selects the filter in channel *chn* position *pos*

URF *nr*

resets the filter wheel number *nr* (=0, all filter wheels)

A.2.4 Shutter and temperature commands

URS

resets the shutter

UTN *chn val*

sets the working temperature of the CCD of channel *chn* to *val*

UTU

force a temperature update

A.2.5 Requests

CDD

requests the realtime display values

CER *directory prefix*

requests the highest+1 number of all stored files with *prefix* in *directory*

IA

ping request from the GUI to check if the MP is still running

B Artificial Bias

As described in Sect. 4.1.1 the most standard method to correct bias effects is to combine single bias frames to a masterbias. The readout noise can be reduced if as many as possible frames are used. The problem with the noise plays an important role in the data reduction process when the readout noise is not small or very accurate photometry is intended. Also the use of the “noisy” masterbias increases the noise in the science frame during bias and flat field correction so the the signal to noise ratio of the science frames decreases. To avoid these problems we tried to create artificial bias frames from masterbias frames, which fit all the bias effects but is noise free.

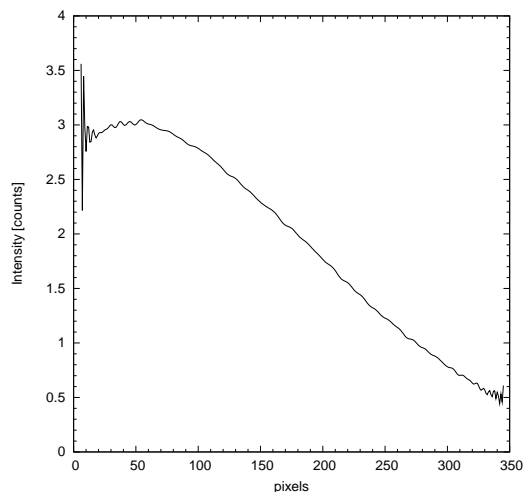


Figure B.1: This diagram shows the bias structure in x-directions in an artificial bias frame (for the yellow-green channel of BUSCA). The electronic artefacts from the controller with a typical amplitude of three counts show two effects, a sinoidal function and an overlying profile.

Studying several bias frames shows that all the bias effects can be described with sinoidal, power law or linear functions. The IRAF package provides tasks to fit pixel lines and pixel rows of CCD frames with Legendre and Chebyshev polynomials and spline functions of variable orders. For the fitting process all lines or rows are combined, so the disturbing noise is nearly suppressed and the bias effects are displayed prominently. After empirical testing it turns out that the use of Legendre polynomials with high (>10) order gives the best results. Fig. B.1 sketches a line of a bias frame showing a sinoidal effect with an overlying gradient and the function used for modelling the bias line. The images in Fig. B.2 clarify the advantage of the bias modelling process. The image on the bottom left is the difference of the masterbias and the synthetic bias and shows only the noise in the masterbias. In the upper right image the bias effect pattern is clearly visible.

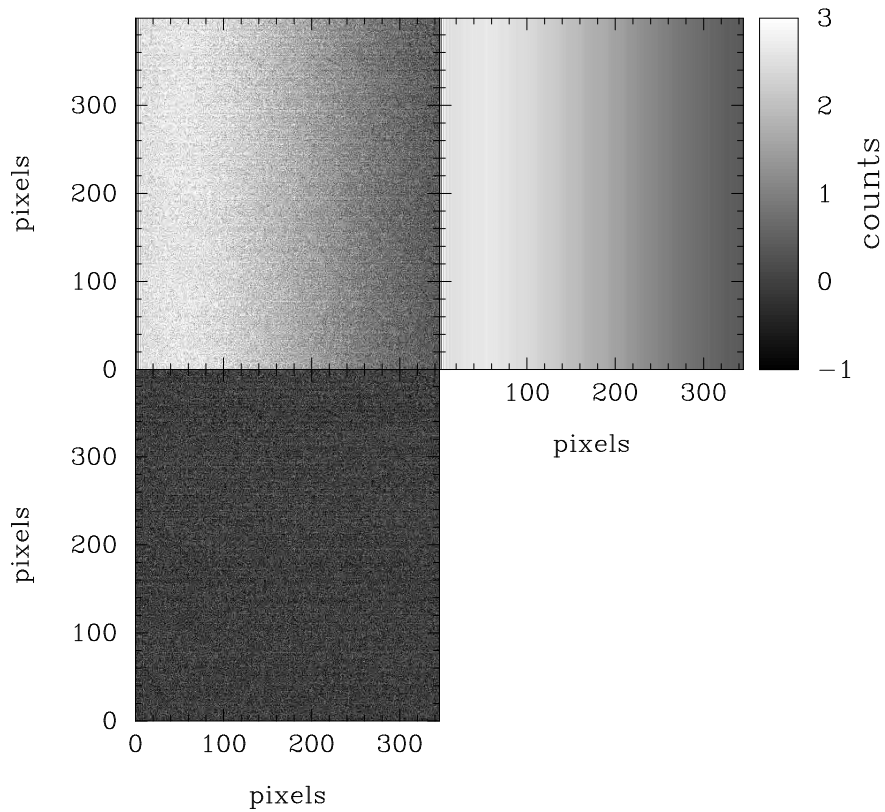


Figure B.2: This figure shows the construction of an artificial bias frame. In the upper left panel there is a stacked master bias of 56 single bias frame for the yellow-green channel. The upper right panel shows the calculated artificial bias frame and in the lower left frame the “reduced” noise pattern can be seen.

C First order linear transformation

For star pairing with BUSCA the task is to transform n coordinate sets of n stars (x_i, y_i) in one CCD frame to the coordinate system of another CCD frame (x'_i, y'_i) (see Sect. 4.2.2). One algorithm which solves this problem mathematically is a first order linear transformation (see Eq. C.1). This transformation provides a rotation and scaling with the parameters a, b, c and d as well as a translation with the parameters e and f and will be now described in detail.

$$\begin{pmatrix} x' \\ y' \end{pmatrix} = \begin{pmatrix} a & b \\ c & d \end{pmatrix} \cdot \begin{pmatrix} x \\ y \end{pmatrix} + \begin{pmatrix} e \\ f \end{pmatrix} \quad (\text{C.1})$$

Necessarily one needs six different coordinate pairs (x, y) and (x', y') to solve this linear problem. The results for each parameter can be determined very easily.

Generally in astronomy, for this equation there exist in general more stars which can be used for calculating the transformation. The reason to use more than six stars is justified by the fact that each star coordinate has an intrinsic inaccuracy. Typically in such cases only numerical fitting algorithms, which can cause a lot of technical problems in their implementation, lead to good results. However, for this special problem there is a simple solution which solves the equation directly.

First the transformation equation can be split in two separate equations (see Eq. C.2) in which the vectors $\vec{x}', \vec{y}', \vec{b}$ and \vec{c} and the matrix \mathbf{A} are defined as:

$$\begin{aligned} \vec{x}' &= \begin{pmatrix} x'_1 \\ x'_2 \\ \vdots \\ x'_n \end{pmatrix}, \vec{y}' = \begin{pmatrix} y'_1 \\ y'_2 \\ \vdots \\ y'_n \end{pmatrix} \\ \vec{b} &= \begin{pmatrix} a \\ b \\ e \end{pmatrix}, \vec{c} = \begin{pmatrix} c \\ d \\ f \end{pmatrix} \\ \mathbf{A} &= \begin{pmatrix} x_1 & y_1 & 1 \\ x_2 & y_2 & 1 \\ \vdots & \vdots & \\ x_n & y_n & 1 \end{pmatrix} \\ \vec{x}' &= \mathbf{A} \cdot \vec{b} \\ \vec{y}' &= \mathbf{B} \cdot \vec{c} \end{aligned} \quad (\text{C.2})$$

The analytical solution of the equations C.2 is shown exemplary for the x' transformation:

$$\begin{aligned} \vec{x}' &= \underbrace{\mathbf{A}}_{n \times 3} \cdot \vec{b} \\ \underbrace{\mathbf{A}^t}_{3 \times n} \cdot \vec{x}' &= \underbrace{(\mathbf{A}^t \mathbf{A})}_{3 \times 3} \cdot \vec{b} \\ (\mathbf{A}^t \mathbf{A})^{-1} \mathbf{A}^t \cdot \vec{x}' &= \underbrace{(\mathbf{A}^t \mathbf{A})^{-1} (\mathbf{A}^t \mathbf{A})}_{=1} \cdot \vec{b} \\ \vec{b} &= (\mathbf{A}^t \mathbf{A})^{-1} \mathbf{A}^t \cdot \vec{x}' \end{aligned}$$

The error of this transformation cannot be given for each parameter a, \dots, f . Instead only an error for the x and y transformation can be calculated. The error for x is the mean deviation Δx of the transformed coordinate x_t and the given coordinate x' :

$$\Delta x = \frac{1}{n} \sum_{i=1}^n |x'_i - x_t|$$

The equation for Δy is defined respectively.

Bibliography

- Altmann M., Edelman H., de Boer K. S., 2004: Studying the populations of our Galaxy using the kinematics of sdB stars; *A&A* 414, 181–201
- Bagschik K., 2001: *The open clusters NGC 7128 and NGC 7788 and the evolution of the BUSCA beam-splitter array*; PhD thesis; Sternwarte der Universität Bonn
- Bartelmann M., Schneider P., 2000: Weak gravitational lensing; *Physics Report* 340, 291
- Bell R. A., Hesser J. E., Cannon R. D., 1983: Spectroscopic analysis of dwarf and subgiant stars in 47 Tucanae; *ApJ* 269, 580–591
- Bell R. A., Hesser J. E., Cannon R. D., 1984: Spectroscopy over a range of 5 magnitudes in NGC 6752; *ApJ* 283, 615–625
- Bergbusch P. A., Vandenberg D. A., 1992: Oxygen-enhanced models for globular cluster stars. II - Isochrones and luminosity functions; *ApJS* 81, 163–220
- Bolzonella M., Miralles J.-M., Pelló R., 2000: Photometric redshifts based on standard SED fitting procedures; *A&A* 363, 476–492
- Bono G., Stellingwerf R. F., 1994: Pulsation and stability of RR Lyrae stars. 1: Instability strip; *ApJS* 93, 233–269
- Bracewell R., 1965: *The Fourier Transform and its applications*; McGraw-Hill Electrical and Electronic Engineering Series, New York: McGraw-Hill, 1965
- Brassard P., Fontaine G., Billères M., et al., 2001: Discovery and Asteroseismological Analysis of the Pulsating sdB Star PG 0014+067; *ApJ* 563, 1013–1030
- Briley M. M., Cohen J. G., 2001: Calibration of the CH and CN Variations Among Main-Sequence Stars in M71 and in M13; *AJ* 122, 242–247
- Briley M. M., Hesser J. E., Bell R. A., 1991: C and N abundances among 47 Tucanae main-sequence stars; *ApJ* 373, 482–496
- Briley M. M., Smith G. H., Bell R. A., Oke J. B., Hesser J. E., 1992: CN and CH variations on the M5 subgiant branch; *ApJ* 387, 612–621
- Brown T. M., Bowers C. W., Kimble R. A., Sweigart A. V., Ferguson H. C., 2000: Detection and Photometry of Hot Horizontal Branch Stars in the Core of M32; *ApJ* 532, 308–322
- Brown T. M., Ferguson H. C., Davidsen A. F., Dorman B., 1997: A Far-Ultraviolet Analysis of the Stellar Populations in Six Elliptical and S0 Galaxies; *ApJ* 482, 685
- Buchler J. R., Kovacs G., 1986: On the modal selection of radial stellar pulsators; *ApJ* 308, 661–668
- Buonanno R., Castellani V., Smriglio F., 1976: M10 and M12: A Couple of Interacting Twin Globular Clusters?; *Ap&SS* 41, L3
- Cannon R. D., Croke B. F. W., Bell R. A., Hesser J. E., Stathakis R. A., 1998: Carbon and nitrogen abundance variations on the main sequence of 47 Tucanae; *MNRAS* 298, 601–624
- Carbon D. F., Romanishin W., Langer G. E., et al., 1982: Carbon and nitrogen abundances in giant stars of the metal-poor globular cluster M92; *ApJS* 49, 207–258
- Charpinet S., 2001: The pulsations in subdwarf B stars; *Astronomische Nachrichten* 322, 387–393
- Charpinet S., Fontaine G., Brassard P., et al., 1997: A Driving Mechanism for the Newly Discovered

- Class of Pulsating Subdwarf B Stars; ApJ 483, L123
- Cohen J. G., 1999a: The Spectra of Main-Sequence Stars in Galactic Globular Clusters. I. CH and CN Bands in M13; AJ 117, 2428–2433
- Cohen J. G., 1999b: The Spectra of Main-Sequence Stars in Galactic Globular Clusters. II. CH and CN Bands in M71; AJ 117, 2434–2439
- Cohen J. G., Briley M. M., Stetson P. B., 2002: Carbon and Nitrogen Abundances in Stars at the Base of the Red Giant Branch in M5; AJ 123, 2525–2540
- Cousins A. W. J., Caldwell J. A. R., 1998: Atmospheric extinction in the U band; The Observatory 118, 85–98
- Cox J. P., 1975: Stellar oscillations, stellar stability and application to variable stars; Memoires of the Societe Royale des Sciences de Liege 8, 129–159
- Cudworth K. M., 1985: Photometry, proper motions, and membership in the globular cluster M71; AJ 90, 65–73
- Dorman B., Rood R. T., O’Connell R. W., 1993: Ultraviolet Radiation from Evolved Stellar Populations. I. Models; ApJ 419, 596
- Dreizler S., Schuh S. L., Deetjen J. L., Edelmann H., Heber U., 2002: HS0702+6043 - A new large amplitude sdB variable at the cool end of the instability region; A&A 386, 249–255
- Falter S., Heber U., Dreizler S., et al., 2003: Simultaneous time-series spectroscopy and multi-band photometry of the sdBV PG 1605+072; A&A 401, 289–296
- Gautschy A., Saio H., 1996: Stellar Pulsations Across the HR Diagram: Part 2; ARAA 34, 551–606
- Geckeler R., 1998: PhD thesis; Eberhard-Karls-Universität Tübingen
- Geffert M., Maintz G., 2000: First results of a photometric and astrometric study of the globular cluster M 71 (NGC 6838); A&AS 144, 227–233
- Gehmeyr M., 1993: On nonlinear radial oscillations in convective RR Lyrae stars. III - A full-amplitude investigation of the red edge; ApJ 412, 341–350
- Gratton R. G., Bonifacio P., Bragaglia A., et al., 2001: The O-Na and Mg-Al anticorrelations in turn-off and early subgiants in globular clusters; A&A 369, 87–98
- Grebel E. K., Richtler T., 1992: Metallicities from CCD Stromgren photometry of the young cluster NGC 330 and nearby field stars in the Small Magellanic Cloud; A&A 253, 359–365
- Greggio L., Renzini A., 1990: Clues on the hot star content and the ultraviolet output of elliptical galaxies; ApJ 364, 35–64
- Greggio L., Renzini A., 1999: The UV emission of elliptical galaxies.; Memorie della Societa Astronomica Italiana 70, 691–708
- Grundahl F., Stetson P. B., Andersen M. I., 2002: The ages of the globular clusters M 71 and 47 Tuc from Strömgren uvby photometry. Evidence for high ages; A&A 395, 481–497
- Hämmerle H., Miralles J.-M., Schneider P., et al., 2002: Cosmic shear from STIS pure parallels. II. Analysis; A&A 385, 743–760
- Harbeck D., 2000: *Simultanphotometrie von Sternfeldern: 4k²-CCD Chips für BUSCA und der Kugelsternhaufen NGC 2808*; Diploma thesis; Sternwarte der Universität Bonn
- Harbeck D., Smith G. H., Grebel E. K., 2003: CN Abundance Variations on the Main Sequence of 47 Tucanae; AJ 125, 197–207
- Hargis J. R., Sandquist E. L., Bolte M., 2004: The Luminosity Function and Color-Magnitude Diagram of the Globular Cluster M12; ApJ 608, 243–260
- Harris W. E., 1996: A Catalog of Parameters for Globular Clusters in the Milky Way; AJ 112, 1487
- Heber U., 1986: The atmosphere of subluminous B stars. II - Analysis of 10 helium poor subdwarfs and the birthrate of sdB stars; A&A 155, 33–45

- Heber U., Dreizler S., Schuh S. L., et al., 2003: Photometric and Spectroscopic Monitoring of the sdBV star PG 1605+072: The Multi-Site Spectroscopic Telescope (MSST) Project; in *White Dwarfs, proceedings of the conference held at the Astronomical Observatory of Capodimonte, Napoli, Italy*. <http://www.na.astro.it/meetings/wd2002/wd.html>. To be published by Kluwer. (*NATO Science Series II – Mathematics, Physics and Chemistry, Vol. 105, p. 105.*); p. 105
- Heber U., Moehler S., Napiwotzki R., Thejll P., Green E. M., 2002: Resolving subdwarf B stars in binaries by HST imaging; *A&A* 383, 938–951
- Heber U., Reid I. N., Werner K., 1999: Spectral analysis of the multi mode pulsating subluminoous B star PG 1605+072; *A&A* 348, L25–L28
- Hesser J. E., 1978: Spectral Inhomogeneities in Faint 47 Tucanae Stars; *ApJ* 223, L117
- Hesser J. E., Harris G. L. H., Bell R. A., Cannon R. D., 1984: Spectroscopy of Main-Sequence and Subgiant Stars in Globular Star Clusters; in *IAU Symp. 105: Observational Tests of the Stellar Evolution Theory*; p. 139
- Hilker M., 2000: Revised Strömgen metallicity calibration for red giants; *A&A* 355, 994–1002
- Jønch-Sørensen H., 1993: Uvby-Beta Photometry of E-Region Stars; *A&AS* 102, 637
- Kilkenny D., Koen C., O’Donoghue D., Stobie R. S., 1997: A new class of rapidly pulsating star - I. EC 14026-2647, the class prototype; *MNRAS* 285, 640–644
- Kilkenny D., Koen C., O’Donoghue D., et al., 1999: The EC 14026 stars - X. A multi-site campaign on the sdBV star PG 1605+072; *MNRAS* 303, 525–534
- Kohley R., 1998: *Multicolor CCD-photometry of M34 under the aspect of the instrumental development of BUSCA*; PhD thesis; Sternwarte der Universität Bonn
- Kraft R. P., 1994: Abundance differences among globular-cluster giants: Primordial versus evolutionary scenarios; *PASP* 106, 553–565
- Macted P. F. L., Heber U., Marsh T. R., North R. C., 2001: The binary fraction of extreme horizontal branch stars; *MNRAS* 326, 1391–1402
- Minnaert M. G. J., 1993: *Light and color in the outdoors*; New York: Springer, |c1993
- Moehler S., Heber U., Rupprecht G., 1997: Hot HB stars in globular clusters: physical parameters and consequences for theory III. NGC 6752 and its long blue vertical branch.; *A&A* 319, 109–121
- Monet D. E. A., 1998: A catalogue of astrometric standards.; in *The PMM USNO-A2.0 Catalog. (1998)*
- Norris J., 1987: The ellipticities of globular clusters and the cyanogen problem; *ApJ* 313, L65–L68
- Osborn W., 1971: Two new CN-strong globular cluster stars; *The Observatory* 91, 223–224
- O’Toole S. J., Bedding T. R., Kjeldsen H., Dall T. H., Stello D., 2002: Time-series spectroscopy of pulsating sdB stars - II. Velocity analysis of PG1605+072*; *MNRAS* 334, 471–480
- O’Toole S. J., Bedding T. R., Kjeldsen H., et al., 2000: Time Series Spectroscopy of Pulsating Subdwarf B Stars: PG 1605+072; *ApJ* 537, L53–L56
- Penny A. J., Smith G. H., Churchill C. W., 1992: CN and CH inhomogeneities among lower giant branch stars in M71; *MNRAS* 257, 89–96
- Perry C. L., Olsen E. H., Crawford D. L., 1987: A catalog of bright UBVY beta standard stars; *PASP* 99, 1184–1200
- Piccioni A., Bartolini C., Bernabei S., et al., 2000: A pulsation episode from the sdB star PG 0856+121; *A&A* 354, L13–L16
- Ramírez S. V., Cohen J. G., Buss J., Briley M. M., 2001: Abundances in Stars from the Red Giant Branch Tip to Near the Main-Sequence Turnoff in M71. II. Iron Abundance; *AJ* 122, 1429–1437
- Reif K., Bagschik K., de Boer K., et al., 1999: BUSCA: A Telescope Instrumentation for Simultaneous Imaging in 4 Optical Bands; *SPIE Vol. 3649*, 109

- Richter P., Hilker M., Richtler T., 1999: Strömgren photometry in globular clusters: M55 & M22; *A&A* 350, 476–484
- Richtler T., 1989: Stroemgren photometry of late-type supergiants in the Small Magellanic Cloud; *A&A* 211, 199–207
- Saffer R. A., Bergeron P., Koester D., Liebert J., 1994: Atmospheric parameters of field subdwarf B stars; *ApJ* 432, 351–366
- Saffer R. A., Green E. M., Bowers T., 2001: The Binary Origins Of Hot Subdwarfs: New Radial Velocities; in *ASP Conf. Ser. 226: 12th European Workshop on White Dwarfs*; p. 408
- Schmoll J., 1997: *Ein optischer Testaufbau für die Bonner Vierfarb-Simultankamera*; Diploma thesis; Sternwarte der Universität Bonn
- Schuh S., Dreizler S., Deetjen J. L., Heber U., Geckeler R. D., 2000: CCD Photometry of Variable Subdwarfs and White Dwarfs at Calar Alto Observatory; *Baltic Astronomy* 9, 395–402
- Silvotti R., Solheim J.-E., Gonzalez Perez J. M., et al., 2000: PG 1618+563B: A new bright pulsating sdB star; *A&A* 359, 1068–1074
- Smith G. H., 1987: The chemical inhomogeneity of globular clusters; *PASP* 99, 67–90
- Smith G. H., Bell R. A., Hesser J. E., 1989: CN and CH variations among subgiants in the globular cluster 47 Tucanae; *ApJ* 341, 190–200
- Spergel D. N., Verde L., Peiris H. V., et al., 2003: First-Year Wilkinson Microwave Anisotropy Probe (WMAP) Observations: Determination of Cosmological Parameters; *ApJS* 148, 175–194
- Stellingwerf R. F., 1982: Convection in pulsating stars. I - Nonlinear hydrodynamics. II - RR Lyrae convection and stability; *ApJ* 262, 330–343
- Stellingwerf R. F., 1984: Convection in pulsating stars. V - Limit cycle characteristics; *ApJ* 284, 712–718
- Stetson P. B., 1991: Initial Experiments with Daophot-II and WFPC Images; in *DATA ANALYSIS WORKSHOP - 3RD ESO/ST-ECF GARCHING P. 187, 1991*; p. 187
- Suntzeff N. B., 1981: Carbon and nitrogen abundances in the giant stars of the globular clusters M3 and M13; *ApJS* 47, 1–32
- Suntzeff N. B., 1993: The Globular Cluster-Galaxy Connection; in *ASP Conf. Ser. 48*; p. 167
- Suntzeff N. B., Smith V. V., 1991: Carbon isotopic abundances in giant stars in the CN-bimodal globular clusters NGC 6752 and M4; *ApJ* 381, 160–172
- van Albada T. S., de Boer K. S., 1975: Pulsation properties of four RR Lyrae stars; *A&A* 39, 83–90
- VandenBerg D. A., 2000: Models for Old, Metal-Poor Stars with Enhanced α -Element Abundances. II. Their Implications for the Ages of the Galaxy's Globular Clusters and Field Halo Stars; *ApJS* 129, 315–352
- Ventura P., D'Antona F., Mazzitelli I., Gratton R., 2001: Predictions for Self-Pollution in Globular Cluster Stars; *ApJ* 550, L65–L69
- von Braun K., Mateo M., Chiboucas K., Athey A., Hurley-Keller D., 2002: Photometry Results for the Globular Clusters M10 and M12: Extinction Maps, Color-Magnitude Diagrams, and Variable Star Candidates; *AJ* 124, 2067–2082
- Winget D. E., Nather R. E., Clemens J. C., et al., 1991: Asteroseismology of the DOV star PG 1159 - 035 with the Whole Earth Telescope; *ApJ* 378, 326–346
- Wittlich M., 2002: *Studien an galaktischen Kugelsternhaufen mittels Strömgren-Photometrie: M 10, M 72 und NGC 6934*; Diploma thesis; Sternwarte der Universität Bonn
- Woolf V. M., Jeffery C. S., Pollacco D. L., 2002: Radial velocity variations of the pulsating subdwarf B star PG 1605+072; *MNRAS* 329, 497–501